

Sensitivity and Fragmentation Calibration of the ROSINA Reflectron-type Time-Of-Flight Mass Spectrometer

Inauguraldissertation
der Philosophisch-naturwissenschaftlichen Fakultät
der Universität Bern

vorgelegt von

Sébastien Gasc

von Frankreich

Leiterin der Arbeit:
Prof. Dr. Kathrin Altwegg
Physikalisches Institut der Universität Bern

Von der Philosophisch-naturwissenschaftlichen Fakultät angenommen.

Original document saved on the web server of the University Library of Bern



This work is licensed under a Creative Commons
Attribution-Non-Commercial-No derivative works 2.5 Switzerland licence.
To see the licence go to <http://creativecommons.org/licenses/by-nc-nd/2.5/ch/> or
write to Creative Commons, 171 Second Street, Suite 300, San Francisco, California 94105, USA.

Copyright Notice

This document is licensed under the Creative Commons Attribution-Non-Commercial-No derivative works 2.5 Switzerland. <http://creativecommons.org/licenses/by-nc-nd/2.5/ch/>

You are free:



to copy, distribute, display, and perform the work

Under the following conditions:



Attribution. You must give the original author credit.



Non-Commercial. You may not use this work for commercial purposes.



No derivative works. You may not alter, transform, or build upon this work..

For any reuse or distribution, you must take clear to others the license terms of this work.

Any of these conditions can be waived if you get permission from the copyright holder.

Nothing in this license impairs or restricts the author's moral rights according to Swiss law.

The detailed license agreement can be found at:

<http://creativecommons.org/licenses/by-nc-nd/2.5/ch/legalcode.de>

Sensitivity and Fragmentation Calibration of the ROSINA Reflectron-type Time-Of-Flight Mass Spectrometer

Inauguraldissertation
der Philosophisch-naturwissenschaftlichen Fakultät
der Universität Bern

vorgelegt von

Sébastien Gasc

von Frankreich

Leiterin der Arbeit:
Prof. Dr. Kathrin Altwegg
Physikalisches Institut der Universität Bern

Von der Philosophisch-naturwissenschaftlichen Fakultät angenommen.

Bern, den 18.12.2015

Der Dekan:
Prof. Dr. G. Colangelo

*“Mit dr Diss chaschs nid besser...
...aber länger”*

Abstract

The goal of this work was to increase the performance and to calibrate one of the ROSINA sensors, the Reflectron-type Time-Of-Flight mass spectrometer, currently flying aboard the ESA *Rosetta* spacecraft. Different optimization techniques were applied to both the lab and space models, and a static calibration was performed using different gas species expected to be detected in the vicinity of comet 67P/Churyumov-Gerasimenko. The database thus created was successfully applied to space data, giving consistent results with the other ROSINA sensors.

Contents

1	Introduction	2
1.1	Comets	2
1.2	Rosetta	6
1.3	ROSINA	9
1.3.1	DPU	9
1.3.2	COPS	9
1.3.3	DFMS	10
1.3.4	RTOF	10
1.3.5	ROSINA discoveries	11
1.4	Time-of-flight mass spectrometry	12
1.4.1	Ionization	12
1.4.2	Mass analyzers	13
1.4.3	Detectors	16
2	RTOF	17
2.1	Description	17
2.1.1	Ion sources	18
2.1.2	Drift tube	19
2.1.3	Reflectron	20
2.1.4	Hard mirror	20
2.1.5	Detectors	20
2.1.6	Gas calibration unit	20
2.1.7	Acquisition / electronics	21
2.1.8	Operations	22
2.2	Data processing	24
2.2.1	Peak fitting & integration	24
2.2.2	Mass scale calibration	25
2.3	Status in flight	26
3	Optimization	28
3.1	On-ground optimizations	28
3.2	In-flight optimizations	30
3.2.1	RTOF/SS	31
3.2.2	RTOF/OS	39
4	Calibration	40
4.1	CASYMIR	42
4.2	Measurement protocol	44
4.3	Data processing	44
4.3.1	Isotopic and fragmentation ratios	46
4.3.2	Sensitivity	47
4.4	Summary – D = –3'000 V	49
4.4.1	CO ₂ fragmentation	49
4.4.2	Krypton isotopic ratios	51

4.4.3	Sensitivities	51
4.4.4	GCU	52
4.5	Results – $D = -1'800\text{ V}$	54
4.5.1	General remarks	54
4.5.2	Noble gases	55
4.5.3	H_2O , CO , CO_2	58
4.5.4	C-H-bearing compounds	61
4.5.5	C-H-O-bearing compounds	65
4.5.6	C-H-N-bearing compounds	67
4.5.7	Other compounds	68
4.5.8	Sensitivities	68
4.6	Results – $D = -1'000\text{ V}$	70
4.6.1	H_2O , CO , CO_2 and krypton	70
4.6.2	Extrapolations	72
5	RTOF results from flight	75
5.1	Baseline variations	75
5.2	Seasonal variations	77
5.3	Diurnal variations	79
5.4	Summary	80
6	Conclusions and perspectives	83
A	RTOF voltage tables	84
B	Tables of fragmentation and isotopic ratios	86
B.1	$D = -3'000\text{ V}$	86
B.2	$D = -1'800\text{ V}$	87
B.3	$D = -1'000\text{ V}$	98
C	Tables of sensitivities	99
C.1	Granville-Phillips correction factors	99
C.2	$D = -3'000\text{ V}$	99
C.3	$D = -1'800\text{ V}$	100
C.4	$D = -1'000\text{ V}$	101
	Bibliography	107
	Acknowledgements	109
	Erklärung	110
	Curriculum Vitae	112

List of Figures

1.1	Solar System diagram	3
1.2	Comet tails	4
1.3	67P/Churyumov–Gerasimenko	5
1.4	<i>Rosetta</i>	6
1.5	(2867) Šteins and (21) Lutetia	7
1.6	DPU and COPS	9
1.7	DFMS and RTOF	10
1.8	Principle of the time-of-flight measurement	13
1.9	Spatial distribution	14
1.10	Kinetic energy distribution	15
2.1	3D drawing of RTOF	17
2.2	Sectional view of the SS	18
2.3	Sectional view of the OS	18
2.4	Reflectron – single reflection	20
2.5	Hard mirror – triple reflection	20
2.6	Example of ADC correction	21
2.7	Histogram to event ratio	22
2.8	Overlap of krypton isotopes	24
3.1	Comparison between the initial RTOF FM settings ($D = -3'000$ V) and lowered optimized settings ($D = -1'800$ V)	29
3.2	Comparison between the RTOF FM settings with $D = -1'800$ V and with $D = -1'000$ V	30
3.3	SS optimization – step 1.	31
3.4	SS optimization – comparison between step 1. and step 2.	32
3.5	SS optimization – comparison between step 2. and step 3.	33
3.6	SS optimization – step 4.	33
3.7	SS optimization – comparison between step 3. and step 5.	34
3.8	SS optimization – intensity of the signal with respect to BP and GR	36
3.9	SS optimization – global behavior of the peaks intensities	37
3.10	SS optimization – comparison between step 5. and step 6.	37
3.11	SS optimization – evolution of mass resolution and S/N ratio	38
3.12	OS optimization – comparison between initial and optimized settings	39
4.1	Picture of CASYMIR	42
4.2	Schematics of CASYMIR	43
4.3	Correlation between pressure and number of ions for the parent (H_2O) and a fragment (OH)	47
4.4	Example of calibration curve for the calculation of the sensitivity	48
4.5	Saturation effect for relatively high pressure measurements	49
4.6	Isotopologic and fragmentation ratios for CO^+	50
4.7	Isotopic ratios for Kr	51
4.8	Correlation between sensitivity and filament emission for CO_2 and Kr	52

4.9	Fragmentation model of a GCU spectrum	53
4.10	Correlation between mass and doubly/singly charged ions ratio	56
4.11	Isotopic ratios for Ne, Ar, Kr, and Xe	57
4.12	Isotopologic and fragmentation ratios for H ₂ O and CO	59
4.13	Isotopologic and fragmentation ratios for CO ₂	60
4.14	Fragmentation ratios – alkanes	62
4.15	Fragmentation ratios – acetylene, benzene	63
4.16	Fragmentation ratios – naphthalene	64
4.17	Fragmentation ratios – alcohols	65
4.18	Fragmentation ratios – acids	66
4.19	Fragmentation ratios – aldehydes	67
4.20	Fragmentation ratios – triazine	68
4.21	Correlation between ionization cross section and sensitivity	69
4.22	H ₂ O, CO, CO ₂ , and Kr ratios	71
4.23	RTOF FS OS GCU spectrum with its model	74
5.1	SS baseline level	76
5.2	OS baseline level	77
5.3	Seasonal variations	78
5.4	Diurnal variations	79
5.5	RTOF OS H ₂ O and CO ₂ maps of 67P/Churyumov-Gerasimenko’s coma	81
5.6	RTOF SS H ₂ O and CO ₂ maps of 67P/Churyumov-Gerasimenko’s coma	81

List of Tables

1.1	Basic characteristics of 67P/Churyumov-Gerasimenko	5
1.2	<i>Rosetta</i> timeline	7
1.3	<i>Rosetta</i> payload	8
2.1	Combinations implemented in the DPU	22
2.2	RTOF operation modes	23
2.3	Reference peaks used for the calculation of the mass scale	26
3.1	Commanded values for BP, GR, and P	34
3.2	Optimization matrix for BP, GR, and P	35
3.3	SS optimization – typical C and t_0 values	38
3.4	OS optimization – typical C and t_0 values	39
4.1	List of calibrated compounds	41
4.2	Calibration measurement protocol for each compound	45
4.3	GCU gases abundances for the three main FM OS neutral modes	53
4.4	Sensitivity scale factors for the SS and the OS modes ($D = -1'800$ V)	69
4.5	Sensitivity scale factors for the SS and the OS modes ($D = -1'000$ V)	72
4.6	Example of density calculations	74
A.1	RTOF FS settings – OS (neutrals)	84
A.2	RTOF FS settings – OS (ions)	84
A.3	RTOF FS settings – SS	85
B.1	Fragmentation ratios – CO_2 (OS, M513, FM and FS)	86
B.2	Isotopic ratios – krypton (OS, M513, FM and FS)	86
B.3	Isotopic ratios – the noble gases (FM, $D = -1'800$ V)	87
B.4	Frag. and isotopologic ratios – H_2O , CO , CO_2 (FM, $D = -1'800$ V)	88
B.5	Frag. and isotopologic ratios – CH_4 (FM, $D = -1'800$ V)	88
B.6	Frag. and isotopologic ratios – C_2H_6 (FM, $D = -1'800$ V)	89
B.7	Frag. and isotopologic ratios – C_3H_8 (FM, $D = -1'800$ V)	89
B.8	Frag. and isotopologic ratios – C_4H_{10} (FM, $D = -1'800$ V)	90
B.9	Frag. and isotopologic ratios – C_2H_2 (FM, $D = -1'800$ V)	90
B.10	Frag. and isotopologic ratios – C_6H_6 (FM, $D = -1'800$ V)	91
B.11	Frag. and isotopologic ratios – C_{10}H_8 (FM, $D = -1'800$ V)	92
B.12	Frag. and isotopologic ratios – CH_3OH (FM, $D = -1'800$ V)	93
B.13	Frag. and isotopologic ratios – $\text{C}_2\text{H}_5\text{OH}$ (FM, $D = -1'800$ V)	93
B.14	Frag. and isotopologic ratios – HCOOH (FM, $D = -1'800$ V)	94
B.15	Frag. and isotopologic ratios – CH_3COOH (FM, $D = -1'800$ V)	95
B.16	Frag. and isotopologic ratios – H_2CO (FM, $D = -1'800$ V)	96
B.17	Frag. and isotopologic ratios – CH_3CHO (FM, $D = -1'800$ V)	96
B.18	Frag. and isotopologic ratios – $\text{C}_3\text{H}_3\text{N}_3$ (FM, $D = -1'800$ V)	97
B.19	Frag. and isot. ratios – H_2O , CO , CO_2 , and Kr (FM, $D = -1'000$ V)	98

C.1	Correction factors for the pressure measurements of the Granville-Phillips stabil ion gauge	99
C.2	CO ₂ and krypton sensitivities for D = -3'000 V	99
C.3	Sensitivity conversion factors for SS and OS modes (D = -1'800 V) . .	100
C.4	Sensitivities for D = -1'000 V	100
C.5	Sensitivity conversion factors for SS and OS modes (D = -1'000 V) . .	101
C.6	Scale factors for the extrapolation of the sensitivities from D = -1'800 V to D = -1'000 V	101
C.7	Sensitivities for D = -1'000 V	101

1. Introduction

Comets have long been a subject of fascination to humankind, evolving from being a bad omen to being a good candidate for the apparition of water and life on Earth.

The technological developments of the last century made the *in situ* study of these celestial bodies possible, in particular with *Rosetta*, a Cornerstone Mission of the European Space Agency (ESA) Horizon 2000 programme; its main objective is the study of comet 67P/Churyumov-Gerasimenko (67P/C-G). On board, the Rosetta Orbiter Spectrometer for Ion and Neutral Analysis (ROSINA) has been designed to determine the global molecular, elemental, and isotopic composition and the physical, chemical, and morphological character of the cometary nucleus (Balsiger et al., 2007). It consists of a pressure sensor and two mass spectrometers; the detailed characterization of the Reflectron-type Time-Of-Flight mass spectrometer (RTOF) will be the aim of this work.

Designed to achieve high performance, the capacities of RTOF were reduced shortly after launch due to a failure of a voltage converter. To achieve the best possible performance in these new circumstances, optimizations were conducted on the ground with the spare instrument, as well as in space.

The primary goal of RTOF is to identify the species present in 67P/C-G's atmosphere. To deconvolve a mass spectrum that results from a gas mixture, it is necessary to know the specific response of RTOF to each molecule. This response depends on the sensitivity of the instrument, i.e. on its settings, leading to the necessity of performing an instrument-specific calibration, for as many species expected in the vicinity of the comet as possible.

The current chapter will be dedicated to the introduction of comets and mass spectrometry; the particular case of RTOF will be described in the subsequent chapter. Chapter 3 will present the results of the optimizations conducted to improve the performance of RTOF after the failure, and the following chapter will detail the calibration campaigns undertaken to prepare the analysis of space data. Finally, the last chapter will be a short overview of the cometary science achieved by RTOF in space since the launch.

1.1 Comets

Origins and families

The birth of a solar system results from the contraction of an interstellar cloud into a protoplanetary disk. The accretion of dust and condensed gas creates planetesimals which in turn form planets. Comets observed in our Solar System are believed to be remnant planetesimals which were not absorbed by the giant planets.

Two main models are proposed to explain their formation: the *fluffy aggregates model* (Donn and Hughes, 1986) and the *primordial rubble pile* (Weissman, 1986). These

comet formations would have happened in two regions: between Jupiter and Uranus (Jewitt, 2004), and in the main asteroid belt (Hsieh and Jewitt, 2006). The comets would have then migrated to other locations, where they remain nowadays; due to stellar encounters or other gravitational effects, some of these objects are regularly sent towards the inner Solar System, following orbits with eccentricities usually ranging from 0.2 to 0.7, few of them having an eccentricity close to 1.0.

Comets are classified into families according to their orbits: *long-period comets* or *Oort cloud comets* have an orbital period above 200 years, and originate from the *Oort cloud* (Oort, 1950); *short-period comets* originate from the *Kuiper belt* (Morbidelli, 2008) and have shorter periods. The location of the Kuiper belt and the Oort cloud can be seen in figure 1.1. Short-period comets are subdivided into two categories: the *Halley family* for comets with orbital periods between 20 and 200 years, and *Jupiter family comets* (JFC) for comets with a period of approximately 6 years.

In addition to the Oort cloud and to the Kuiper belt, another reservoir has been proposed by Hsieh and Jewitt (2006) and described more recently as a *comet graveyard* (Ferrín et al., 2013), providing a possible origin for the objects recently discovered in the main asteroid belt and presenting cometary activity.

Comets were created far from the Sun and have remained far from the Sun, behind the snowline. This line is a limit located between the orbits of Mars and Jupiter and corresponds to the heliocentric distance where ice can be formed. This characteristic has earned them the nickname of “dirty snow balls” since 1950 (Whipple, 1950). Due to these cold temperatures, the composition of the cometary material is not expected to have changed since their formation, making comets good witnesses of the composition of the early Solar System.

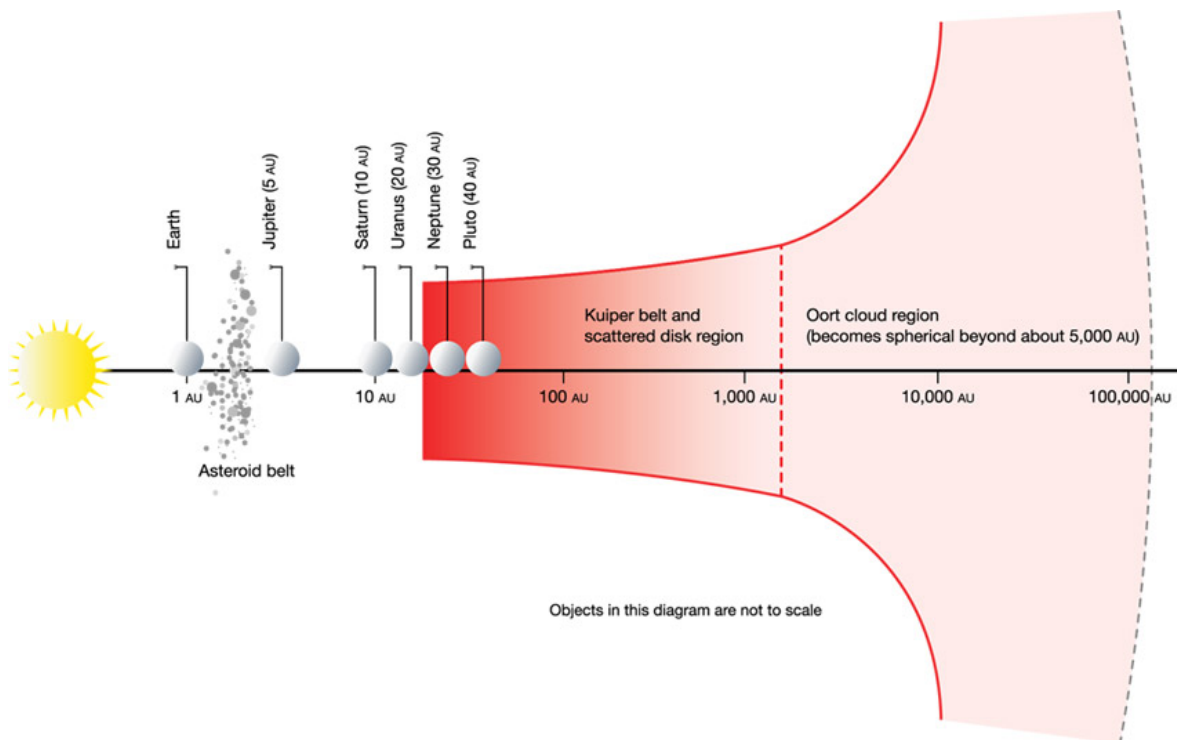


Figure 1.1: Solar System diagram. From Stern (2003).

Characteristics

Comets differ from the other celestial objects by the fact that they are *active* or *inactive*, depending on their distance to the Sun, and thus they are visible only for a short amount of time. Comets consists of three distinct parts:

- a *nucleus* with a low albedo, with typical sizes ranging from a few kilometers to a few dozens of kilometers
- a *coma*, or cometary atmosphere, composed of gases sublimated from the nucleus
- a *dust tail*, consisting of dust particles pushed by the solar radiation pressure, curved in the orbital plane due to the Sun's gravity, and an *ion tail*, in the direction opposite to the Sun, distorted by the solar wind

The dust tail can reach several millions of kilometers, making the comets the biggest objects in the Solar System (see figure 1.2, right picture).

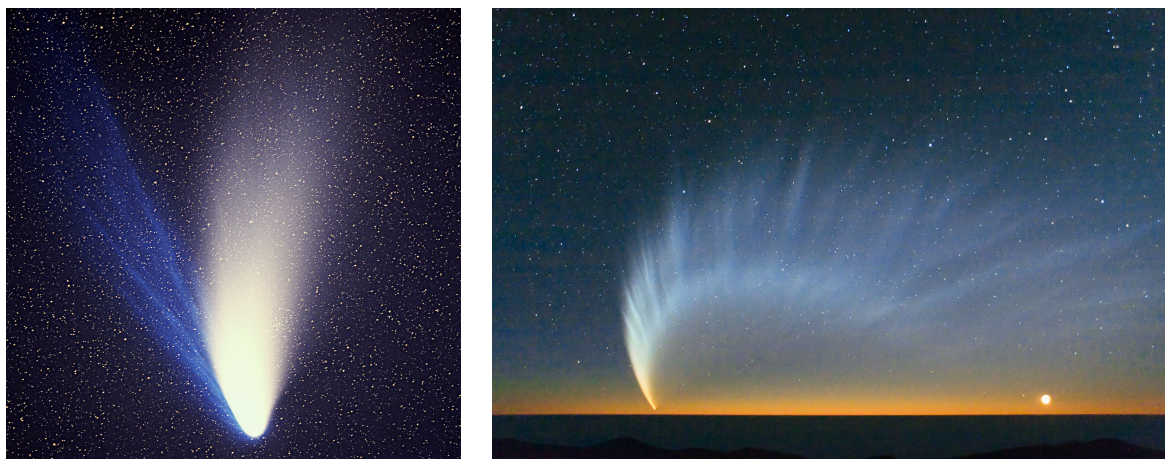


Figure 1.2: Left: picture of comet C/1995 O1 (*Hale-Bopp*) (image taken by E. Kolmhofer and H. Raab from Johannes-Kepler-Observatory). The blue ion tail and the white dust tail are easily identifiable. Right: picture of comet C/2006 P1 (*McNaught*) over the Pacific Ocean (image taken from Paranal Observatory in January 2007; credit: S. Deiries/ESO). Tails of comets can reach several millions of kilometers.

67P/Churyumov-Gerasimenko

67P/Churyumov-Gerasimenko (67P/C-G) is a Jupiter family comet discovered in 1969 by Klim Ivanovich Churyumov, on a photographic plate captured by Svetlana Ivanovna Gerasimenko. It appeared that this photography was acquired only a few hours after the comet's perihelion, on its second observable passage: after an unknown amount of time orbiting with perihelion distances greater than 4 astronomical units (AU, defined as the Sun-Earth distance), two perturbations from Jupiter in 1840 and 1959 decreased the perihelion distance to about 1.28 AU. Since 1969, 67P/C-G was observed at each perihelion passage, every 6.44 years.

Two lobes were identified and are clearly visible in figure 1.3. A few other characteristics are summarized in table 1.1. These measurements are based on data collected in the first few months at the comet; measurements are subject to change as the comet evolves and as more data are collected.

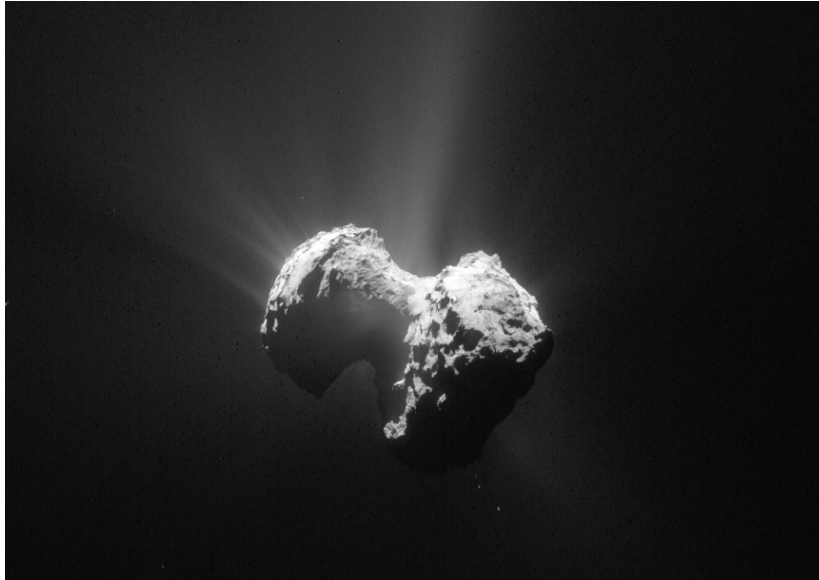


Figure 1.3: Picture of comet 67P/Churyumov–Gerasimenko taken by the Rosetta NAVCAM on 20th July, 2015 from a distance of 171 km from the comet centre. Credit: ESA/Rosetta/NAVCAM.

Table 1.1: Basic characteristics of 67P/Churyumov-Gerasimenko (ESA).

Volume	21.4 km ³
Mass	$1 \cdot 10^{13}$ kg
Density	470 kg · m ⁻³
Porosity	70–80 %
Average albedo	6 %
Rotation period	12.4 hours

Cometary space missions

- The *International Cometary Explorer* (ICE), launched on 12th August 1978, passed through the plasma tail of Comet 21P/Giacobini-Zinner within approximately 7'800 km of the nucleus on 11th September 1985. It was the first spacecraft to visit a comet.
- *Vega 1 & 2*, launched on 15th December 1984, closest approach at 8'890 km from 1P/Halley's nucleus on March 6, 1986.
- *Suisei*, launched on 19th August 1985, distant flyby of 1P/Halley (151'000 km) on 8th March 1986.
- *Sakigake*, launched on 7th January 1985, distant flyby of 1P/Halley ($6.99 \cdot 10^6$ km) on 11th March 1986.

- *Giotto*, launched on 2nd July 1985, flyby of 1P/Halley on 13th March 1986, at 596 km, and flyby of 26P/Grigg-Skjellerup on 10th July 1992, at 200 km. *Giotto* gave the first images of a comet nucleus and was such an important step in cometary sciences that many authors talk about “pre-Halley” and “post-Halley” eras.
- *Deep Space 1*, launched on 24th October 1998, flew in the tail of 19P/Borrelly at 2'171 km from the nucleus on 22nd September 2001.
- *Stardust*, launched on 7th February 1999, flyby of 81P/Wild (236 km) on 24th January 2004; cometary dust was brought back to Earth on 15th January 2006. On 15th February 2011, flyby of 9P/Tempel (190 km).
- *Deep Impact*, launched on 12th January 2005, impacted 9P/Tempel with a copper projectile of 372 kg on 4th July 2005; renamed *EPOXI*, the spacecraft approached 103P/Hartley at 700 km on 4th November 2010.
- *Rosetta*, launched on 2nd March 2004, detailed hereafter.

1.2 Rosetta

The *Rosetta* mission is a Cornerstone Mission in ESA's Horizons 2000 Science Programme, which was named after the Rosetta Stone which allowed Jean-François Champollion to translate the Egyptian hieroglyphs and thus reconstitute the history of ancient Egypt. Similarly, the *Rosetta* mission is intended to provide new elements to understand the origin of the formation of the Solar System.

Initially targeted towards comet 46P/Wirtanen, *Rosetta* was delayed by one year after the failure of an Ariane 5 rocket in December 2002, and was finally launched on 2nd March 2004 towards comet 67P/Churyumov-Gerasimenko. After a 10-year journey including multiple gravity assists from Earth (3 times) and Mars (once), flybys of asteroids (2867) Šteins in 2008 and (21) Lutetia in 2010 (see figure 1.5), and almost three years of hibernation, *Rosetta* arrived at 300 km from the nucleus of comet 67P/C-G in August 2014 (see timeline in table 1.2).

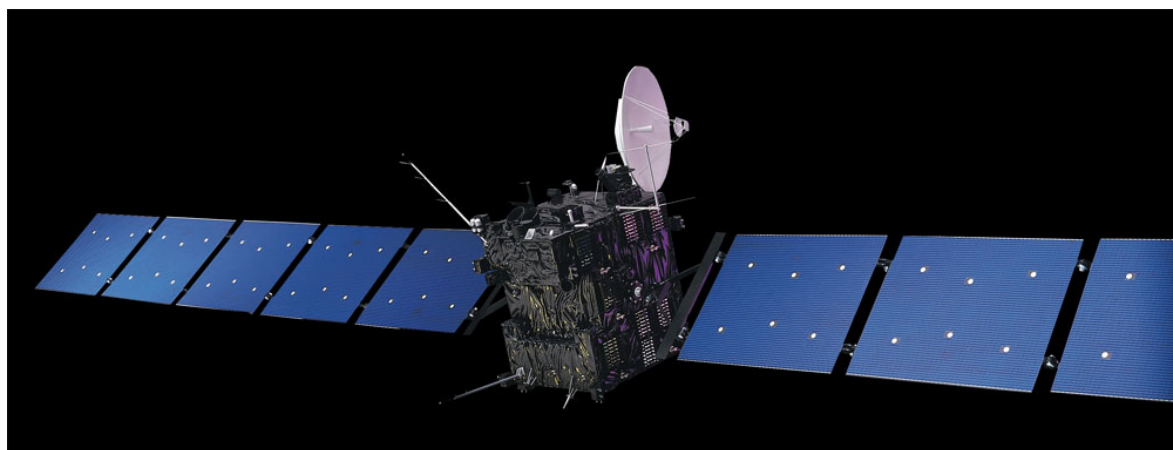


Figure 1.4: The *Rosetta* spacecraft. Credit: ESA/AOES Medialab.

Table 1.2: *Rosetta* timeline.

Date	Event
02/03/2004	Launch
04/03/2005	First gravity assist – Earth
25/02/2007	Second gravity assist – Mars
13/11/2007	Third gravity assist – Earth
05/09/2008	Flyby of (2867) Šteins (800 km)
13/11/2009	Last gravity assist – Earth
10/07/2010	Flyby of (21) Lutetia (3'162 km)
08/06/2001	Start hibernation
20/01/2014	Wake up from hibernation
10/09/2014	Orbit insertion at 30 km from the nucleus
15/10/2014	10 km orbit
12/11/2014	Release of <i>Philae</i> and landing on 67P/C-G
15/11/2014	End of <i>Philae</i> 's nominal operations
13/06/2015	Wake up of <i>Philae</i>
13/08/2015	Perihelion passage
31/12/2015	Nominal end of mission
09/2016	End of extended mission

The scientific measurement goals of *Rosetta* include (Schwehm and Schulz, 1999):

- Global characterization of the nucleus, determination of dynamic properties, surface morphology and composition.
- Determination of chemical, mineralogical and isotopic compositions of volatiles and refractories in a cometary nucleus.
- Determination of the physical properties and interrelation of volatiles and refractories in a cometary nucleus.
- Study of the development of cometary activity and processes in the surface layer of the nucleus and inner coma (dust/gas interaction).

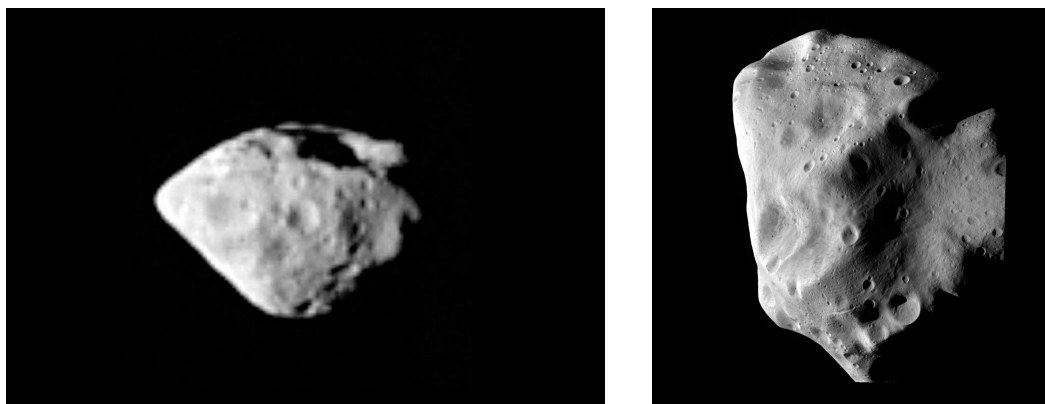


Figure 1.5: Left: OSIRIS wide angle camera image of asteroid (2867) Šteins taken around closest approach. Right: Asteroid (21) Lutetia at closest approach. Credit: ESA 2010 MPS for OSIRIS Team MPS/UPD/LAM/IAA/RSSD/INTA/UPM/DASP/IDA.

To achieve these goals, *Rosetta* consists of an orbiter (shown in figure 1.4) and a lander, *Philae*. Their overall mass is approximately 2'900 kg and includes the lander as well as the scientific payload. A brief description of the instruments is given in table 1.3 (based on Schulz et al. (2009)).

Table 1.3: *Rosetta* payload.

	Name	Instrument	Category
ORBITER	ALICE	UV imaging spectrograph	Remote sensing
	CONCERT	Radio sounding, nucleus tomography	Nucleus large-scale structure
	COSIMA	Cometary Secondary Ion Mass Analyser	Coma composition
	GIADA	Grain Impact Analyser and Dust Accumulator	Dust flux and mass distribution
	MIDAS	Micro-Imaging Dust Analysis System	Coma composition
	MIRO	Microwave Instrument for the Rosetta Orbiter	Remote sensing
	OSIRIS	Optical, Spectroscopic, and Infrared Remote Imaging System	Remote sensing
	ROSINA	Rosetta Orbiter Spectrometer for Ion and Neutral Analysis	Coma composition
	RPC	Rosetta Plasma Consortium	Comet plasma environment & solar wind interaction
	RSI	Radio Science Investigation	Radio science
LANDER	VIRTIS	Visible and Infrared Thermal Imaging Spectrometer	Remote sensing
	APXS	Alpha Particle X-ray Spectrometer	Nucleus composition
	CIVA	Comet Infrared & Visible Analyser	Nucleus surface structure
	CONCERT	Comet Nucleus Sounding Experiment by Radiowave Transmission	Nucleus structure
	COSAC	Cometary Sampling and Composition experiment	Nucleus composition
	MUPUS	Multi-Purpose Sensors for Surface and Subsurface Science	Nucleus structure
	PTOLEMY	Isotopic composition sampling	Nucleus composition
	ROLIS	Rosetta Lander Imaging System	Nucleus surface structure
	ROMAP	Rosetta Lander Magnetometer and Plasma Monitor	Nucleus structure
	SD2	Sample and Distribution Device	Nucleus structure
SESAME	Surface Electrical, Seismic and Acoustic Monitoring Experiments	Nucleus surface structure	

Rosetta cumulates many firsts:

- First mission to go close to Jupiter's orbit using solar panels.
- First mission to orbit a comet's nucleus and to stay in orbit as the comet heads towards the inner Solar System.
- First mission to soft land on a comet.

Rosetta provided many new scientific data as well; the description of the first scientific results, other than the ones described in the description of 67P/C-G, will focus on the discoveries from ROSINA and is done in the next section.

1.3 ROSINA

Among the eleven instruments carried by the orbiter, the Rosetta Orbiter Spectrometer for Ion and Neutral Analysis (ROSINA) consists of two complementary mass spectrometers, the Reflectron-type Time Of Flight mass spectrometer (RTOF) and the Double Focusing Mass Spectrometer (DFMS), and a pressure sensor, the COmetary Pressure Sensor (COPS). A Data Processing Unit (DPU) controls the three sensors.

The science goals of ROSINA are to determine the global molecular, elemental, and isotopic composition and the physical, chemical, and morphological character of the cometary nucleus, and to investigate the origin of comets, the relationship between cometary and interstellar material and the implications for theories on the origin of the Solar System (Balsiger et al., 2007).

ROSINA was designed, built, and tested at the University of Bern, Space Research and Planetology department.

1.3.1 DPU

The DPU (figure 1.6, left picture) is responsible for the complete operation of ROSINA and also for its communication with the Rosetta spacecraft. The main components are a 32-bit signal processor with 3 MB program and 8 MB data memory.

Another important role of the DPU concerns the handling of the data volume. Due to a limited data rate available for telemetry, the spectra acquired with the two mass spectrometers need to be compressed: this task is handled by the DPU.

1.3.2 COPS

COPS (figure 1.6, right picture) consists of two gauges: the *nude gauge* (NG) measures the total neutral particle density, while the *ram gauge* (RG) measures the ram pressure from the cometary gas flux, from which we can derive the total neutral gas density (i.e. comet activity).

Additionally, COPS serves as a safety instrument for *Rosetta*, as it informs the other sensors in real time about the surrounding pressure, allowing these sensors to switch themselves OFF if this pressure is too high, i.e. dangerous for instrument operation.

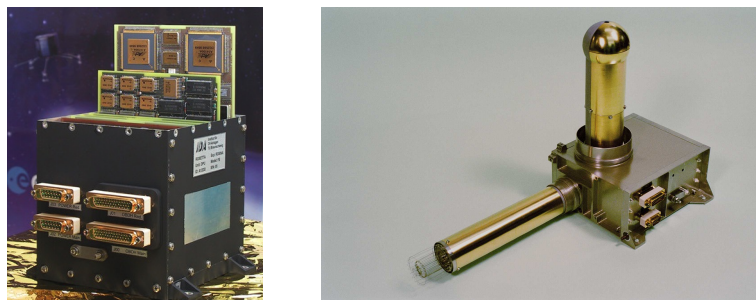


Figure 1.6: Left: the DPU weights 2.2 kg and requires 5 W. Right: COPS weights 1.7 kg and requires 7 W.

1.3.3 DFMS

DFMS (figure 1.7, top picture) is a double focusing mass spectrometer designed according to the Nier-Johnson configuration (Johnson and Nier, 1953). It can measure ions as well as neutrals, the latter being ionized in an ion source by electron impact ionization (see section 1.4.1). An electrostatic analyzer is used to focus the ions in angle and energy, before the ions are separated according to their mass by a sector magnet. The detection of the ions can be performed by three independent detectors: a position sensitive multi channel plate in combination with a linear electron detection array, a channel electron multiplier and a faraday cup.

These features translate into high performance: DFMS has a mass range of 12 to 150 u/e, a high dynamic range (10^8), and a mass resolution $m/\Delta m \approx 3'000$ at 1 % peak height and $m/\Delta m \approx 9'000$ at 50 % peak height, for mass 28.

1.3.4 RTOF

The description of RTOF (figure 1.7, bottom picture) will be detailed in chapter 2. However, it is worth mentioning that DFMS and RTOF are complementary: if DFMS has a much higher mass resolution, RTOF has a higher temporal resolution and a higher mass range.

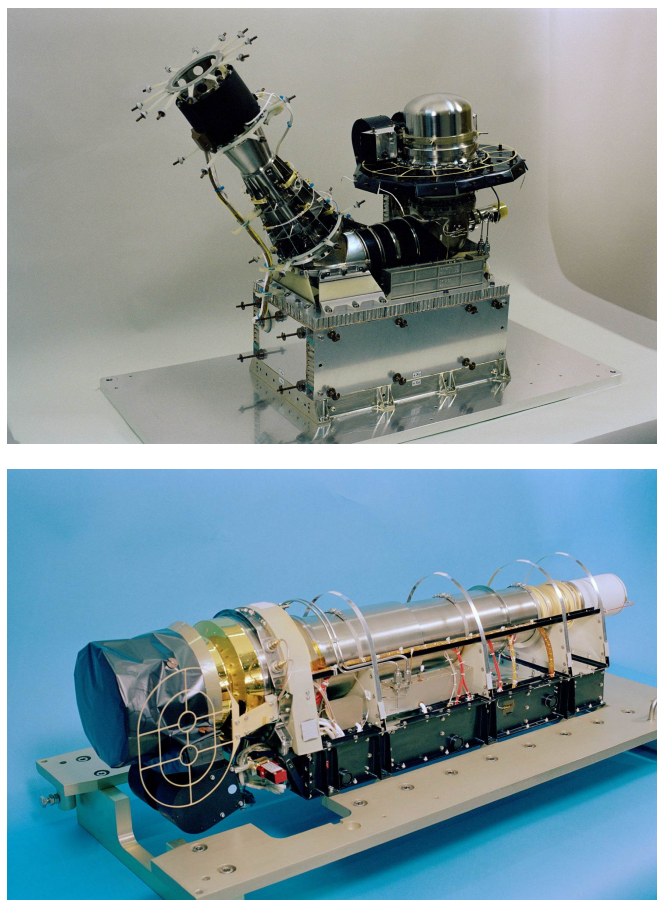


Figure 1.7: Top: DFMS weights 16 kg and requires 22 W. Bottom: RTOF weights 15 kg and requires 26 W.

1.3.5 ROSINA discoveries

From the first months after the encounter with 67P/C-G, many scientific results were published, from many of the experiments onboard *Rosetta*. This section summarizes briefly the discoveries published by ROSINA at the time of writing.

- Altwegg et al. (2015) reported the direct *in situ* measurement of a D/H ratio of $(5.3 \pm 0.7) \cdot 10^{-4}$ in 67P/C-G, concluding that the D/H values of Jupiter family comets may be highly heterogeneous, and precluding the idea that this reservoir is solely composed of Earth ocean-like water.
- Hässig et al. (2015) reported measurements of H₂O, CO, and CO₂, in a strongly heterogeneous coma, with substantial diurnal and latitudinal variations.
- Rubin et al. (2015) reported the first direct *in situ* measurement of N₂ in 67P/C-G, with a calculated N₂/CO ratio of $(5.70 \pm 0.66) \cdot 10^{-3}$ (2σ standard deviation of the sampled mean) corresponding to depletion by a factor of $\approx 25.4 \pm 8.9$ as compared to the protosolar value. Two suggestions arose from these values: 67P/C-G may have agglomerated from grains formed at about 30 K or below, and JFC comets were probably not the main source of Earth's nitrogen.
- Balsiger et al. (2015) reported the detection of argon in 67P/C-G and confirmed that comets of this type cannot be the main source of Earth's major volatiles, nor can they be the origin for terrestrial water.
- Bieler et al. (2015a) reported the first direct *in situ* measurement of O₂ in the coma of 67P/Churyumov-Gerasimenko with local abundances ranging from 1 % to 10 % relative to H₂O and a mean value of 3.80 ± 0.85 %, suggesting that primordial O₂ was incorporated into the cometary nucleus during the comet's formation.
- Bieler et al. (2015b) presented the first full 3D simulation results of 67P/C-G's neutral gas coma; the model validates the assumption that illumination conditions on the nucleus are at least an important driver of the gas activity, and calculates a production rate of about $1 \cdot 10^{26}$ molecules \cdot s⁻¹ between August and November 2014.
- Fuselier et al. (2015) reported the observation of primary ions such as organic volatiles and water group ions and their breakup products, CO⁺, CO₂⁺, and other mass peaks at masses 26, 27, and possibly 30; secondary ions were observed as well, such as H₃O⁺ and HCO⁺. A model was presented, predicting the H₃O⁺/H₂O⁺ and the HCO⁺/CO⁺ ratios.
- Le Roy et al. (2015) reported the detection of almost all species currently known to be present in cometary coma, and the significant differences in relative abundance between summer and winter hemispheres.
- Luspay-Kuti et al. (2015) analyzed the heterogeneity of various minor volatile species such as C₂H₆, HCN, CH₃OH, and CH₄, in the winter (southern) hemisphere of 67P/C-G.
- Wurz et al. (2015) reported the observation of sputtered refractory elements from the surface of 67P/C-G, and derived values for Na/Si, Ca/Si, and K/Si.

1.4 Time-of-flight mass spectrometry

The aim of this section is to provide some general elements about mass spectrometry, and more particularly about time-of-flight (TOF) mass spectrometry, as a prerequisite for chapter 2, where the specifics of RTOF will be more detailed.

The principle of mass spectrometry consists of separating atomic or molecular ions according to their mass-to-charge (m/z) ratio. Various possibilities exist, following a common structure:

- an **ion source** ionizes the compound to be analyzed,
- a **mass analyzer** separates the ions according to their m/z ratio,
- a **detector** converts the ion current into a numerical signal.

A few of the most common methods used during each steps are listed hereafter, but only the techniques applied to RTOF will be detailed in this work.

1.4.1 Ionization

The first step to analyze a neutral (atom or molecule) is to ionize it, so that it can be moved along a defined path in the spectrometer by electric fields. Several ionization processes exist, such as thermal ionization, field ionization, matrix assisted laser desorption ionization, and secondary ion mass spectrometry. The ionization method chosen for RTOF is electron impact ionization (EII).

The principle of EII lies in the capacity of an energetic electron to create fluctuations in the electric field around the neutral atom or molecule, resulting in an ionization and a fragmentation of the latter. This process is shown in equation 1.1: the perturbation induced by a primary electron e_p^- leads to the ionization of the molecule M and the ejection of a secondary electron e_s^- . EII is mainly used for the study of gases and volatile organic molecules.



A filament is heated to create the electron beam needed for this process. The ionization and the fragmentation depends strongly on the electron beam energy, i.e. on the difference of potential between the filament and the ionization region.

With a difference of potential of 70 V, the electrons have an energy of $U = 70$ eV, which is the energy range where the majority of ionization cross sections for organic molecules have their maxima (Mark, 1982). If the ionization region had a different potential, and for the same filament potential, then the electron beam energy would not remain at 70 eV, and the ionization as well as the fragmentation would be different. This phenomenon will be encountered in both chapters 3 and 4.

EII is a highly reproducible physical process. For molecules with very similar masses, seen as a single peak, the fragmentation ensuing EII offers the possibility to deconvolve a spectrum and to know the contribution of each parent molecule.

1.4.2 Mass analyzers

The purpose of the mass analyzers is to separate the ions. Many analyzers exist: time-of-flight (TOF), quadrupole, magnet sector, double focusing, Fourier transform... TOF will be detailed below but several definitions are necessary at first.

- The **mass range** represents the range of m/z achievable by a given analyzer.
- The **mass resolution** translates the ability of a mass spectrometer to separate ions of two different m/z , and is generally (and in this work) calculated using the peak width at the half maximum height, or Full Width at Half Maximum (FWHM). With this definition, the mass resolution R can be expressed as $R = m/\Delta m$. The mass resolution will be given for mass 28 in this work.
- The **sensitivity** of an instrument to different species is needed to correctly convert measured counts to a physical unit. It depends on the cross section of the atom or molecule analysed, the detector efficiency, the filament emission, and the transmission of the instrument (see section 4.3.2).

The principle of a TOF mass spectrometer is to accelerate the newly created ions with the same energy qU so that their speed v would only depend on their mass m (equation 1.2), and to measure the time $t = d/v$ they need to travel through the instrument of length d (equation 1.3). Figure 1.8 illustrates this principle with three ions of different masses.

$$qU = \frac{1}{2}mv^2 \quad (1.2)$$

$$t = d \cdot \sqrt{\frac{m}{2qU}} \quad (1.3)$$

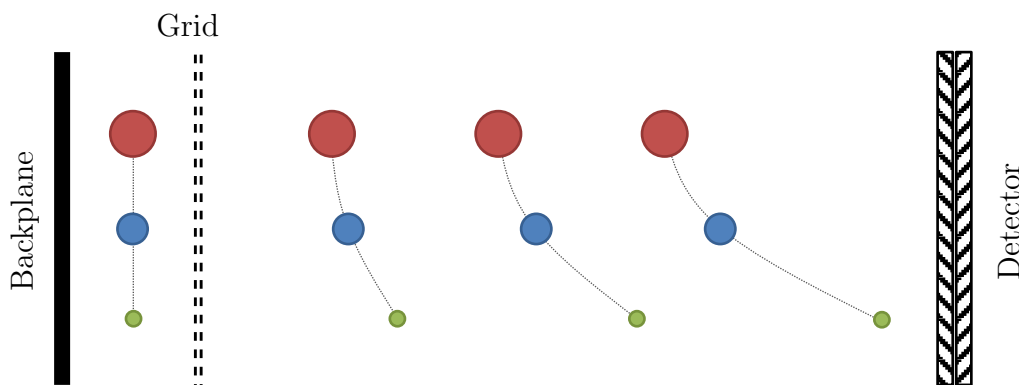


Figure 1.8: Principle of the time-of-flight measurement. Ions are created between the backplane and the grid; when a pull-pulse is applied on the grid, the ions are extracted from the ion source and travel in a field-free drift region at a constant velocity. The light ones travel faster than the heavy ones, reaching the detector in a shorter time.

This acceleration starts with a pulse, which either pushes the ions away from the ion source (*push-pulse*) or pulls the ions (*pull-pulse*) towards a field-free region where they will keep flying towards the detector.

Depending on the pulse shape and the initial distribution of the ions in the source, the mass resolution may vary: a parallel with Optics can be done, where the sharpness of the object directly influences the quality of the image. In this case, the object would be the pool of ions, the optics would be the electrodes (or *ion optics*), and the quality of the image would be the mass resolution.

Two kinds of distributions are incriminated here: the spatial distribution of the ions in the ion source, and their kinetic energy distribution.

Spatial distribution

Depending on their initial location in the ion source, and particularly their distance to the electrode where the pulse is applied, ions will get a different amount of kinetic energy from the electric field, as the energy received depends on the difference of potential the ions travel through. The fast ions, leaving the ion source later, catch up the slow ions in a focal plane which depends on the geometry of the ion source (see figure 1.9).

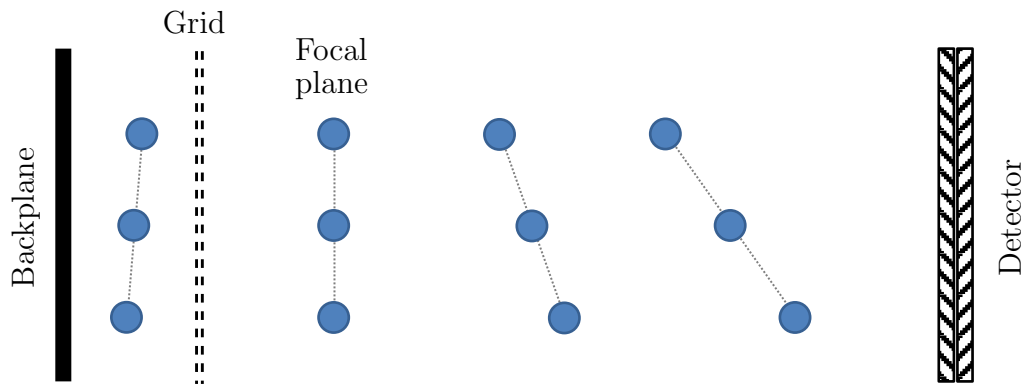


Figure 1.9: The spatial distribution of the ion source causes a spread in travel velocity and a loss in mass resolution.

Kinetic energy distribution

When the ions are extracted out of the ion source, the kinetic energy acquired is added to the initial energy the gas molecules had before the ionization. For ideal gases, this energy U_0 is proportional to the temperature T , following equation 1.4 where k_B is the Boltzmann constant.

$$U_0 = \frac{3}{2}k_B T \quad (1.4)$$

Two ions of the same mass can therefore have different velocity vectors before the extraction, pointing in different directions. In the worst case, where the velocity vector points in the direction opposite to the detector, the ion will first need to turn around before flying towards the detector. This adds a delay in the time of flight, compared to an ion of the same mass but with a velocity vector already pointing towards the detector. This phenomenon is represented in figure 1.10. The turn around time t_{turn} of an ion of mass m can be calculated using equation 1.5, with e the electric charge and E_s the electric field strength inside the source.

$$t_{\text{turn}} = 2 \frac{\sqrt{2mU_0}}{eE_s} \quad (1.5)$$

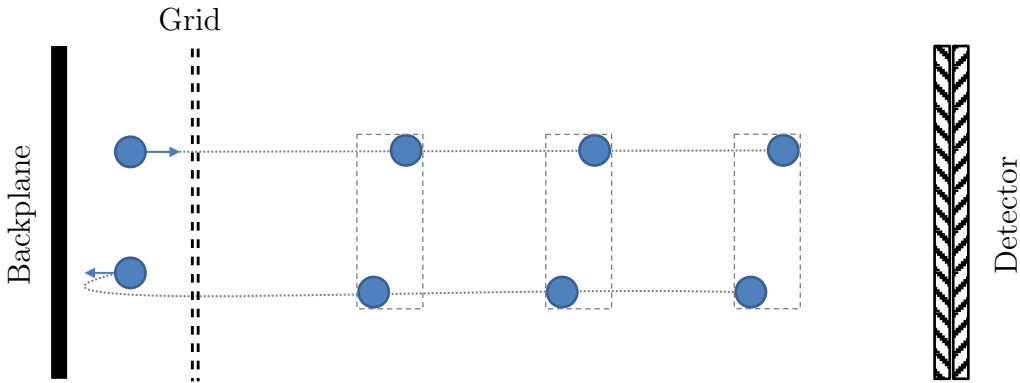


Figure 1.10: The initial kinetic energy of the neutrals creates a dispersion of the ions after the extraction. No focal plane exists, as the ions have the same velocity once in the field-free region, between the grid and the detector.

Reflectron

Several solutions exist to reduce the impact of these distributions on the mass resolution. For instance, increasing the field strength E_s in equation 1.5 will decrease the turn around time, and thus the kinetic energy distribution will be smaller.

Another way to narrow these distributions and therefore increase the mass resolution was proposed by Mamyrin et al. (1973): a reflectron makes the ions turn around at the end of the drift tube and focuses them in a time-focus plane on the detector, then located close to the ion source. Not only does it compensate the energy dispersion, but it also doubles the flight path, increasing the mass resolution (see figure 2.5 page 20).

1.4.3 Detectors

Several detectors and amplifiers can be combined with the previous mass analyzers and with different ionization processes, such as faradays cups, imaging detectors, solid state detectors, or secondary electron multipliers. The latter can be divided into several sub-categories containing channel electron multipliers, discrete dynode tubes, multichannel plates, and multisphere plates. The multichannel plates or microchannel plates (MCP) have been chosen for RTOF.

An MCP typically consists of a few million channels of a few micrometers in diameter, making an angle with the MCP surface so that the entering ions would hit the walls of the channels. The impact generates several electrons, which in turn hit the walls and create an electron cascade.

The gain of MCP detectors is a function of the accelerating potential between the front and the back of the MCP, and is typically of 10^3 to 10^5 .

2. RTOF

2.1 Description

The Reflectron-type Time-Of-Flight mass spectrometer (RTOF) is a TOF mass spectrometer consisting of:

- two ion sources, one dedicated to neutrals and the other to ions
- a drift tube
- a reflectron
- a hard mirror
- two detectors

Additionally, an ion attraction grid, located in front of the ion source entrances and charged negatively during the ion measurements, attracts the positively charged ions. A positive or a negative potential can be applied as well to compensate for the spacecraft charging (see 2.1.8).

The function of the cover was to avoid a contamination from the Earth's atmosphere and to protect the sensor head from any unintended dust entry into the ion sources during launch, and is now used in flight as a shield against dust grains and solar radiation. A motor ensures the positioning of the cover along 20 different positions, over 140° .

The main elements listed above are detailed in the next sections; a drawing of RTOF is presented in figure 2.1. The performance of the instrument will be addressed in the next chapters.

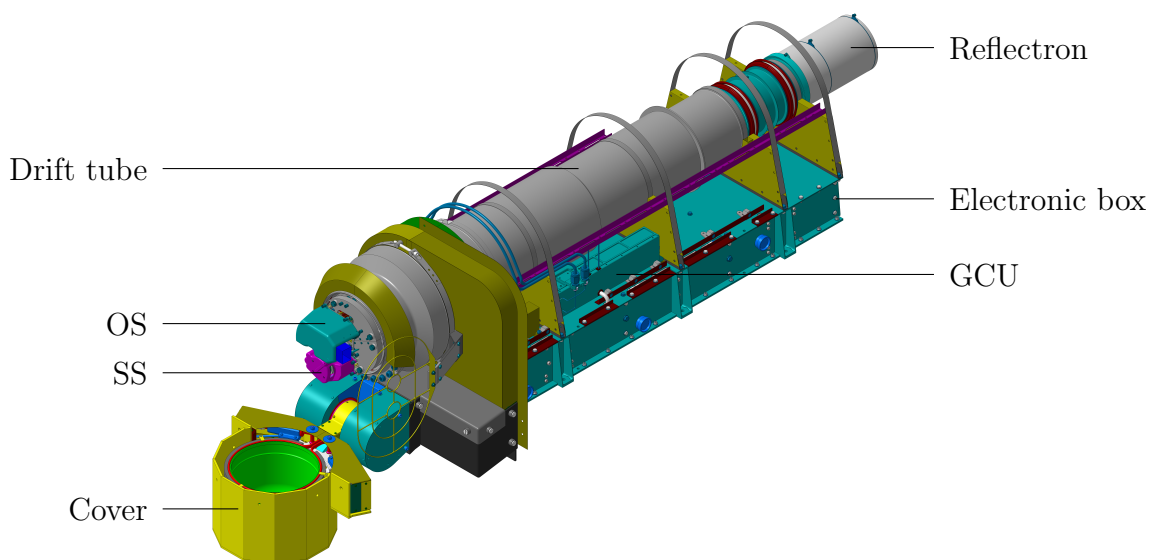


Figure 2.1: 3D drawing of RTOF.

2.1.1 Ion sources

RTOF contains two ion sources: the Storage Source (SS) and the Orthogonal extraction Source (OS). Both sources are capable of measuring cometary neutral gas while the latter also allows measuring cometary ions. They can be operated independently or together to study neutrals and ions simultaneously.

Each ion source consists of two filaments, two repellers, a backplane, an extraction grid, two acceleration electrodes and a lens electrode. Additionally, the OS has two entrance lenses to focus the entering ions before their extraction in the source.

Sectional views of the sources (based on Balsiger et al. (2007)) are shown in figures 2.2 (SS) and 2.3 (OS).

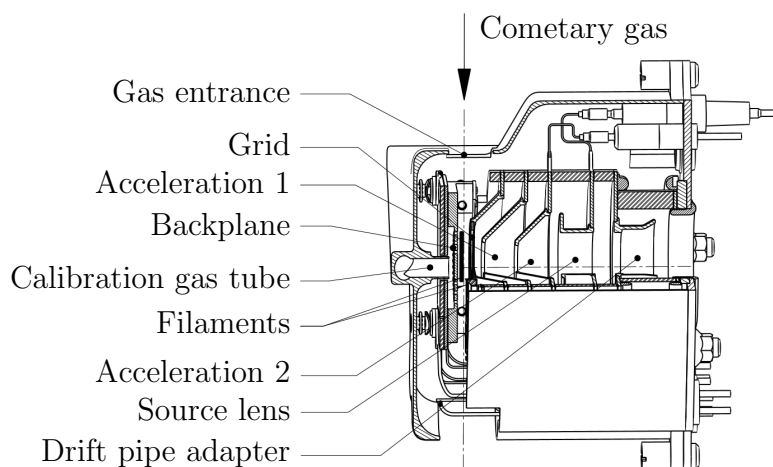


Figure 2.2: Sectional view of the Storage Source.

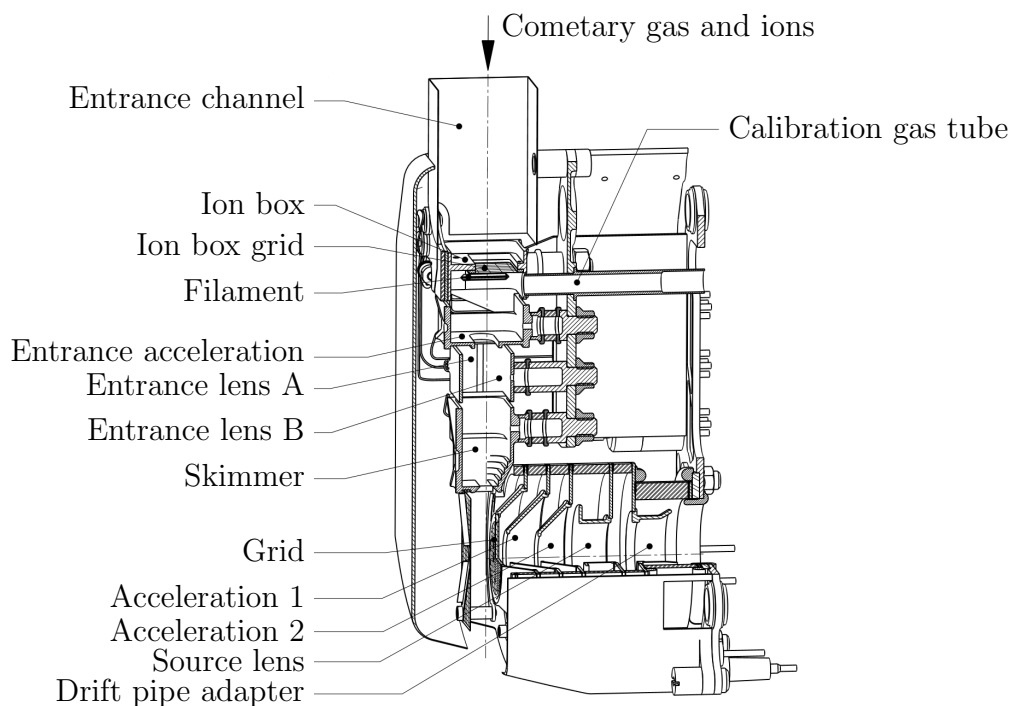


Figure 2.3: Sectional view of the Orthogonal Source.

Filaments

Four tungsten filaments are available for the electron impact ionization of the neutrals: two in the storage source (main + redundant), and two in the orthogonal source as well, although the primary goal of the latter is to measure ions. This double redundancy is justified by the lifetime requirements of the *Rosetta* mission, particularly critical for the filaments, combined with the fact that a failure of a filament would immediately make the measurement of neutrals impossible.

Only one filament is emitting at a time, creating an electron beam adjustable by two repellers, with an ≈ 70 eV energy. As we will see in the next chapters, due to the influence of the potentials of the backplane and the extraction grid, the electron energy will vary.

In the case of the SS, the space charge of the continuous electron beam creates an ion trap between the backplane and the extraction grid, keeping the ions in the source. With this storage, it is possible to detect a large fraction of the ions produced in the SS.

Extraction grid

The extraction grid has two purposes. The first one is to extract the newly created ions towards the acceleration electrodes: this is done by applying a 2 μ s pull-pulse on the grid. The second purpose is to act like a potential barrier for the ions to remain in the source between two pulses.

The extraction grid is actually a double-grid which reduces the penetrating electrical field and separates the ionization and acceleration regions (de Heer and Milani, 1991).

Typically, the extraction frequency is in the kHz range, and will be changed depending on the desired mass range: with a high extraction rate, the heavy ions do not have enough time to reach the detector before the next pulse happens. A low frequency allows the study of heavier masses.

Acceleration

In each source, three electrodes are accelerating the ions until they arrive in the drift tube. The accelerated ions are time-focused a few centimetres behind the source exit.

2.1.2 Drift tube

The drift tube is a field-free region measuring 83 cm, in which the ions, having different masses but the same given energy, get separated due to their different speeds. As an example, during their flight, for a drift voltage of $-3'000$ V, the ions have a typical energy of 3 keV.

2.1.3 Reflectron

As described in 1.4.2, the ions formed in the ion sources have an initial kinetic energy distribution. Ions with the same mass may therefore not have the same speed and arrive at different times, decreasing the mass resolution of the instrument. RTOF is therefore equipped with a reflectron. The principle is represented in figure 2.4.

For more details about the reflectron of RTOF, the reader is advised to refer to Hohl et al. (1999) and Scherer et al. (2006).

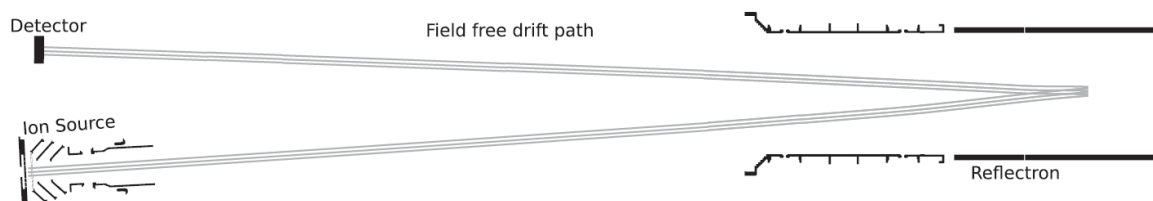


Figure 2.4: Single reflection. On the right side, the reflectron makes the ions turn around and refocus them in time on the detector. Picture based on Bieler et al. (2011).

2.1.4 Hard mirror

The use of additional electrostatic mirrors is another way to increase the flight path without increasing the physical dimensions: coupled with the reflectron, the hard mirror allows triple reflections in the instrument, multiplying the flight path by an additional factor of 2 (see figure 2.5).

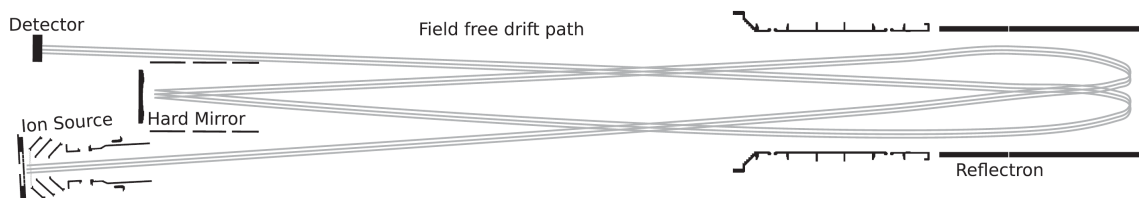


Figure 2.5: Triple reflection. On the right side, the reflectron. On the left side, the hard mirror reflects the ions which go back to the reflectron and to the detector, increasing again the flight path. Picture from Bieler et al. (2011).

2.1.5 Detectors

Both the OS and the SS detectors are equipped with microchannel plates assembled in chevron and amplifying the signal collected at the end by the anode (see 1.4.3).

2.1.6 Gas calibration unit

Two Gas Calibration Units (GCU) are able to fill the sources with a well known gas mixture of one third each of helium, carbon dioxide, and krypton. The gas inlet is reg-

ulated by a Pirani gauge, providing reliable and reproducible reference measurements. GCU spectra are mainly acquired in flight to get reference values for the application of the mass scale (C and t_0 , see 2.2.2) and for optimization purposes (see chapter 3).

2.1.7 Acquisition / electronics

The time of flight of the ions created in the two sources and amplified by two Micro-Channel Plates are processed by two data acquisition boards: the Equivalent Time Sampler (ETS) for the SS, and a simplified board for the OS, the ETS-Light (ETSL). Both data acquisition systems serve as Time-to-Digital Converters (TDC), recording the time when the signal exceeds a programmable trigger level. In the OS, such an *event* can be considered as a single ion when the density is low enough to consider that only one ion is hitting the detector at the same time. For the SS though, the ion density is supposed to be much higher due to the storage and leads to multiple ions arriving at the same time on the detector. To prevent an underestimation, the ETS system is also capable of converting the signal height into a digital value, or *histogram*, using 16 high-speed, low-power Analog-to-Digital Converters (ADC) fired with a 1.65 ns delay, consequently giving a time resolution for ETS of 1.65 ns.

These 16 ADCs do not all respond the same way, and create a pattern observed in the histogram data with a 16×1.65 ns redundancy. This pattern can be filtered with a specific factor for each ADC, calculated for instance via normalizing the $(n \times 16) + k$ points, with $k = 1 \dots 16$. This method has the advantage of having statistics on its side, with several tens of thousands of points in each spectrum. An example of this filtering is shown in figure 2.6.

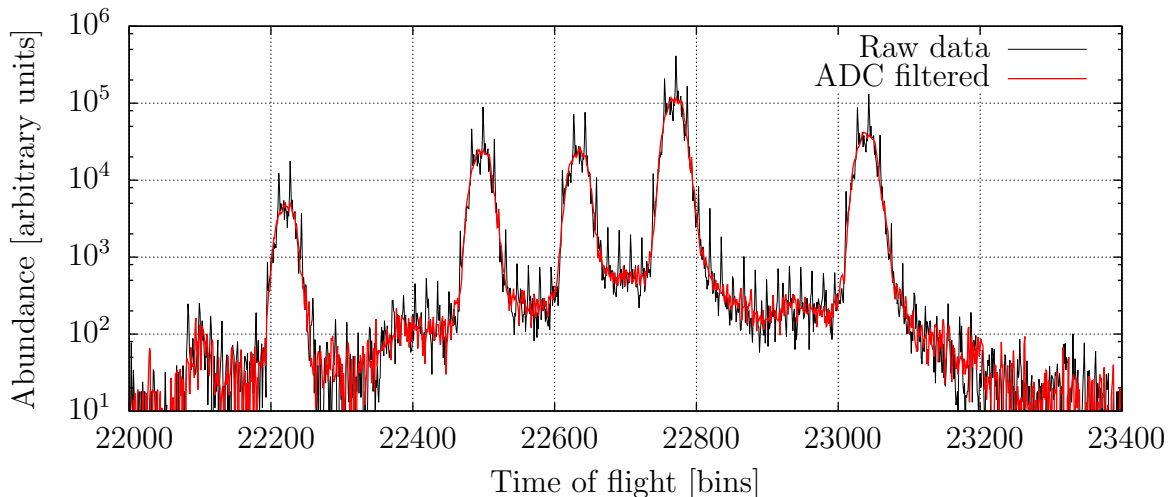


Figure 2.6: Krypton spectrum acquired with the RTOF FM on ground, showing the difference between raw data (black) and filtered data with ADC correction (red).

The ratio *histogram* / *events* is of high importance to estimate whether more than one ion hits the detector at the same time. If the ratio remains constant for the low intensity peaks as well as the high intensity peaks, then it is reasonable to consider

that one event corresponds to one ion (this is the case in figure 2.7). Otherwise, if the ratio increases for a high number of counts, then the event counts are underestimated for the peaks with a high signal. This saturation effect will be visible in chapter 4.

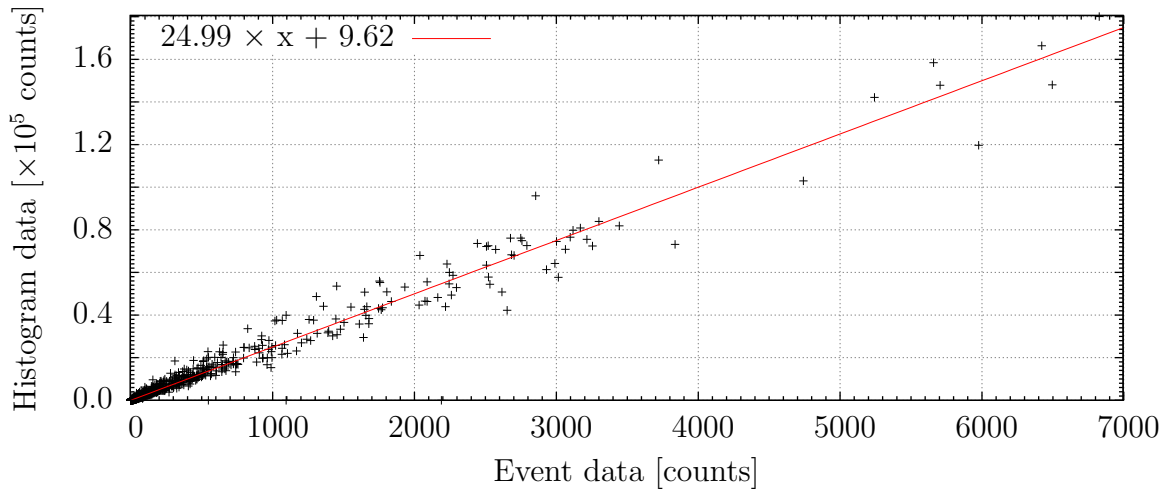


Figure 2.7: Constant histogram to event ratio.

Another saturation phenomenon can originate from the electronics: the ETS and ETSL are able to store a finite number of events during one single extraction, defined as the Mass Line Mode (MLM) number. This number is 31 for a 10 kHz extraction frequency, 63 for 5 kHz, and 255 for 2 kHz. If too many events happen during an extraction, the highest masses will be underestimated.

2.1.8 Operations

RTOF has several operation modes to ensure optimized scientific data acquisition. For each source, three different extraction frequencies are possible – 10 kHz, 5 kHz, and 2 kHz – and three different filament emissions are available – 200 μA , 100 μA , and 20 μA . Not all combinations are implemented in the DPU software: for instance and among others, the signal is expected to be too weak with a low emission associated to a low extraction frequency (an example is given in table 2.1 for the neutral measurements). The available modes and a few characteristics are listed in table 2.2.

Table 2.1: Combinations implemented in the DPU as modes (for the neutrals). F_{emi} = filament emission.

		SS			OS			
		Extraction frequency			Extraction frequency			
		10 kHz	5 kHz	2 kHz	10 kHz	5 kHz	2 kHz	
F_{emi}	200 μA	521	526	528	523	553		
	100 μA	511	516		513	543		
	20 μA	501	506		503	533		

Table 2.2: RTOF operation modes. The internal calibration modes have an extraction delay of 12'000 ns and a pulse width of 50 ns; the pulse height depends on the mode.
 * PC = pulser cross-talk. * BG = background measurements with attraction grid variations.

	Source	Mode	Extraction frequency [kHz]	Filament emission [μ A]	Acqu. time [s]	Remarks
	All	1	\emptyset	\emptyset	\emptyset	Standby
Heat.	SS	51	\emptyset	sub.	\emptyset	Heating of BP.SS (10 min)
	OS	53	\emptyset	sub.	\emptyset	Heating of BP.OS (10 min)
GCU	SS	161	10	20	200	GCU mode, equiv. to 501
	SS	171	10	100	200	GCU mode, equiv. to 511
	SS	181	10	200	200	GCU mode, equiv. to 521/522
	OS	163	10	20	200	GCU mode, equiv. to 503
	OS	173	10	100	200	GCU mode, equiv. to 513
	OS	183	10	200	200	GCU mode, equiv. to 523/524
Internal calib.	SS	211	5	\emptyset	10	Pulse height = 20 mV
	SS	221	5	\emptyset	10	Pulse height = 50 mV
	SS	231	5	\emptyset	10	Pulse height = 100 mV
	OS	203	5	\emptyset	10	Pulse height = 20 mV
	OS	213	5	\emptyset	10	Pulse height = 50 mV
	OS	223	5	\emptyset	10	Pulse height = 100 mV
PC*	OS	251	10	\emptyset	10	
	SS	253	10	\emptyset	10	
Neutral measurements	SS	501	10	20	200	
	SS	511	10	100	200	
	SS	521/522	10	200	200/400	
	SS	506	5	20	200	
	SS	516	5	100	200	
	SS	526/527	5	200	200/400	
	SS	528/529	2	200	400/400	
	OS	503	10	20	200	
	OS	513	10	100	200	
	OS	523/524	10	200	200/400	
	OS	533	5	20	200	
	OS	543	5	100	200	
	OS	553/554	5	200	200/400	
	Ion meas.	OS	504/514	10	\emptyset	200/400
OS		507/517	5	\emptyset	200/400	E1 = -7.7 V
OS		510/520	10	\emptyset	200/400	E1 = -5.0 V
OS		502/512	10	\emptyset	200/400	E1 = 0.0 V
Ion & neutral	BOTH	505	10	20	200	E1 = -7.7 V
	BOTH	515	10	100	200	E1 = -7.7 V
	BOTH	525	10	200	200	E1 = -7.7 V
	BOTH	555	5	20	200	E1 = -7.7 V
	BOTH	565	5	100	200	E1 = -7.7 V
	BOTH	575	5	200	200	E1 = -7.7 V
BG*	SS	621	10	200	200	E1 = -50.0 V
	SS	631	10	200	200	E1 = +50.0 V
Variation of E_{e^-}	SS	841	10 kHz	100	200	$E_{e^-} = 55$ eV RepA = -116 V RepB = -116 V
	SS	851	10 kHz	100	200	$E_{e^-} = 40$ eV RepA = -109 V RepB = -85 V
	SS	861	10 kHz	200	200	$E_{e^-} = 55$ eV RepA = -116 V RepB = -116 V
	SS	871	10 kHz	200	200	$E_{e^-} = 40$ eV RepA = -109 V RepB = -85 V

2.2 Data processing

2.2.1 Peak fitting & integration

Due to the spatial and kinetic energy distributions, peaks generated by a TOF mass spectrometer are expected to have a Gaussian shape. An instrument is nonetheless never perfect, and the use of a pseudo-Voigt profile appeared to be a better fit. The pseudo-Voigt function is an approximation to the Voigt function (eq. 2.1) defined as the convolution of a Lorentzian (eq. 2.2) and a Gaussian (eq. 2.3):

$$V_p(x) = \eta \cdot L(x) + (1 - \eta) \cdot G(x) \quad (2.1)$$

$$L(x) = \frac{A_0}{1 + \left(\frac{x-x_0}{2\sigma}\right)^2} \quad (2.2)$$

$$G(x) = A_0 \exp \left[-\left(\frac{x-x_0}{2\sigma}\right)^2 \right] \quad (2.3)$$

Therefore, a first method for the calculation of the area under each peak is to fit the data with a pseudo-Voigt profile, using the least squares method. The fitting is done either independently when the peak is clearly separated from its neighbors, or together with the closest peaks in the cases of krypton and xenon for instance, where an overlap of the isotopes can be observed (see figure 2.8).

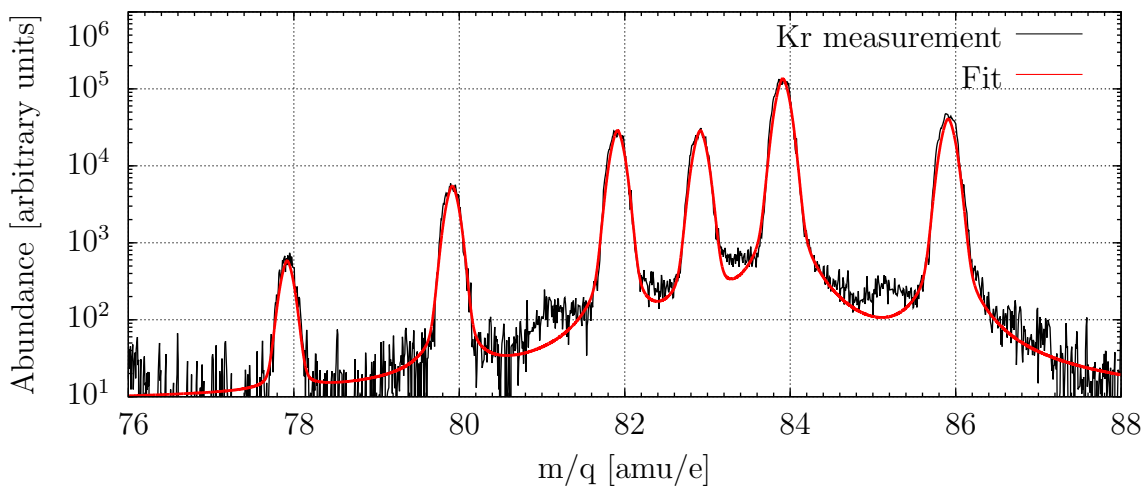


Figure 2.8: Zoom on the krypton isotopes region of a spectrum acquired on ground with the SS with a krypton gas inlet of $1.0 \cdot 10^{-7}$ mbar. The overlap of the peaks influences the area under the neighboring peaks on the percent level, and therefore fitted together as a sum of pseudo-Voigt profiles.

Due to a possible irregular peak shape, a numerical integration might be preferred to the fitting. When the peaks are isolated, calculating the sum of all the counts within 3σ around the peak centroid is the simplest and most efficient way to integrate the peak numerically. In case of an overlap, like in figure 2.8, more sophisticated methods like Monte Carlo integration or Simpson's rule might be used, and were considered; in this work though, the peaks will always be isolated enough so that a simple numerical sum would be possible, except for the calibration of krypton and xenon in chapter 4.

2.2.2 Mass scale calibration

The first step for the identification of peaks in a spectrum is to apply a mass scale. Starting from equation 1.3 (rewritten below), one can derive equation 2.4, linking the mass to the time of flight of the ions:

$$t = d \cdot \sqrt{\frac{m}{2qU}} \quad (1.3)$$

$$m = \left(\frac{t - t_0}{C} \right)^2 \quad (2.4)$$

where t is the time needed for an ion of mass m to reach the detector. C and t_0 are constant parameters which can be calculated according to equations 2.5 and 2.6, provided that at least two peaks can already be identified. For instance, for a krypton spectra acquired with the SS in mode 521, the mass scale was applied using 4 reference peaks as shown in table 2.3.

$$C = \frac{N \sum_{i=1}^N t_i^2 - \left(\sum_{i=1}^N t_i \right)^2}{N \sum_{i=1}^N (\sqrt{m_i} t_i) - \sum_{i=1}^N \sqrt{m_i} \sum_{i=1}^N t_i} \quad (2.5)$$

$$t_0 = \frac{\sum_{i=1}^N (\sqrt{m_i} t_i) \sum_{i=1}^N t_i - \sum_{i=1}^N \sqrt{m_i} \sum_{i=1}^N t_i^2}{N \sum_{i=1}^N (\sqrt{m_i} t_i) - \sum_{i=1}^N \sqrt{m_i} \sum_{i=1}^N t_i} \quad (2.6)$$

N is the number of reference peaks ($N \geq 2$), t_i the time of flight of the i^{th} peak, and m_i its associated theoretical mass. The theoretical masses are calculated using the Handbook of Chemistry and Physics database (Haynes); the mass of an electron has been subtracted, and the peak position is determined using a pseudo-Voigt profile fitting as described in the previous section.

For the SS, with the reference peaks in table 2.3, and for the spectrum shown in figure 2.8, $C = 2'482.30 \text{ bins} \cdot \text{u}^{-0.5}$ and $t_0 = 30.79 \text{ bins}$.

Table 2.3: Time of flight of the four reference peaks used for the calculation of C and t_0 . The deviation represents the difference between the theoretical mass and the mass re-calculated according to C and t_0 .

i	Reference peak	Theoretical mass m_i [u]	Time of Flight t_i [ns]	Deviation [ppm]
1	H ₂ , residual	2.0151	5'865.2	-92
2	H ₂ O, residual	18.0100	17'432.2	56
3	CO ₂ , residual	43.9893	27'216.1	-9
4	⁸⁴ Kr, gas inlet	83.9109	37'569.6	-4

2.3 Status in flight

FM / FS

It is standard practice, after a prototype has been made and the Engineering Qualification Model has been tested, to build a space instrument in duplicate: a Flight Model (FM), and a Flight Spare (FS), in case a problem would occur before launch with the FM. For RTOF, tests performed on both the FM and the FS models revealed that better performances were obtained with the FS, in particular regarding the ADC noise and the mass resolution. Consequently, the RTOF FS was chosen for flight, and the RTOF FM remained on the ground for test purposes.

After the exchange, the RTOF FM was refurbished to be used on the ground as a spare. In the following, *FM* will always stand for *FM refurbished*. For additional information, the reader is advised to consult the technical document *RO_ROS_Tech_1107, RTOF Refurbishing*.

An anecdotal, but very useful, way not to be mistaken between the lab and the flight model is to remember FS as *Flight Space* and FM as *Flight à la Maison* (K. Altwegg, pers. comm.).

9 kV high voltage converter

A few months after the *Rosetta* launch, in September 2004, although the commissioning of the ROSINA instrument was performed nominally, a strange behavior of the RTOF FS was observed, consisting of partial discharges occurring when the 9 kV high voltage converter was being switched on. After a few months of instabilities, in March 2005, the highest voltage achievable decreased to less than 3'000 V. A similar failure could be reproduced in the lab after some years, providing an explanation about this behavior: outgassing in the potting near the high voltage converter was leading to some partial discharges along some of the potted cables.

A solution, found by electronic engineers from the University of Bern, was to switch the 9 kV converter ON and OFF at regular intervals, and resulted in RTOF working in a stable state without any discharges (Altwegg, 2010). After a few months of tests on ground with the RTOF FM, the solution was successfully tested in space on the RTOF FS in February 2010, with lowered voltages and a drift of -1'000 V.

Once it was demonstrated that RTOF could be operated with a drift voltage of $-1'000$ V without risking a more major failure, it was decided to increase the voltages to higher values, with $D = -1'800$ V, to get closer to the initial performances of RTOF. This was done on ground only, as *Rosetta* had to go into its hibernation phase. Unfortunately, the failure in space was more critical than on ground, and after the hibernation, despite reasonable performances obtained in the lab with $D = -1'800$ V, it was concluded that such a value could not be reached with the RTOF FS; a drift value of $-1'000$ V was concluded and has been used in space since April 2014.

Regulating the 9 kV converter requires an electronic workaround which directly impacts the operations of RTOF: the new regulated voltage needs to be applied somewhere in the HV board, and even if this voltage is not physically applied, the corresponding electrode cannot be used any more. When the SS is measuring, the regulation voltage is applied on the OS source lens. When the OS is measuring, the regulation voltage is applied on the SS source lens. And when both the SS and the OS are being used together, the regulation voltage is applied to the hard mirror. This means that the triple reflection, which requires the use of the hard mirror, is impossible with both the SS and the OS together.

Cover

As we will see in chapter 5, the baseline between the peaks varies very rapidly; the cover was set to position 14 on 05/11/2014 (meaning 2/3 closed or opened with an angle of $\approx 42^\circ$) to try to reduce these variations. As no significant increase of the quality could be observed, the cover was set back to position 1 on 10/04/2015.

MCP voltages

One main difference between the RTOF FM and the RTOF FS is the voltage applied to the two MCPs. It is $2'650$ V for the FM, and has been increased for the FS from $2'700$ V to $2'750$ V on 08/04/2015.

SS filament

In flight, on 27/05/2015, and during the first switch ON after a standard maneuver, the SS filament #1 ceased emitting electrons, as it could not be powered with more than 30 mA – far less than the usual 950 mA needed to emit a $200 \mu\text{A}$ -electrons beam. As a consequence, the redundant SS filament (number #2) was used. The origin of the SS filament #1 failure is still not clear, but a rupture of the filament is considered, due to the harsh conditions in the vicinity of the comet.

3. Optimization

After the 9 kV high voltage converter issue (see 2.3), each time the maximum available voltage was lowered, new optimized settings had to be found for these new configurations. These optimizations are presented in this chapter as follows: on-ground optimizations will be briefly detailed in a first part, and a second part will be dedicated to the in-flight performances achieved with the settings found on the ground, and followed with in-flight fine tunings. The goal of the optimizations on the ground being to increase the performances of RTOF in flight, emphasis will be placed on the optimization of the RTOF FS.

In the following, the different settings applied to RTOF will be referred to as “ $D = -3'000 \text{ V}$ ”, “ $D = -1'800 \text{ V}$ ”, or “ $D = -1'000 \text{ V}$ ”: the drift voltage D is one of the voltages the most affected by the decrease of the maximum voltage available (see 2.3), and will be used to differentiate the main RTOF voltage settings.

3.1 On-ground optimizations

As the 11 (SS) to 15 (OS) parameters are to be optimized together (see appendix A), a manual optimization may not be the best choice to reach optimum parameters in a short amount of time. The necessity of having an autonomous process is even more self-evident when it comes to flight instruments: the study of bodies in more and more remote regions of our Solar System induces long travel times, during which the performance of an instrument could decrease due to aging or to other environmental factors such as the temperature. Moreover, the long distances involved make manual optimization more than difficult due to the waiting time needed to send commands and receive acknowledgements back on Earth. For these reasons, an Adaptive Particle Swarm Optimization (APSO) algorithm has been developed by A. Bieler at the University of Bern and has been successfully implemented on several TOF mass spectrometers (Bieler et al., 2011).

The particle swarm optimization was first developed by Kennedy and Eberhart (1995), and is a stochastic population-based optimization technique inspired by social behavior of some animals, such as bird flocking. A swarm of potential solutions (or set of voltages) called *particles* is spread in the solution space where an optimum has to be found; these particles, following simple motion rules, converge gradually towards a local maximum.

The optimization algorithm was first used on the RTOF FM with $D = -1'800$ V, i.e. after the 9 kV failure and during the hibernation or the RTOF FS, and resulted in an increase of a factor 2.5 to 4 in the intensity of the peaks compared to the best results obtained with a manual optimization, and the mass resolution was almost doubled (Bieler et al., 2011). However, due to the more positive drift voltage, the mass resolution suffered: starting from an initial typical mass resolution of 950 at mass 44 and at 50 % peak height for $D = -3'000$ V, this value was reduced to 540 for $D = -1'800$ V.

The two sets of voltages associated to $D = -3'000$ V (software version 6.7 FS) and $D = -1'800$ V (software version 8.5 FS) are summarized in tables A.1 and A.3, and the peak shape differences between them for the OS are shown in figure 3.1. The decrease in the signal intensity is obvious, but thanks to the optimization, the science requirements were still met (Balsiger et al., 2007), with a mass resolution greater than 500 and a mass range greater than 1'800 u/e. The evolution is similar for the SS, and the evolution of the sensitivities will be discussed in chapter 4.

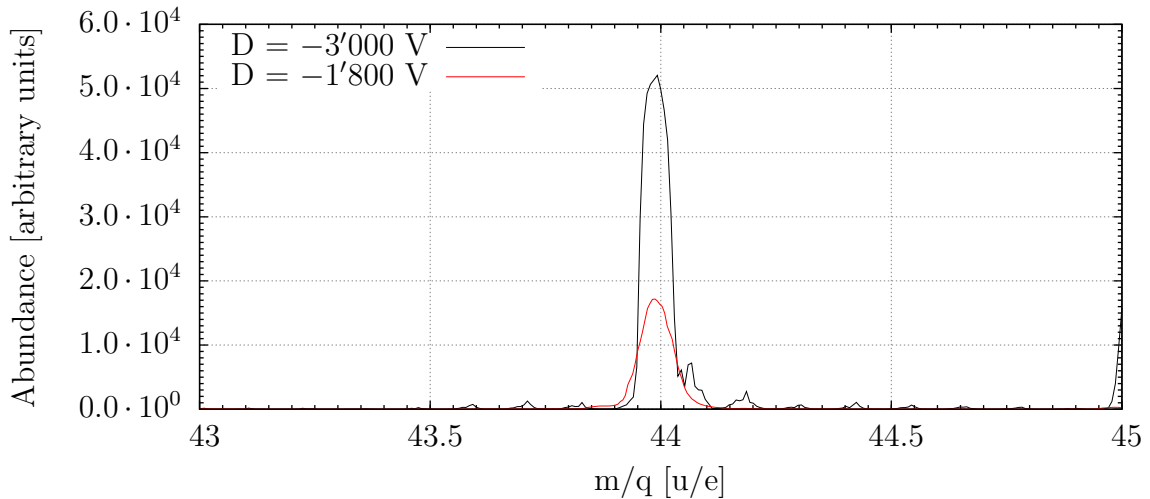


Figure 3.1: Comparison between the initial RTOF FM settings with $D = -3'000$ V and lowered optimized settings with $D = -1'800$ V, for the OS in mode 513 and a CO_2 gas inlet of $1.0 \cdot 10^{-7}$ mbar.

After the end of hibernation and the realization that high voltages with $D = -1'800$ V could not be reached with the RTOF FS, the first step on the ground was to launch an optimization starting from the Lutetia settings (equivalent to the settings from the software version 8.5 FS in table A.1). The best results obtained in the $D = -1'000$ V configuration after optimization are compared with the best results obtained in the $D = -1'800$ V configuration in figure 3.2 for the OS. The results for the SS are similar.

Once more, a decrease of the performances had to be expected and the mass range was almost reduced by a factor of 2, with a typical mass resolution of 450 at 50 % peak height for CO_2 .

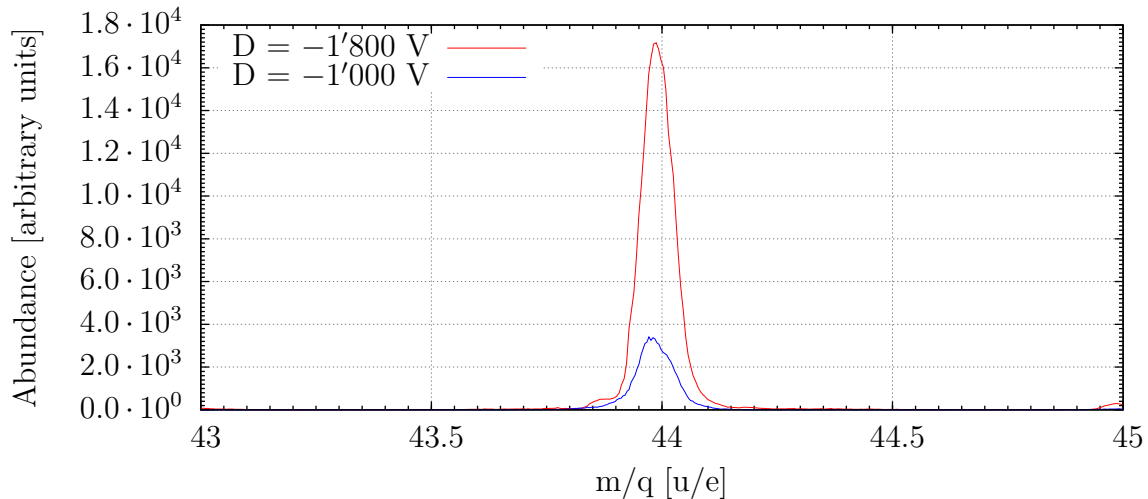


Figure 3.2: Comparison between the RTOF FM settings with $D = -1'800$ V and with $D = -1'000$ V, for the OS in mode 513 and a CO_2 gas inlet of $1.0 \cdot 10^{-7}$ mbar. The red curve for $D = -1'800$ V corresponds to the red curve from figure 3.1.

The optimized settings were uploaded to the DPU in flight in September and October 2014 for the SS and the OS respectively. These values, set with the software version 8.8 FS (see tables A.1 and A.3) for the SS and the OS, were the starting points of the in-flight optimizations.

3.2 In-flight optimizations

Because it has the advantage of being autonomous and very efficient, the APSO algorithm was one of the most viable possibilities to increase the performance of the RTOF FS, and it was naturally planned to use it in flight. Despite a substantial investment of time into implementing the APSO algorithm in the DPU software, the automatic optimization could never be successfully performed in space, as the best results found by the algorithm were not reproducible: either the housekeeping values displayed were incorrect, or the spectra recorded during the optimization process were incorrect – both cases being almost impossible. As of today, this behavior remains unexplained, but due to a lack of understanding and a limited amount of time for optimization, it was decided to optimize the RTOF FS manually, using the lab instrument as reference for space.

Although very similar, the FS and the FM do not respond exactly the same way to a commanded voltage, which is typical due to the precision of the digital-to-analog converters converting the commanded value to an actual voltage, and due to slight differences in mechanical dimensions and the shape of the filaments. Therefore some fine tuning was necessary after applying the optimized voltages found on the ground. The performance and results from these tunings are presented below, for each source; the voltages are given in table A.3.

3.2.1 RTOF/SS

The timeline for the RTOF SS optimization in space between the end of hibernation beginning of 2014 and June 2015 consists of six steps, detailed in the next paragraphs. For each step, the CO_2 peak of a GCU spectrum (histogram data) is shown: the plain red curve corresponds to the current step, and the dashed gray one to the previous step, for comparison. The data are corrected for the ADC pattern, but are not corrected for sensitivity.

1. 20/04/2014 – SW v8.5 FS Initial functional set of voltages, based on the settings used during the Lutetia fly-by (figure 3.3).

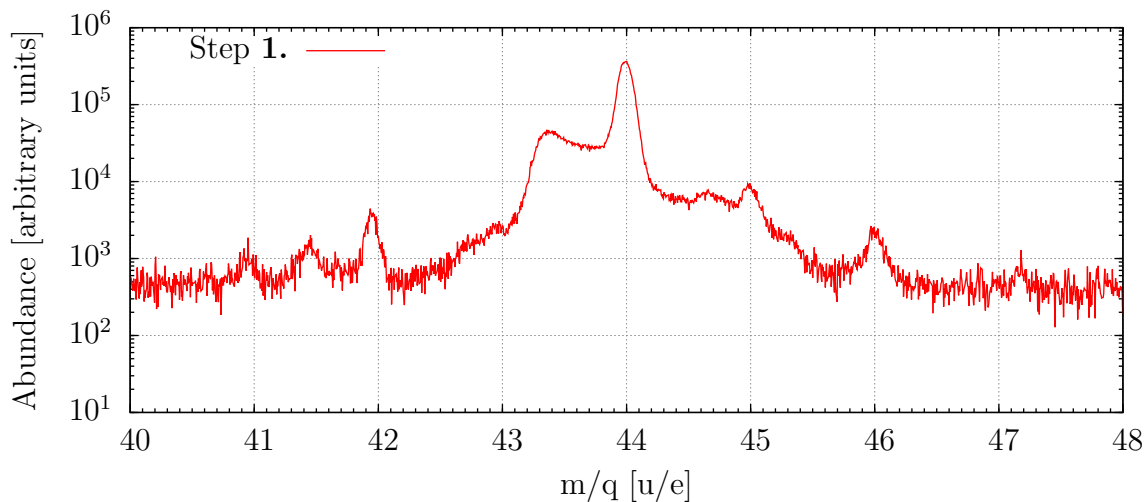


Figure 3.3: Step 1.

Far from a perfect gaussian, the peaks present some “shoulders” on their left side (20 % of the main peak height, 0.6 u/e lighter) and on their right side (2 % of the main peak height, 0.4 u/e heavier, difficult to see here because of the proximity of the peaks but clear for isolated compounds like CO at mass 28), indicating that there’s still room for improvement.

The peaks on the left side (masses 41, 41.5, and 42) correspond to the doubly charged krypton isotopes; on the right side (masses 45 and 46), the CO_2 isotopologues.

It is already important to take note of the high level of the baseline between the peaks, which will be discussed in step 2. and in chapter 5.

2. 02/09/2014 – SW v8.8 FS Upload of new parameters for the RTOF FS after optimizing the RTOF FM (figure 3.4).

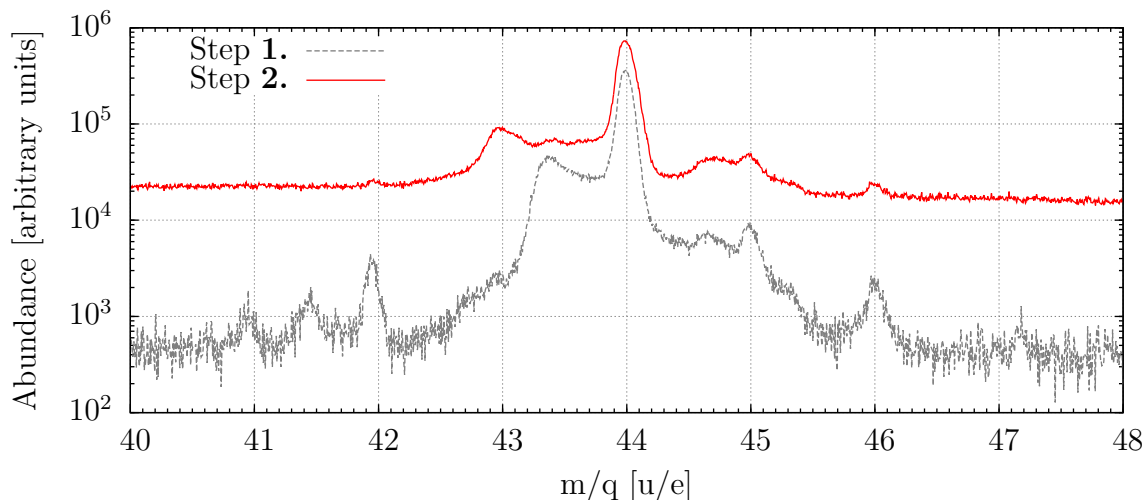


Figure 3.4: Comparison between step 1. and step 2.

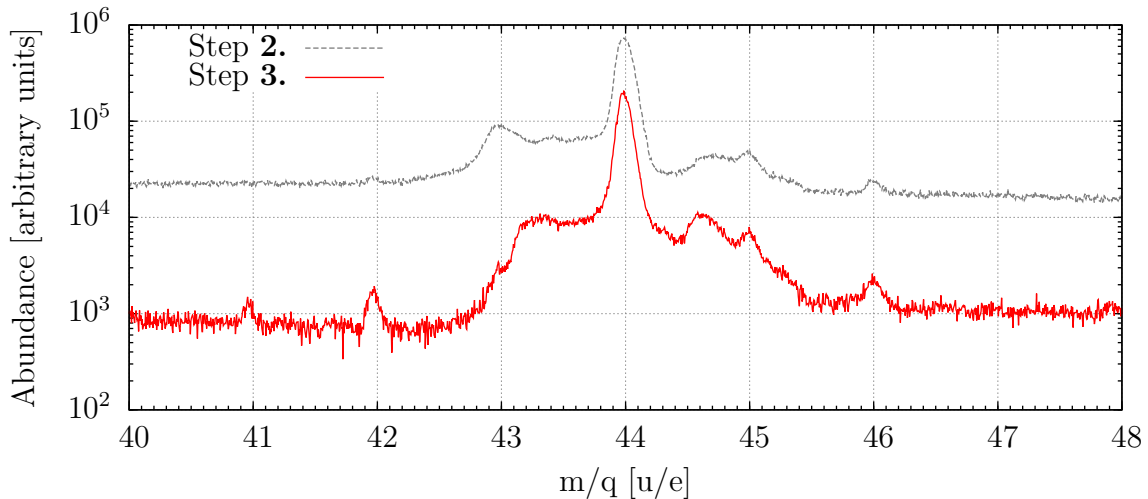
After a few months of optimization in the lab, new parameters were uploaded in flight. The main changes concern mostly the ion source voltages, with more negative values for BP, A2, and SL, a more negative RL as well, and a more positive P (see table A.3, software version 8.8 FS).

However, the comparison with the Lutetia settings is complicated by the high level of the baseline between the peaks. This phenomenon, most probably linked to the solar radiation, will be investigated in chapter 5. Even with a high baseline level, the intensity of the left feature represents now 10 % of the intensity of the main peak.

As a general behavior, it is expected to observe fewer doubly charged ions with a lower BP value, as it changes the potential of the ionization region, located between the ion source backplane and the extraction grid. The electrons are emitted from the filament with a potential of -70 V, and reach the ionization region with a lower energy for a lower BP (or GR) voltage, therefore creating fewer doubly charged ions (and potentially less fragments, but this point will be addressed in chapter 4).

3. 03/10/2014 – SW v8.8 FS First short optimization matrix with the RTOF FS (figure 3.5), consisting of trying a few configurations with different ion source voltages (BP, GR, P, RepA, and RepB).

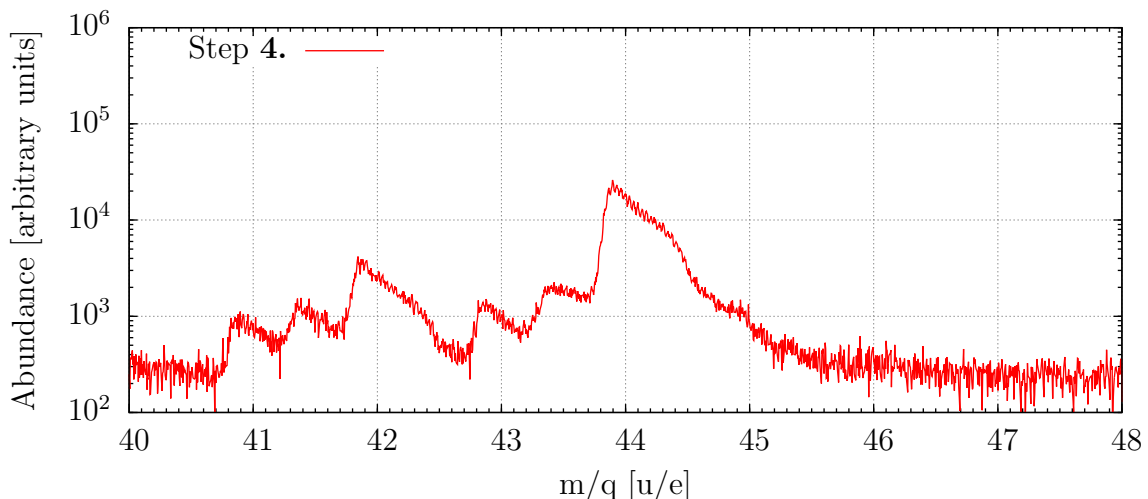
The main change between step 2. and step 3. concerns only the ion source settings BP, GR, P, and the repellers. The idea of this step was to optimize the initial ion distribution in the ion source, to get a better peak shape. Put in another way, and by analogy with optics, the idea was to improve the quality of the *object* (i.e. the pool of newly created ions in the source) without changing the *ion optics* (i.e. the voltages on the acceleration and reflectron electrodes), to see an improvement in the resolution of the *image* (i.e. getting a smaller temporal distribution on the detector, and hence a narrower peak).

Figure 3.5: Comparison between step **2.** and step **3.**

With a baseline back to the 10^3 level, the details are easier to compare and although the intensity of the peak is 50 % lower with **3.** than with **2.**, the peak shape looks better with side features at only 5 % of the main peak height.

After this step, a problem with the ADC #1 in the RTOF FM ETS board made the use of the SS impossible on the ground until March 2015; during this time, efforts focussed on the optimization of the OS.

4. 08/04/2015 – SW v8.9 FS Test of different settings found on the ground (figure 3.6).

Figure 3.6: Step **4.**

Once the ADC #1 was fixed, optimizations on the ground started again and a new optimum was found for the RTOF FM, with “exotic” values for BP and GR: both positive,

and GR at the maximum limit of 50.0 V. These settings were tested in space but the results were completely different from the ones on the ground, and the performances of the flight instrument were much lower in this configuration.

5. 11/05/2015 – SW v8.A FS Same settings as step 3.

Additionally to coming back to step 3., in order to prevent a saturation of the acquisition boards, which are limited to 31 ions per extraction for the 10 kHz modes, the threshold level was increased by 1 step, decreasing the baseline level between the peaks. Finally, in an attempt to increase the overall signal, the MCP voltage was increased by 50 V to 2750 V.

The effect is visible in figure 3.7: the signal-to-noise ratio is globally the same, but the number of counts is lower, and the peak shape is the same.

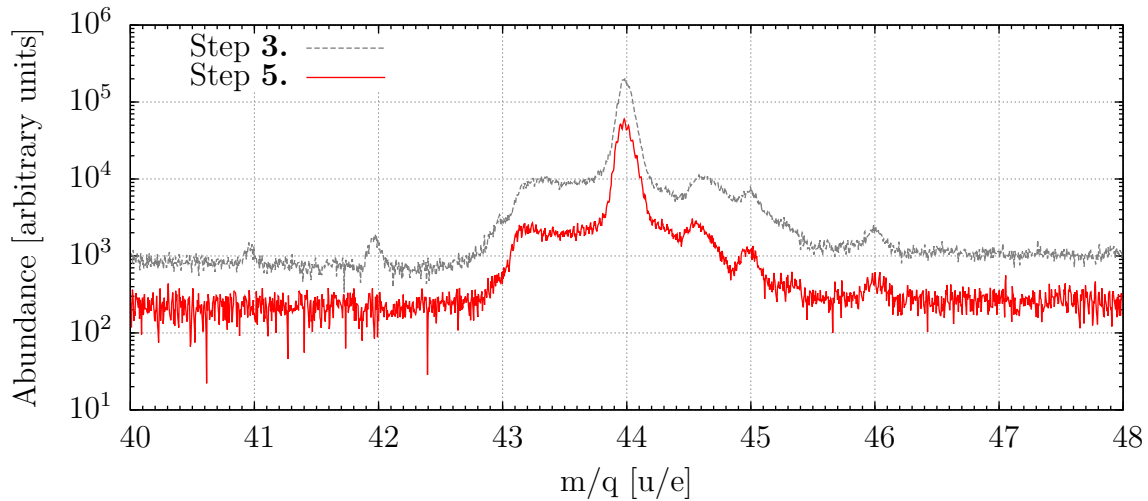


Figure 3.7: Comparison between step 3. and step 5.

6. 15-20/04/2015 and 13-18/05/2015 – SW v8.A FS Global optimization matrix.

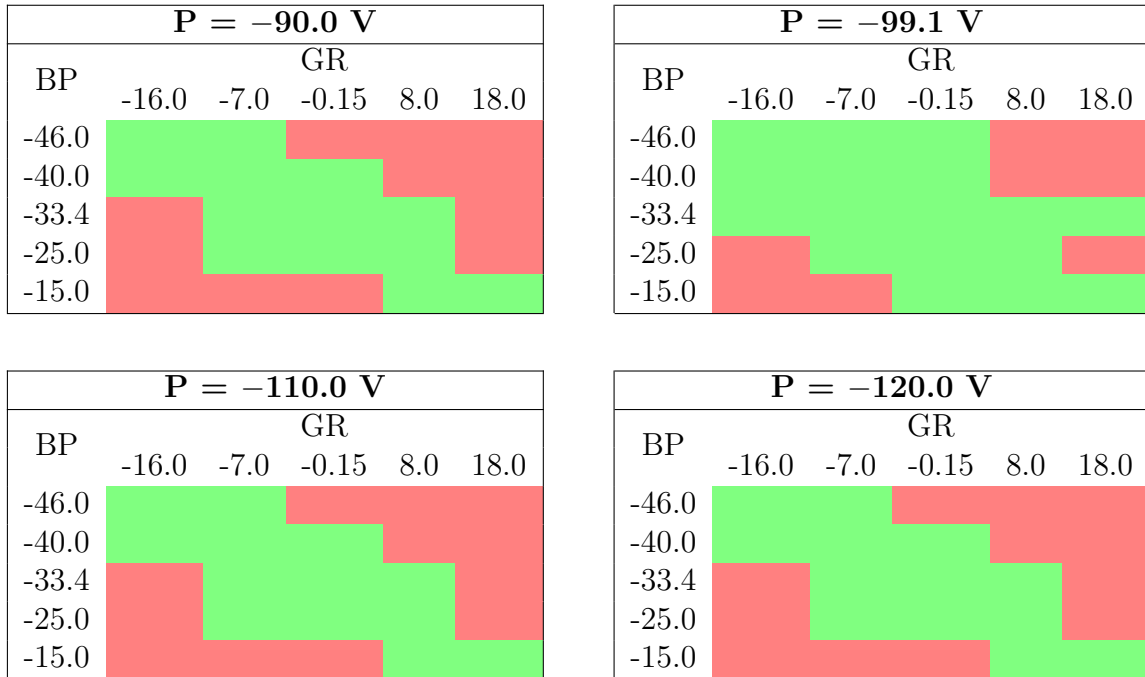
At this point, it became clear that a global characterization of the ion source settings was needed to get a real improvement. This was the purpose of the optimization matrix done with the settings from the table 3.1.

Table 3.1: Commanded values for BP, GR, and P, in V.

BP	GR	P
-46.0	-16.0	-120.0
-40.0	-7.0	-110.0
-33.4	8.0	-99.1
-25.0	0.15	-90.0
-15.0	18.0	

The optimization matrix contained relevant combinations of BP, GR, and P, in a way which would minimize the number of permutations to avoid an overload in the stack of commands sent to the DPU in flight. The selected combinations are shown in table 3.2.

Table 3.2: Optimization matrix for BP, GR, and P. The green boxes correspond to the combinations commanded. Red were excluded as they were not considered as relevant, based on previous optimizations. All voltages are in V.



The analysis of the spectra acquired with the ion source settings selected in table 3.2 reveals two distinct behaviors for two different populations of peaks: masses 12 and 19, on one side, and all the other peaks on the other side, i.e. the GCU peaks He, O, CO, CO₂, Kr, and the H₂O peak of cometary origin.

The peaks at masses 12 and 19 are not expected to be real compounds, as their “masses” actually change when the reflectron voltages are changed. A link with a possible sputtering or with the electronic pattern discussed in 2.3 is still under debate.

Figure 3.8 shows the difference between CO₂, representing the second group above, and the peak at mass 19. Figure 3.9 summarizes the 3D maps in a qualitative manner. Several observations can be drawn from these maps and from the previous optimizations:

- With the current reflectron and acceleration voltages, the best intensities are obtained with $P = -90.0$ V.
- Likewise, the best intensities are found for a difference of 40.0 V between GR and BP, independently of P.
- Doubly charged ions are much more abundant with positive BP and GR.
- Masses 12 and 19 appear for a difference of 20.0 V between GR and BP, and for BP greater than -35 V.

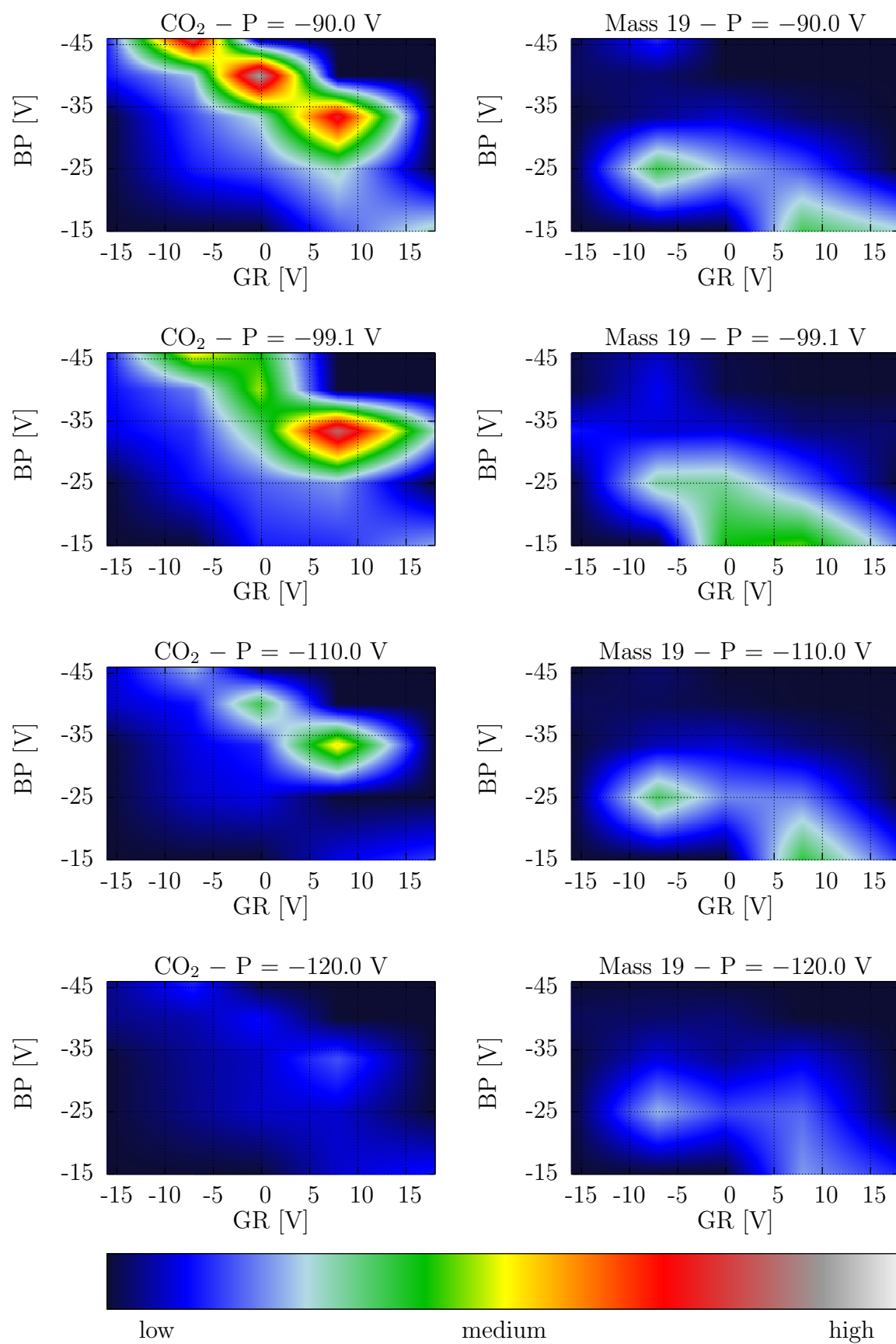


Figure 3.8: Intensity of the CO_2 peak (left) and of the peak at mass 19 (right) with respect to the BP and GR voltages.

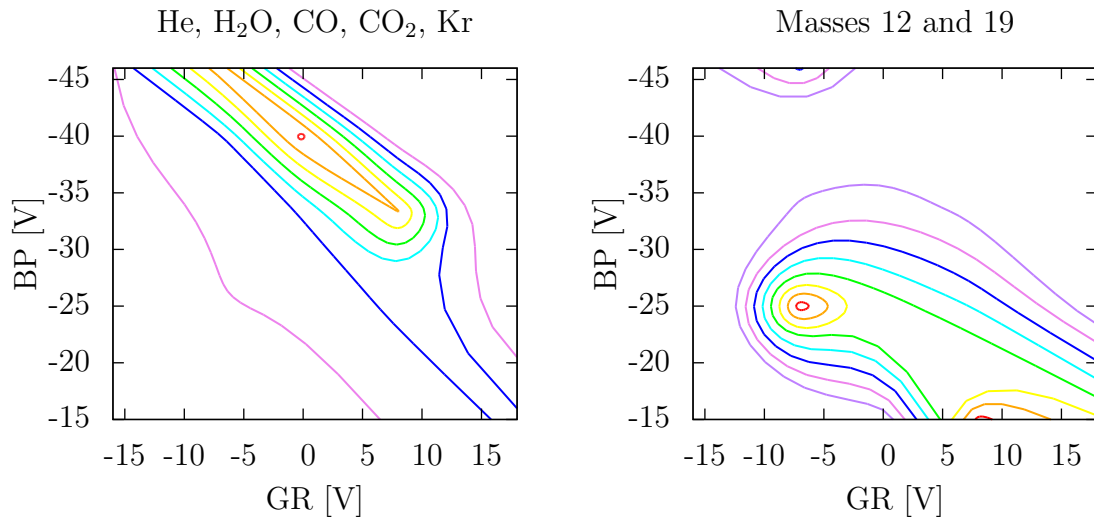


Figure 3.9: Local maximal intensities of two kind of peaks, with respect to BP and GR. On the right side, masses 12 and 19. On the left side, all the other peaks.

In light of the results obtained, the settings chosen for the ion source are $BP = -40.0$ V, $GR = 0.0$ V, and $P = -90.0$ V. In this way, a maximal intensity is reached for the masses known to be *real*, and the maximum of intensity for the peaks at masses 12 and 19 is avoided. The spectrum associated with these parameters is compared to the previous settings in figure 3.10.

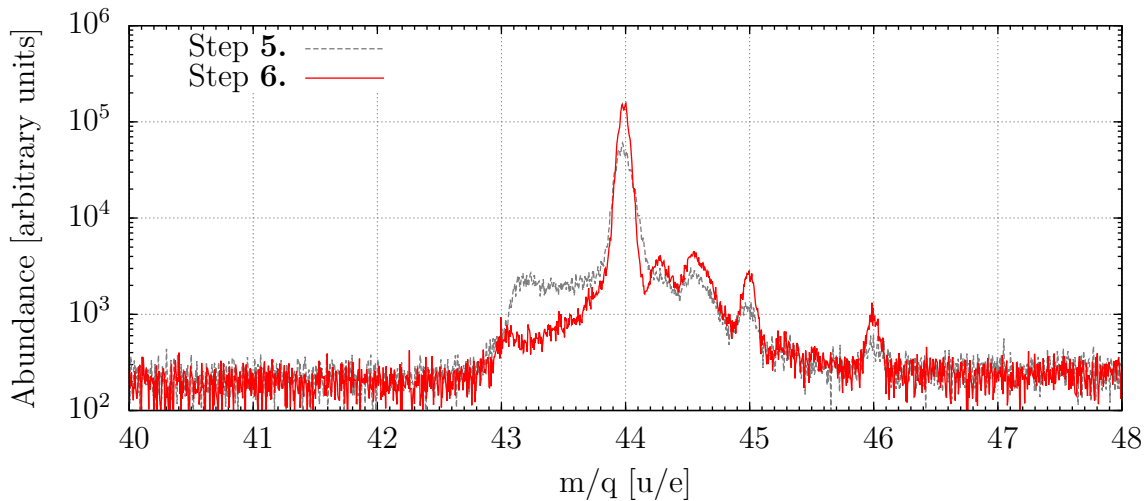


Figure 3.10: Comparison between step 5. and step 6.

The new settings present the double advantage of increasing the intensity of the main peak by a factor of 2, with a significant diminution of the left shoulder and an increase in the mass resolution. Two trailing peaks remain visible at $+0.25$ u/e and $+0.55$ u/e, representing a few percent of the main peak height.

Summary and perspectives – SS

Figure 3.11 summarizes the evolution of the mass resolution and the signal-to-noise ratio as a function of the step number. Such an encouraging progression between steps **5.** and **6.** led to the planning of step **7.**, where a fine tuning of the reflectron voltages was intended to get rid of the two trailing peaks.

The filament #1 failure at the end of May 2015 and the switch to the redundant filament #2 demonstrated otherwise (see 2.3): all the other settings being the same, and even with a symmetric geometry between the two filaments, the intensity of the signal falls by a factor of 100 when filament #2 is used.

In sum, a whole new optimization is needed with the new filament, and is being performed as of the time of writing, starting with a promising optimization on the RTOF FM, which will most probably be followed with tests with the RTOF FS.

As a tool for the analysis of space data and because these values changed quite often between April 2014 and June 2015, typical C and t_0 values are given in table 3.3. These parameters are defined in 2.2.2.

Table 3.3: Typical C and t_0 values for the different optimization steps of the SS. The settings from step **6.** tested in May were uploaded in flight after the filament failure and were therefore never used.

Step	Start	End	C	t_0
1.	24/04/2014	02/09/2014	3165.78	26.93
2.	02/09/2014	03/10/2014	3104.40	27.35
3.	03/10/2014	08/04/2015	3127.13	27.80
4.	08/04/2015	11/05/2015	3116.29	37.61
5.	11/05/2015	05/06/2015	3127.13	27.80
6.	05/06/2015	—	3130.76	28.21

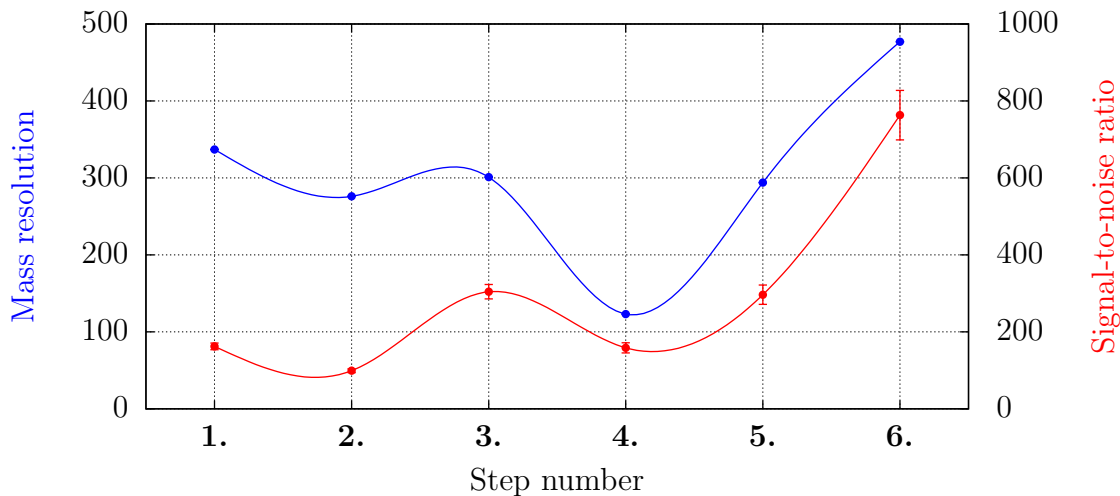


Figure 3.11: Evolution of the mass resolution (50% peak height, mass 28) and the signal-to-noise ratio with respect to the optimization step number.

3.2.2 RTOF/OS

The optimization of the OS for neutral particles was performed in September 2014, when the on-ground optimization of the SS had to be paused due to a failure of one of the ADCs in the ETS acquisition board. It consisted of one major change in the voltage settings after the first post-hibernation spectrum acquired on 24/04/2014. The optimized settings were found after 5 days of on-ground optimization with the FM and uploaded in the DPU aboard the *Rosetta* spacecraft on 17/10/2014.

A spectrum acquired with the optimized settings is compared to the initial settings in figure 3.12, and average values for C and t_0 are indicated as well in table 3.4.

The major changes concern the mass resolution, which increased almost by a factor of 2 (from 182 to 332), and the intensity of the peaks, which improved by 50%. The high level of the baseline between the peaks is most likely due to the solar radiation rather than to the settings themselves (see section 5.1).

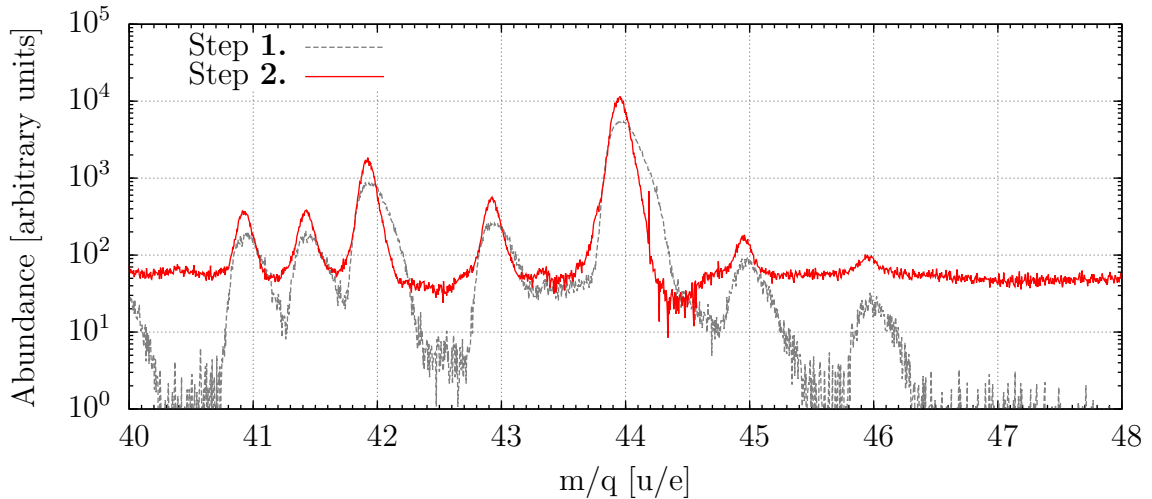


Figure 3.12: Comparison between initial (step 1.) and optimized settings (step 2.)

The optimization of the OS for the ions follows the one for the neutrals, as both modes share the same settings for the drift, the acceleration electrodes and the reflectron. Regarding the other voltages, the procedure was the same as for the neutrals: after an optimization campaign performed by A. Jäckel on the ground (pers. comm.), three sets of voltages were defined with different settings for the ion source and the entrance potentials, covering three possible energy ranges for the ions to be measured.

The voltages are summarized in table A.2. As no ions could be clearly seen with the RTOF FS yet due to large distances from the comet and low outgassing, no ion spectra are shown here.

Table 3.4: Typical C and t_0 values for the different optimization steps of the OS.

Step	Start	End	C	t_0
1.	24/04/2014	17/10/2014	3'092.49	29.07
2.	17/10/2014	—	3'055.09	28.30

4. Calibration

In this chapter, three calibration campaigns will be presented, for three of the states detailed in chapter 3:

- Early calibration done before flight (Sinzig, 2003) with a drift voltage of $-3'000$ V
- New calibration performed on ground during the hibernation of *Rosetta* with a drift voltage of $-1'800$ V
- Newest calibration performed on ground with a drift voltage of $-1'000$ V

Data from the early calibration have been re-analysed for this work and will be presented in the first section. The purpose of this analysis, in addition to creating a reference point to be used for the extrapolation detailed at the end of this chapter, is to check the validity of the integration methods described in 2.2, and to demonstrate the initial capabilities of RTOF. For this reason, data acquired in 2002 and 2003 with CO_2 , Kr, and GCU gases have been analysed.

The design of the experiments for the new calibration performed with $D = -1'800$ V, presented in the second section, was based mainly on the work of Bockelée-Morvan et al. (2004), which listed production rates relative to H_2O from *in situ* measurements and spectroscopic observations of several well-documented comets near their perihelion. The complete list of the studied compounds is shown in table 4.1 p. 41. The Chemical Abstract Service (CAS) registry number, a numeric identifier used to classify organic and inorganic compounds, is given in the table as well. In this section, the species will be gathered according to their atomic composition:

- H_2O , CO, CO_2
- Noble gases
- C-H-bearing compounds, i.e. alkanes, alkenes, aromatic hydrocarbons
- C-H-O-bearing compounds, i.e. alcohol, carboxylic acids, aldehydes
- C-H-N-bearing compounds, i.e. hexamethylenetetramine, triazine
- C-H-O-N-bearing compounds, i.e. urea, formamide, glycine

In a third and last section, the results of the calibration done with $D = -1'000$ V with H_2O , CO, CO_2 , and Kr will be presented and extrapolated to create a database to be used for the analysis of the RTOF FS data.

Table 4.1: List of calibrated compounds. **Mass* is rounded to the closest integer. ***State* is given for 20 °C & 1 atm.

Type	Chemical family	Name	Formula	Mass* [u/e]	N° CAS	State**
H ₂ O, CO, CO ₂		Water	H ₂ O	18	7732-18-5	Liquid
		Carbon monoxide	CO	28	630-08-0	Gas
		Carbon dioxide	CO ₂	44	124-38-9	Gas
Noble gases	Noble gases	Helium	He	4	7440-59-7	Gas
		Neon	Ne	20	7440-01-09	Gas
		Argon	Ar	40	7440-37-1	Gas
		Krypton	Kr	84	7439-90-9	Gas
		Xenon	Xe	132	7440-63-3	Gas
C-H-bearing molecules	Alkane	Methane	CH ₄	16	74-82-8	Gas
		Ethane	C ₂ H ₆	30	74-84-0	Gas
		Propane	C ₃ H ₈	44	74-98-6	Gas
		Butane	C ₄ H ₁₀	58	106-97-8	Gas
	Alkene	Acetylene	C ₂ H ₂	26	74-86-2	Gas
		Benzene	C ₆ H ₆	78	71-43-2	Liquid
	PAH	Naphthalene	C ₁₀ H ₈	128	91-20-3	Solid
		Phenanthrene	C ₁₄ H ₁₀	178	85-01-8	Solid
		Pyrene	C ₁₆ H ₁₀	202	129-00-0	Solid
C-H-O-bearing molecules	Alcohol	Ethanol trans	C ₂ H ₅ OH	46	64-17-5	Liquid
		Methanol	CH ₃ OH	32	67-56-1	Liquid
	Carboxylic acid	Formic acid	HCOOH	46	64-18-6	Liquid
		Acetic acid	CH ₃ COOH	60	64-19-7	Liquid
		Glycolic acid	HOCH ₂ COOH	76	79-14-1	Solid
	Aldehyde	Formaldehyde	H ₂ CO	30	50-00-0	Gas
		Acetaldehyde	CH ₃ CHO	44	75-07-0	Liquid
C-H-N-bearing molecules	N-heterocycle	Hexamethylenetetramine	C ₆ H ₁₂ N ₄	140	100-97-0	Solid
		Triazine	C ₃ H ₃ N ₃	81	290-87-9	Solid
		Ammonia solution	NH ₄ OH	35	1336-21-6	Liquid
C-H-O-N-bearing molecules		Urea	NH ₂ CONH ₂	60	57-13-6	Solid
	Amide	Formamide	NH ₂ CHO	45	75-12-7	Liquid
	Amino acid	Glycine	NH ₂ CH ₂ COOH	75	56-40-6	Solid

4.1 CASYMIR

The calibration measurements were done in the CALibration SYstem for the Mass spectrometer Instrument ROSINA (CASYMIR) in the Physics Institute of the University of Bern (Westermann et al., 2001; Graf et al., 2004). Figure 4.2 shows a schematic and a picture of RTOF in CASYMIR. This facility is a multi staged vacuum chamber system designed with the goal of simulating the neutral gas coma around a cometary nucleus, for the testing and the calibration of space instruments. CASYMIR can be operated in static mode, either with residual gas only or with a specific gas mixture, or in dynamic mode, where neutral gas beams can be focused onto the instrument source with different gas velocities and impact angles. Particle densities range between 10^{13} and 10^{17} m^{-3} , and molecular beam velocities range between 300 to 3'000 $\text{m} \cdot \text{s}^{-1}$.

Mixtures of gaseous compounds can be produced in a Gas Mixing Unit (GMU) fed by five different gas lines controlled by a series of valves and mass flow controllers. In static mode, the GMU is filled with a gaseous compound, which is introduced in the main chamber (V1) through a thermally regulated leak valve. The regulation keeps the inlet pressure stable and is based on the pressure sensor located closest to the inlet system. Eight other pressure sensors ensure the monitoring of the pressure between the leak valve and RTOF. An inlet system has been added specifically for this calibration campaign to study also liquid and solid compounds; it consists of a glass tube installed near the leak valve LV4 which can be easily pumped, homogeneously heated, and exchanged with tubes containing other compounds.

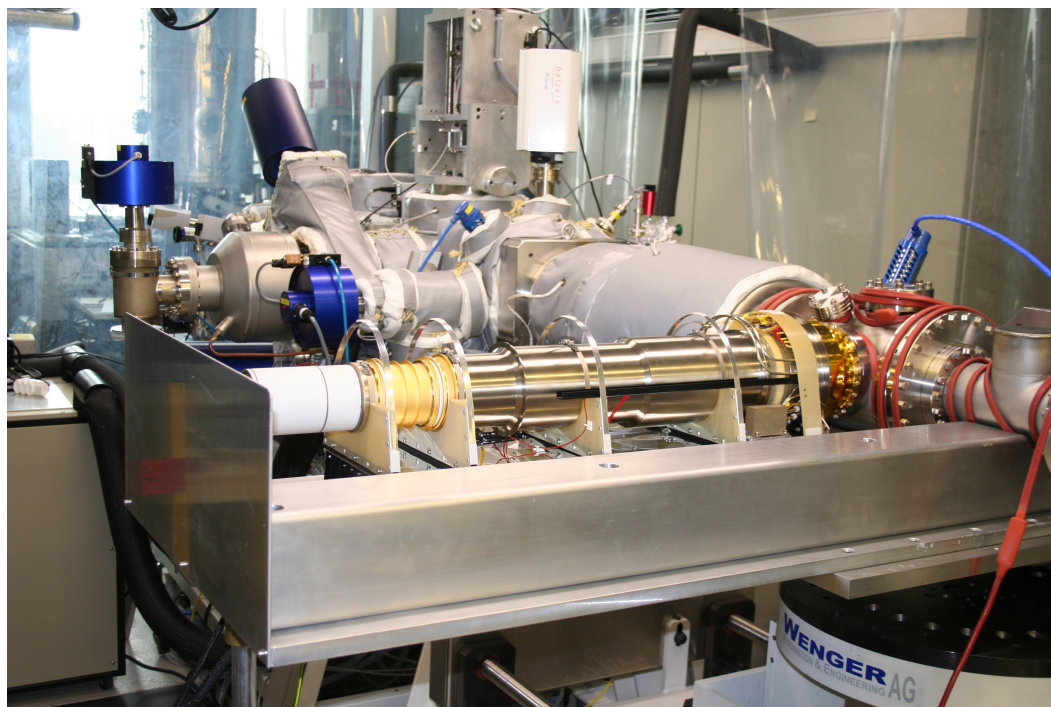


Figure 4.1: Picture of RTOF (front), connected to CASYMIR (back). The RTOF source entrances are aligned with the docking section V0 on the right side of the schematic. The sample tube used for the calibration of liquid and solid compounds was installed near the leak valve LV4, visible at the bottom of the pipe covered with a black insulator, on top of the picture.

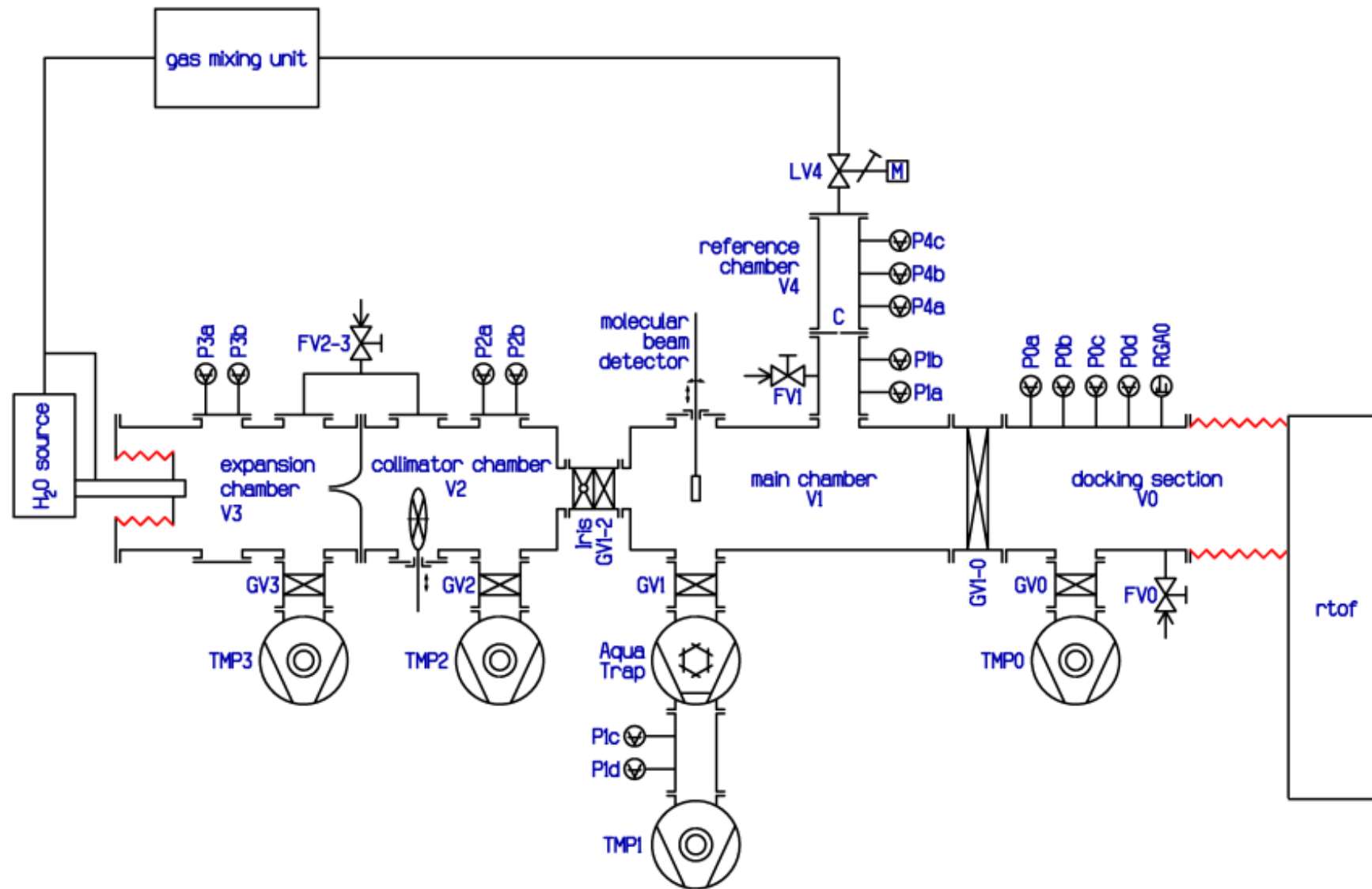


Figure 4.2: Schematics of the CALibration SYstem for the Mass spectrometer Instrument ROSINA (CASYSMIR).

4.2 Measurement protocol

Measurements were done for both channels (SS and OS in neutral mode), for the three possible extraction frequencies and for the three possible filament emissions. A summary of the calibrated modes is shown in table 4.2.

All spectra were acquired at three different pressure ranges, ideally $1 \cdot 10^{-9}$ mbar, $1 \cdot 10^{-8}$ mbar, and $1 \cdot 10^{-7}$ mbar. These pressure references were measured with a Granville-Phillips Ion Gauge, with a typical error of 4% to 6% (Granville-Phillips, 2007). These pressures could be reached only while pumping: the environment can therefore not be considered as absolutely static. A calibration in an absolute static environment would have required making the measurements without pumping and with no gas inlet, which was not feasible without sacrificing the pressure stability.

The protocol below was followed for each compound and for each source:

1. RTOF was switched ON and left to run for 1.5 h before the first calibration measurement in order to reach thermal equilibrium in the sensor and its electronics.
2. Background measurements of the residual gases in the chamber were acquired for each of the operation modes described in table 4.2.
3. Each of the operation modes was acquired three times while the gas inlet was open and the pressure was regulated by a thermal valve. This step was performed for the three pressure ranges mentioned above.
4. Background measurements of the residual gases in the chamber were once more acquired after a waiting time of 30 minutes for each of the operation modes.

In addition, some liquid or solid compounds had to be heated to be measured in their gaseous state. This heating was done using an infrared lamp located close to the inlet tube. Aluminium foil was placed behind the tube to achieve more homogeneous and faster heating, and the temperature was monitored using a PT100 resistance thermometer.

4.3 Data processing

The analysis of the data requires the following steps for each spectrum:

- Correction of the ADC pattern according to section 2.1.7.
- Application of the mass scale according to section 2.2.2; for all the measurements, the mass scale was applied with the peaks from the analysed species, rather than with GCU spectra which would have contaminated the chamber and required an additional waiting time for pumping.
- Integration of all the peaks according to section 2.2.1, for *event* data (SS & OS) as well as for *histogram* data (SS).

For each mode, the calculations of the fragmentation ratios, sensitivities, and their errors are detailed hereafter.

Table 4.2: Calibration measurement protocol for each compound. With a 11 h total duration, a full day was needed for each species.

*As mode 528 has a mass range of [50 – 1/150], it has not been acquired for species with fragments lighter than 50 u/e.

Source	Measurement	Mode	N° of spectra acquired	Duration
Storage Source	Waiting time – thermally stability			1 h 30 min
	Background 1	511	×1	35 min
		516	×1	
		521	×1	
		526	×1	
		528*	×1	
		501	×1	
	506	×1		
	Waiting time – stable inlet pressure			15 min
	Gas inlet measurement for each pressure range	511	×3	1 h 20 min
		516	×3	
		521	×3	
526		×3		
528*		×3		
501		×3		
506	×3			
511	×3			
Waiting time – stable background pressure			30 min	
Background 2	511	×1	35 min	
	516	×1		
	521	×1		
	526	×1		
	528*	×1		
	501	×1		
506	×1			
Orthogonal Source	Waiting time – thermal stability			30 min
	Background 1	513	×1	9 min
		543	×1	
	Waiting time – stable inlet pressure			15 min
	Gas inlet	513	×3	22 min
		543	×3	
	Waiting time – stable background pressure			30 min
Background 2	513	×1	9 min	
	543	×1		
Total per compound			≈ 11 h	

4.3.1 Isotopic and fragmentation ratios

Fragmentation ratios can be expressed in two ways. An **absolute ratio** is obtained by dividing the number of ions of a daughter by the sum of all the ions attributed to the calibrated species. A **relative ratio** is obtained by dividing the number of ions of a daughter by the number of ions of the most abundant fragment, being usually but not always the parent. In the latter case, the most abundant fragment has a relative intensity of 100%.

In this chapter, relative ratio ($I_{\text{daughter}}/I_{\text{parent}}$) will be given, as we are interested in the daughter fragments only to get back to the initial density of the parent molecule. The same applies for the isotopic ratios, given relative to the most abundant isotope.

The determination of the relative ratios depends on the global intensities of the peaks in the spectra: if too high, the saturation effect mentioned in 2.1.7 will generate an underestimation of the highest peaks (usually the parent molecule), thus leading to biased results.

This saturation is particularly visible for the data acquired with a drift voltage of $-3'000$ V, and a correction will be applied and detailed in section 4.4.1. For the data acquired with $D = -1'800$ V, no saturation could be observed.

Without a saturation effect, there is a linear correlation between the gas inlet pressure and the number of ions associated to the studied gas. The calculation of the ratios will therefore be done using the ratio of the slopes a_i of the equation curves:

$$I_i = a_i p + \text{offset} \quad (4.1)$$

with I_i the number of counts in the peaks corresponding to the studied gas, and p the pressure measured in the vacuum chamber.

Figure 4.3 shows an example of this method, using water measurements of the FM OS at 100 μA filament emission and 10 kHz extraction rate (mode 513) with a drift voltage of $-1'800$ V. The ratio of the slopes gives directly $\text{OH}/\text{H}_2\text{O} = 20.59$ %. The error on the ratios is given by the statistical error on the numerical integration and the error on the fit.

It is expected to observe variations of the fragmentation patterns due to the ion source settings, especially the ion source backplane and the extraction grid, and it may also vary with the emission of the filament. It is on the other hand not expected to observe any difference of fragmentation due to the extraction frequency, nor due to the settings other than of the ion source (as drift, acceleration and reflectron voltages).

Thereafter, a comparison will often be done with the National Institute of Standards and Technology (NIST) database (Stein): differences are expected due to the fact that the NIST spectra are acquired by a quadrupole and not a TOF/MS, but a comparison is still justified as the ionization is performed with electron impact at an ionization energy of 70 eV, which is close to the ionization energy of RTOF.

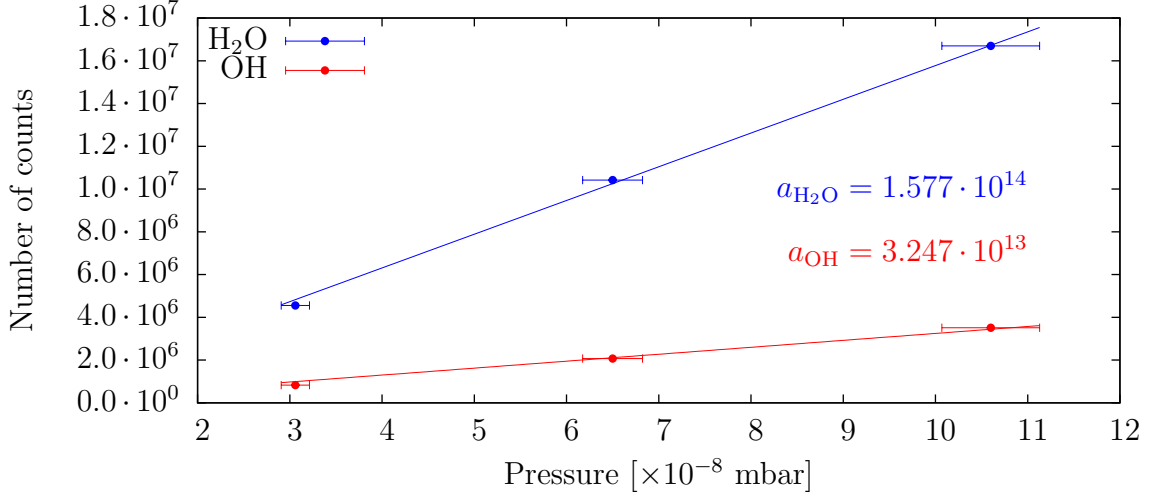


Figure 4.3: Correlation between pressure and number of ions for the parent (H_2O) and a fragment (OH). A linear interpolation gives a slope of $1.577 \cdot 10^{14}$ counts/mbar for H_2O and $3.247 \cdot 10^{13}$ counts/mbar for OH , leading to the ratio $\text{OH}/\text{H}_2\text{O} = 20.59\%$.

4.3.2 Sensitivity

The sensitivity of a mass spectrometer links the ion current to the partial pressure of the sample in the ion source. It depends on the instrument characteristics as well as on the gas composition, due to the different ionization cross sections of the different chemical species.

Sensitivities S_i are derived from the ratio (measured ion current) / (density of the sample):

$$S_i = \frac{I_i}{I_{em}n_i} \quad (4.2)$$

where I_i is the total current generated by the measured ions (including the parent molecule, the daughters, the doubly charged ions and the isotopologues), I_{em} the filament emission, and n_i the density. n_i is derived from the partial pressure p_i using the ideal gas law $p_iV = N_ik_B T$ at a temperature T of 293 K, with N_i the number of particles and k_B the Boltzmann constant:

$$n_i = \frac{N_i}{V} = \frac{p_i}{k_B T} \quad (4.3)$$

The ratio I_i/n_i is obtained by calculating the slope given by the measurements of the signal for three different pressures. An example is given below, once again using water measurements of the FM OS at 100 μA filament emission and 10 kHz extraction rate (mode 513) with a drift voltage of $-1'800$ V.

The slope in figure 4.4 gives $I_i/n_i = 6.251 \cdot 10^{-26}$ A.cm³, thus leading to a sensitivity of:

$$S_i = \frac{I_i}{I_{em}n_i} = \frac{6.251 \cdot 10^{-26} \text{ A.cm}^3}{100 \cdot 10^{-6} \text{ A}} = 6.251 \cdot 10^{-22} \text{ cm}^3$$

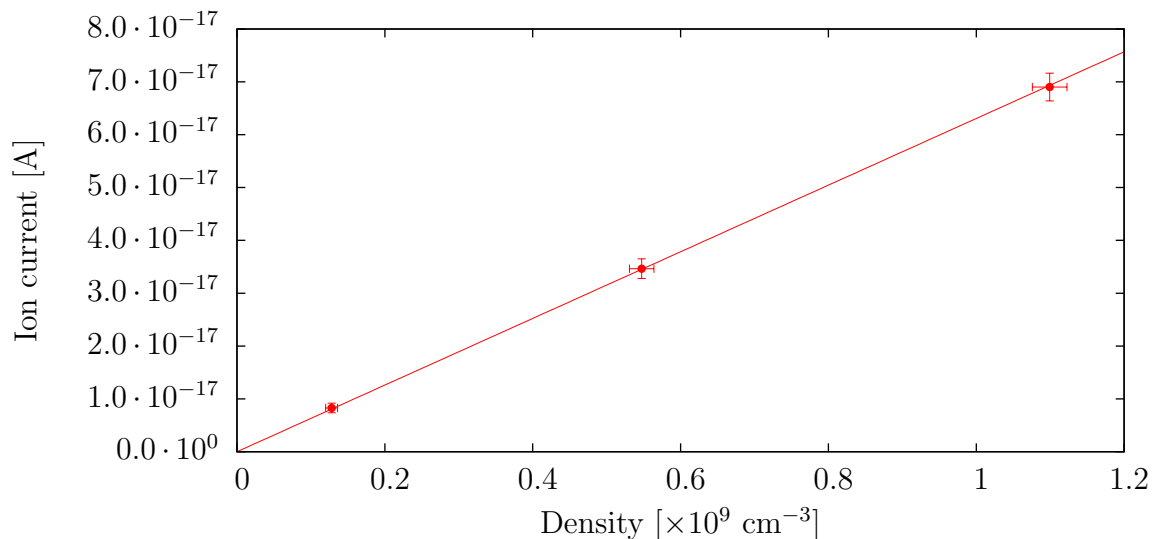


Figure 4.4: Example of calibration curve for the calculation of the sensitivity. The ion counts have been integrated as described in section 2.2.1, and multiplied by q to get the induced current. Density is calculated according to equation 4.3 with a 5% error due to the Granville-Phillips accuracy.

As above, sensitivities will be expressed in cm^3 in this chapter, although $\text{A}\cdot\text{mbar}^{-1}$ is a more common unit: the main reason is to stay consistent with the DFMS values given by Hässig (2013), but it will also ease the density calculations in chapter 5.

The statistical error for the sensitivity measurement will be in most of the cases of the order of 1%. Additional uncertainties due to pressure measurements (5%) and detector will be added in the presented results.

4.4 Summary – $D = -3'000$ V

The results of this section are based on the measurements of Sinzig (2003), acquired before launch for the calibration of the orthogonal sources of both the FM and FS models. Measurements were done with CO_2 and krypton at several inlet pressures ($5 \cdot 10^{-9}$, $1 \cdot 10^{-8}$, $1 \cdot 10^{-7}$, and $1 \cdot 10^{-6}$ mbar), with a medium filament emission for the FS (mode 513), and with the three filament emissions for the FM (modes 503, 513, and 523).

Fragmentation ratios as well as sensitivities have been recalculated to avoid differences due to data processing. The results for CO_2 and krypton will be presented in the two following sections, and the obtained values will be confirmed in a third section with GCU measurements performed with the FM (Sinzig, 2003).

4.4.1 CO_2 fragmentation

RTOF can be operated at pressures lower than 10^{-6} mbar, but for the highest pressures and with optimized settings for $D = -3'000$ V, the saturation effect detailed in 2.1.7 appears. This effect is clearly visible in the CO_2 data acquired with the FM, as shown in figure 4.5.

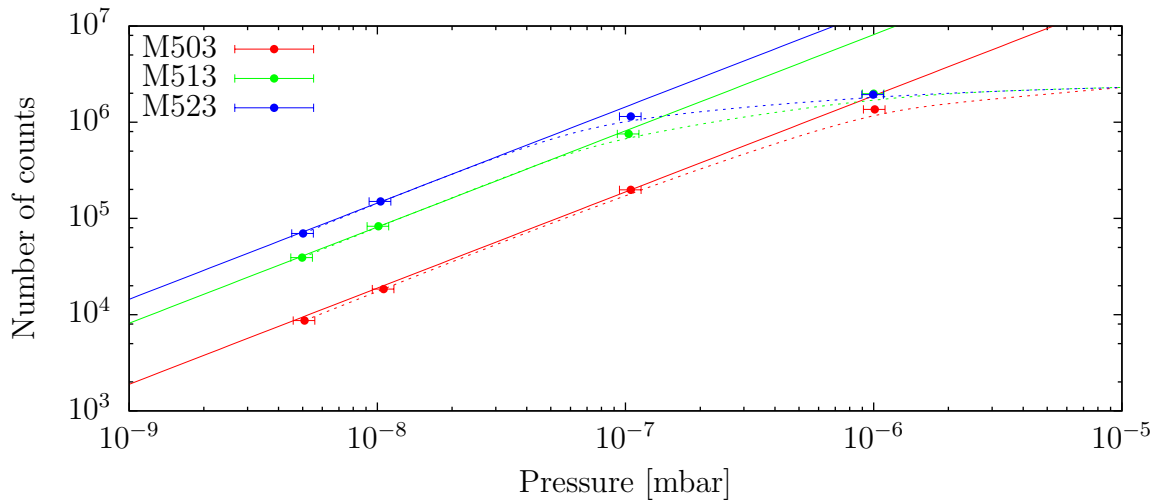


Figure 4.5: Saturation effect for relatively high pressure measurements. A decrease of the CO_2 signal starts to be visible for peaks with a number of counts of 10^6 , corresponding to a gas inlet pressure of 10^{-6} mbar for mode 503 but already 10^{-7} mbar for mode 523.

This effect needs to be compensated for the calculation of the fragmentation ratios, either using only the measurements with the lower pressures, or extrapolating linearly the intensity of the highest peaks. The latter solution will be implemented here for the FM – no saturation was observed for the FS. Without this correction, all the fragments would be overestimated, due to the underestimation of the parent (CO_2).

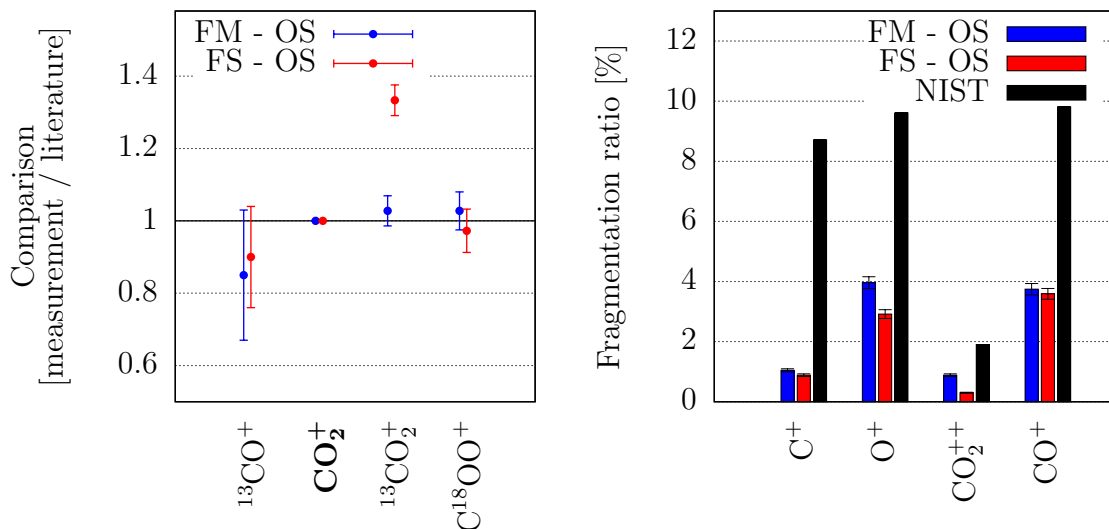


Figure 4.6: Isotopologic and fragmentation ratios for CO_2 . On the left side, the points correspond to the isotopologic ratios measured with RTOF divided by the ones from literature (NIST). On the right side, fragmentation ratios are given relative to CO_2^+ . When not specified, C = ^{12}C and O = ^{16}O .

Figure 4.6 and table B.1 summarize the fragmentation ratios obtained with spectra acquired by Sinzig (2003) at different CO_2 inlet pressures, compared with the literature values (NIST).

If the isotopic ratios for C^{18}OO^+ and $^{13}\text{CO}^+$ are similar to the literature, the RTOF FM and FS generate significantly less fragments than the quadrupole used for the NIST measurements. By the same token, the doubly charged ions are much less abundant for the FS than for the FM or NIST. A possible explanation lies in the difference in the electron energy between the FM and the FS: the electrons are emitted at a potential of -70 V, and their energy depends on the potential of the ionization region, located between the ion source backplane and the extraction grid; as the ion source backplane is being given a voltage of -13.5 V for the FS and $+5.0$ V for the FM, the electron energy is therefore higher for the FM than for the FS, leading logically to a higher fragmentation for the FM.

The FS ratio $^{13}\text{CO}_2^+/\text{CO}_2^+$ is 33% higher than NIST and can not be explained by contamination from another compound in the vacuum chamber: the best candidate for an overabundance at mass 45 would be formamid (CH_3NO) from previous measurements in CASYMIR, but no increase due to the most abundant fragment of formamid is observable at mass 29 (formyl radical – CHO). Particular attention will be drawn to this ratio for the space data as well as for the other configurations (i.e. $D = -1'800$ V and $D = -1'000$ V).

These first observations already confirm the need for an instrument-specific calibration.

4.4.2 Krypton isotopic ratios

Figure 4.7 and table B.2 summarize the isotopic ratios obtained with spectra acquired by Sinzig (2003) at different krypton inlet pressures, compared with the literature (NIST).

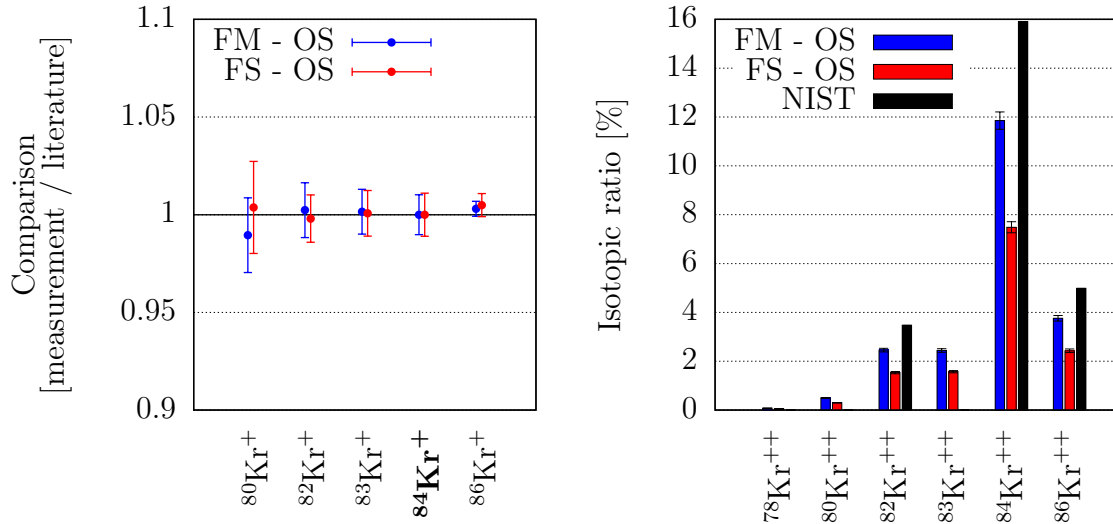


Figure 4.7: Isotopic ratios for Kr. On the left side, the points correspond to the isotopic ratios measured with RTOF divided by the ones from literature (NIST). On the right side, isotopic ratios for the doubly charged ions are given relative to $^{84}\text{Kr}^{++}$.

The isotopic ratios for the singly charged krypton isotopes are similar to the literature within a 3% margin.

The doubly charged ions are less abundant for the FM and the FS than for NIST, but are consistent for each RTOF model: the doubly charged ions have the same ratios relative to $^{84}\text{Kr}^{++}$ as the single charged ions relative to $^{84}\text{Kr}^+$, with a ratio doubly charged / single charged of 7% for the FS, 11% for the FM, and 16% for NIST.

4.4.3 Sensitivities

The sensitivities for CO_2 and Kr, calculated as explained in 4.3.2, are presented in table C.2. As a mathematical exercise, the datapoints have been fitted with a square root function (see figure 4.8). This empirical correlation will be used later to extrapolate sensitivities for helium for the three filament emissions.

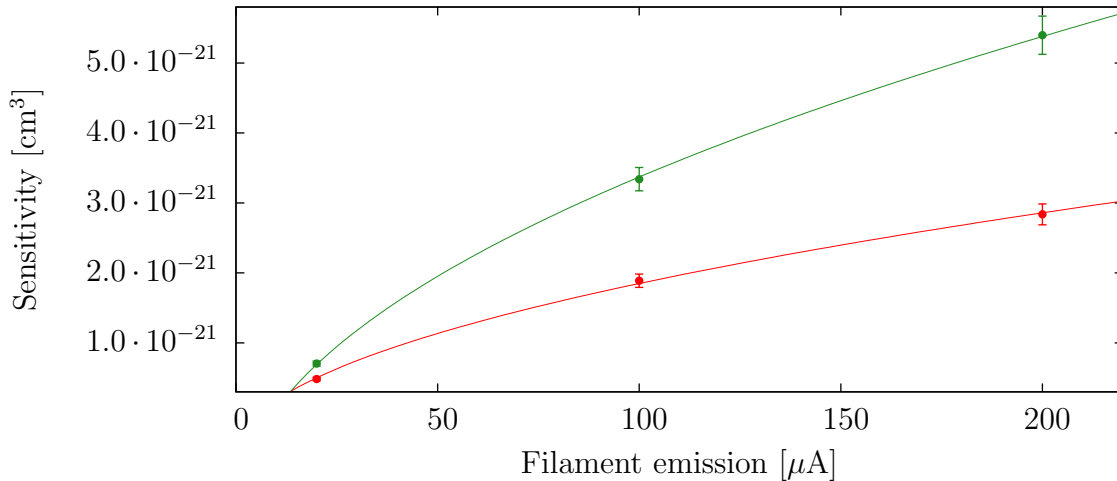


Figure 4.8: Correlation between sensitivity and filament emission for CO₂ and krypton (RTOF - FM). Data points have been fitted with curves of equation $y = a\sqrt{x} + b$.

4.4.4 GCU

The results obtained above will be applied on a GCU spectrum acquired in May 2003 with the RTOF FM, for the mode 523, and with the same settings as the CO₂ and krypton measurements. The spectrum is fitted with a sum of pseudo-Voigt profiles, using as variable only the intensity of the main species – here the GCU gases He, CO₂, and Kr. The intensities of the fragments are defined by the fragmentation ratios established previously.

The spectrum and the model are drawn in figure 4.9; a specific color is attributed to each species, but only one model is applied. This method will be used for the analysis of space data, where the initial composition of the cometary gas is unknown.

The sensitivity for helium is estimated using the following hypothesis:

- the sensitivity follows the square root of the emission (see figure 4.8),
- the three GCU gases He, CO₂, and Kr, are injected simultaneously in the ion source in the same quantities – one third each.

With these hypotheses, the sensitivity for helium and for the FM OS in mode 523 has been estimated to be $6.98 \cdot 10^{-23} \text{ cm}^3$, and the values for modes 503 and 513 have been extrapolated so that they would be proportional to the square root of the emission (see table 4.3).

Even with estimated sensitivities for helium, the calculated densities for CO₂ and krypton give very similar proportions for the GCU composition. This first exercise demonstrates the initial capabilities of RTOF and illustrates how the partial densities will be calculated out of measurement of a gas mixture in chapter 5.

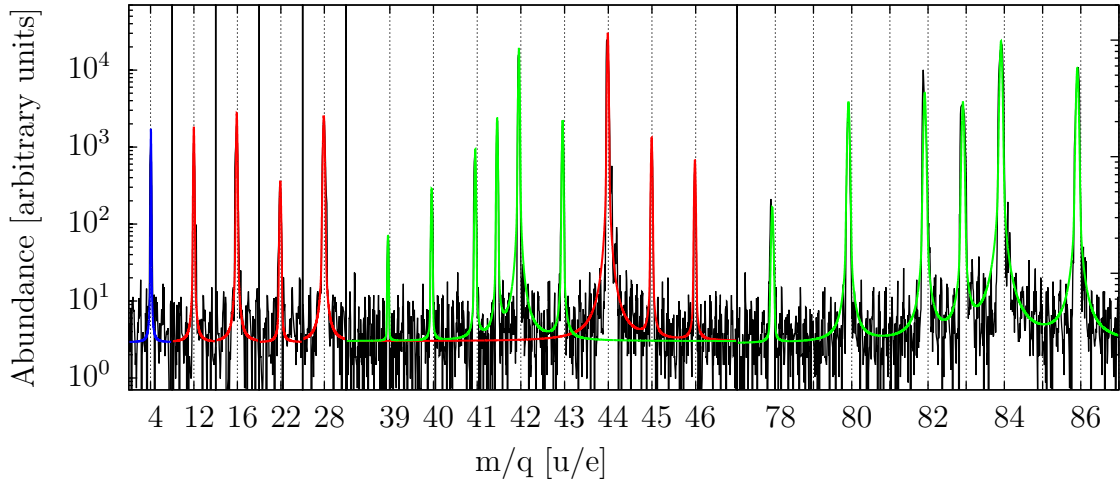


Figure 4.9: Fragmentation model of a GCU spectrum. The model has been created using only the intensities of the main species as input, i.e. He (blue), CO₂ (red), and Kr (green).

Table 4.3: GCU gases abundances for the three main FM OS neutral modes. Sensitivities for helium have been estimated (*). Errors for the final ratios are of the order of 5%.

		M503	M513	M523
Sensitivity [cm ³]	He	*1.19 · 10 ⁻²³	*4.64 · 10 ⁻²³	*6.98 · 10 ⁻²³
	CO ₂	4.84 · 10 ⁻²²	1.89 · 10 ⁻²¹	2.84 · 10 ⁻²¹
	Kr	7.04 · 10 ⁻²²	3.34 · 10 ⁻²¹	5.40 · 10 ⁻²¹
Density [cm ⁻³]	He	1.26 · 10 ¹²	4.05 · 10 ¹¹	3.72 · 10 ¹¹
	CO ₂	1.16 · 10 ¹²	4.30 · 10 ¹¹	3.76 · 10 ¹¹
	Kr	1.24 · 10 ¹²	4.02 · 10 ¹¹	3.69 · 10 ¹¹
Proportions	He	34.43 %	32.73 %	33.32 %
	CO ₂	31.66 %	34.77 %	33.62 %
	Kr	33.91 %	32.51 %	33.06 %

4.5 Results – $D = -1'800$ V

The solution found to handle the problem with the 9 kV high voltage converter implies a decrease of the maximum available voltage which led to the finding of optimized settings for the FM with a drift value of $-1'800$ V. As part of the optimization process, the ion source settings have been changed compared to the ones used with $D = -3'000$ V (section 4.4) and the fragmentation needed to be characterized again. This is the purpose of the second calibration campaign, done with the FM, and detailed in this section.

4.5.1 General remarks

The presentation of the results will not be done chronologically, as the order of measurement was chosen depending on possible interferences: after calibrating one compound, and depending on the species, several hours were needed to pump the residual gases. In the case of the noble gases, only half an hour was needed to get rid of the remaining gas in the chamber and in the tube sample; for other products such as naphthalene, traces could be observed weeks after the calibration campaign, even after heating the chamber. This was expected and the polycyclic aromatic hydrocarbons measurements were done almost at the end of the calibration period.

Particular care was therefore taken to avoid the calibration of species which would have fragments located at the same masses, or which would have masses close to each other. For instance, CO was calibrated before – and not adjacent to – CO_2 , to avoid having an overabundance of CO around mass 28, among others. However, the amount of remaining gas after a measurement is supposed to be small and constant, and the calibration procedure was designed to handle the presence of residual gases in the chamber or in the sample tube, with background measurements performed before and after the sample measurements.

Other factors such as the availability of the compounds or the easiness to pump also played a role in the preparation of the order of the measurements.

Unlike the results obtained with a drift voltage of $-3'000$ V, no saturation effect was observed in the spectra acquired with $D = -1'800$ V. This is mainly due to the fact that pressures lower than $1.0 \cdot 10^{-7}$ mbar were set, but also to the fact that the signal is weaker due to a lower sensitivity, thus the probability of having more than one ion hitting the detector within less than 1.65 ns (1 bin) is much smaller.

With no saturation effect, the analysis of both the event and histogram data for the SS gives similar results in term of fragmentation and isotopic ratios (within the error bars); put differently, the ratio histogram / event remains constant for each spectrum. Hence, the storage source results will be presented together as “SS” data; “OS” data are based on the events only.

Finally, for species other than H_2O , CO, CO_2 , and the noble gases, as more than 50 fragments are generated for some compounds, only the fragments with a relative abundance higher than 5% will be displayed for clarity reasons. The complete lists of fragments are listed in the fragmentation tables in appendix B.

4.5.2 Noble gases

Noble gases do not undergo chemical reactions and are highly volatile – their volatility decreases with mass. Therefore, any change in their elemental and isotopic compositions is caused by thermal processes, providing us information about the physical conditions in the early Solar System. Remote observations of the noble gases are difficult because their resonance transitions lie in the far-UV spectral region (Bockelée-Morvan et al., 2004); before *Rosetta*, no noble gas had been identified in comets.

The noble gases helium, neon, argon, krypton, and xenon have been studied to characterise the accuracy of RTOF regarding isotopic ratios. These gases were actually calibrated first, because they are easy to measure due to their gaseous state and their low chemical reactivity. The results are summarized in table B.3 page 87 and in figure 4.11 page 57. A few preliminary comments:

- ^3He is the second most abundant isotope of helium with a relative abundance of $1.34 \cdot 10^{-6}$ compared to ^4He , and ^3He is not detectable with RTOF, and no isotopic ratio for helium will be provided here.
- Using the same reasoning as for $D = -3'000$ V, and based on the ion source backplane voltages being negative for the OS and more negative for the SS, it is expected to have less doubly charged ions for RTOF than in the literature, and less doubly charged ions for the SS than for the OS.

Neon

The analysis of the neon spectra resulted in the observation of the three stable isotopes of neon (^{20}Ne , ^{21}Ne , and ^{22}Ne), but no doubly charged ions could be detected. The error bars are larger for $^{21}\text{Ne}^+$ due to the lower abundance of this isotope.

Argon

The three stable isotopes of argon are observable in the calibration data, and for the most abundant of them, ^{40}Ar , a peak at half the mass of $^{40}\text{Ar}^+$ is observed and corresponds to the doubly charged ion $^{40}\text{Ar}^{++}$.

The deviation of the ratios for $^{40}\text{Ar}^{++}$ illustrates the fact that the SS creates much less doubly charged ions than the OS, and generally RTOF creates less doubly charged ions than NIST. The creation of doubly charged ions for argon compared to NIST is $(45.0 \pm 0.5)\%$ for the OS and $(7.7 \pm 0.2)\%$ for the SS.

Krypton

As for the previous noble gases, all the stable isotopes of krypton are visible in the spectra, and doubly charged ions are present for all except $^{78}\text{Kr}^{++}$. Its abundance was too low to be detected, but upper limits of 0.07% for the OS and 0.03% for the SS can be extrapolated, based on the abundance of $^{78}\text{Kr}^+$ and on the average of the doubly charged ions / singly charged ions ratio for krypton. The creation of doubly charged

ions for krypton compared to NIST is $(58.82 \pm 0.84)\%$ for the OS and $(29.44 \pm 1.15)\%$ for the SS.

Xenon

The xenon data are consistent with the previous measurements and most of the stable isotopes are detected in the same proportions as for the literature. ^{124}Xe and ^{126}Xe show very large error bars: their theoretical abundances are of the order of 0.35% of the most abundant isotope, ^{132}Xe , representing only 30 counts per peak or 5 counts per bin in the best case (center of the peak, high pressure, high extraction rate, and high emission), which is the average noise level. With “only” three spectra acquired per setting, the statistics are not good enough to reduce these errors. The creation of doubly charged ions for xenon compared to NIST is $(69.63 \pm 1.89)\%$ for the OS and $(46.90 \pm 5.55)\%$ for the SS.

Fragmentation summary

For all the studied noble gases, the RTOF SS and OS are able to provide isotopic ratios within 200 s using different extraction frequencies and different emissions with typical error bars in the range of the percent. The main difference between the two sources is the abundance of doubly charged ions, explained by the difference of potential in the sources (due to different BP and GR values essentially).

The amount of doubly charged ions compared to the singly charged ions is correlated with the mass (see figure 4.10). Doubly charged ions are in any case good witnesses of the presence of singly charged ions, the latter being found at twice the mass of the former.

The values of the fragmentation ratios are summarized in table B.3.

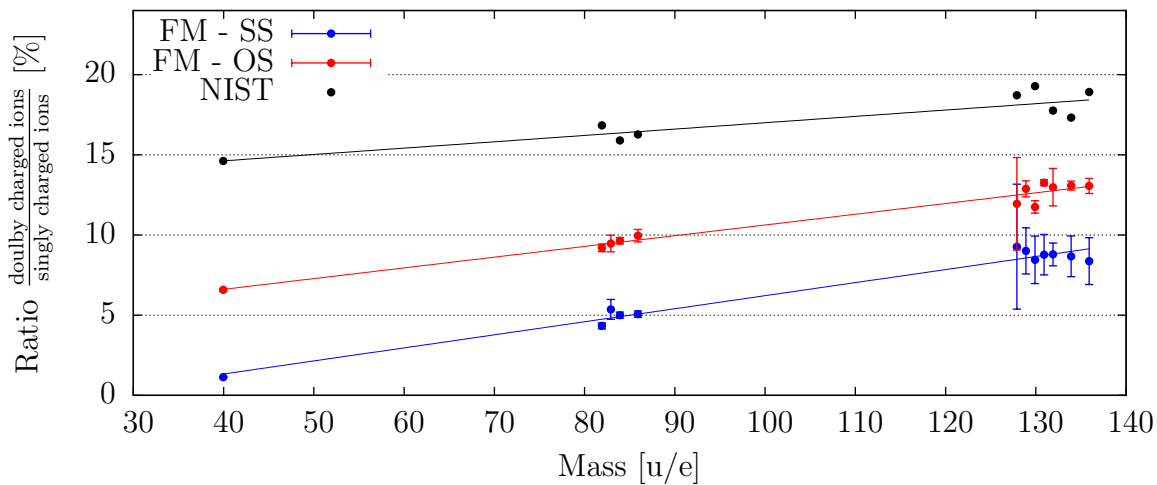


Figure 4.10: Correlation between mass and doubly/singly charged ions ratio.

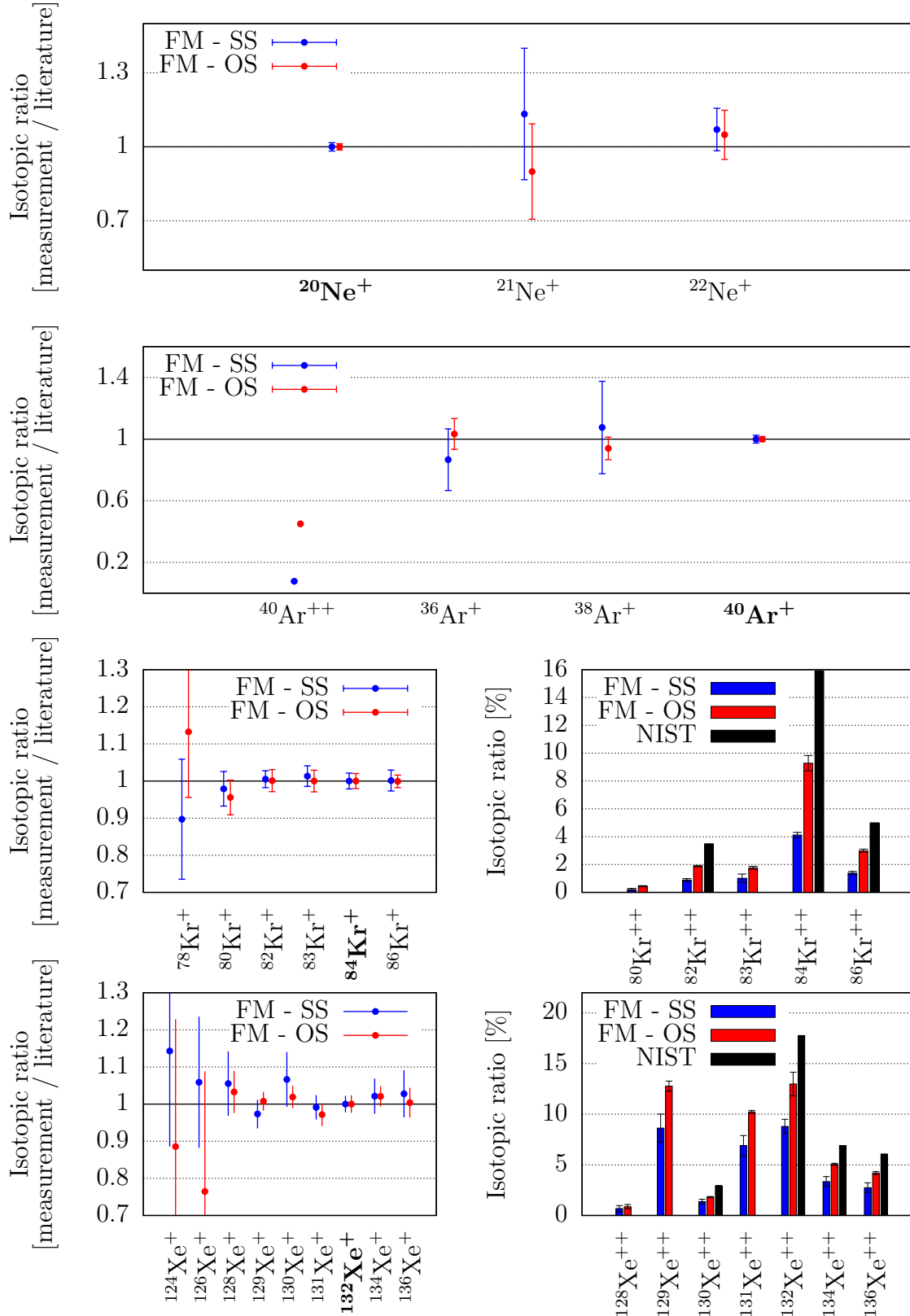


Figure 4.11: Isotopic ratios for Ne, Ar, Kr, and Xe. For Kr and Xe, singly charged isotopes are shown on the left panel and are relative to the literature (NIST), doubly charged ions are shown on the right panel and are relative to the main isotope ($^{84}\text{Kr}^+$ for krypton and $^{132}\text{Xe}^+$ for xenon). No literature data is available for $^{83}\text{Kr}^{++}$, $^{131}\text{Xe}^{++}$, and $^{129}\text{Xe}^{++}$, as NIST provides data for integer masses only.

4.5.3 H₂O, CO, CO₂

H₂O is the most abundant constituent of cometary ices and is one of the most important elements required for life as we know it; the large amount of water on Earth surely participated in the development of living species on our planet. Nonetheless, the origin of terrestrial water is still under debate nowadays: based on the water content of meteorites, which strongly depends on their heliocentric distance, it is believed that the planetesimals formed near the Earth had to have a low amount of water because of the high temperature of their accretion. This suggests that water originates from other places in the Solar System (Oró, 1961), brought on Earth for instance by collisions with asteroids or with comets originating from the outer Solar System (Owen and Bar-Nun, 1995).

The *in situ* study of cometary water is of particular importance as spectroscopic measurements are limited by a strong absorption in the terrestrial atmosphere (Mumma and Charnley, 2011). The presence of water in comets was first derived in the 1970s from the observation of clouds of atomic hydrogen and OH radicals around comets (Festou et al., 1993), then interpreted as dissociated fragments of water molecules.

Additionally, water will be almost always seen in the spectra produced by RTOF on the ground and in flight, and is therefore a reliable peak for the determination or the checking of the mass scale.

The fragmentation ratios of H₂O are summarized in table B.4 and shown in figure 4.12. The isotopologic ratios from literature are lying within the error bars of the calibrated values.

The analysis of the fragments is more surprising: with the same reasoning as for $D = -3'000$ V, and based on the fact that $BP_{SS} < BP_{OS} < 0.0$ V, it is expected to have less fragments for RTOF than in the literature (NIST), and less fragments for the SS than for the OS. This was the case for the doubly charged isotopes of the noble gases from the previous section, but this is not valid for H₂O, which presents slightly higher proportions of fragments compared to NIST; furthermore, the OS has more fragments than the SS.

A preliminary explanation can be found in the nature of the mass spectrometer used by NIST for the establishment of their database: if the sensitivity of a time-of-flight mass spectrometer remains independent of the mass until $m \approx 200$ u/e, a quadrupole mass analyser offers a high sensitivity for masses between ≈ 15 u/e and 80 u/e, and a lower sensitivity otherwise. The higher abundance of fragments with a mass close to 16 u/e (O⁺) and 17 u/e (OH⁺) is consistent with this hypothesis and should be emphasized for lighter and much heavier elements.

CO was first observed by Feldman and Brune (1976) in comet C/1975 V1 (West), and later measured *in situ* in 1P/Halley with the Neutral Mass Spectrometer (NMS) aboard *Giotto* (Eberhardt et al., 1987), with a relative abundance to water of 0.4% to 30%. Its remote observation is also difficult due to the missing permanent electric dipole moments of the symmetric molecules (Mumma and Charnley, 2011), and its characterisation is fundamental for RTOF as the latter cannot resolve CO from N₂.

For CO, the isotopologues are in the same proportion as the literature and the fragmentation of the parent into O⁺ and C⁺ is of the order of 80% for the SS and 12% for the OS compared to NIST (see figure 4.12): the difference may be even greater here as for the H₂O fragments, as lighter masses are involved – 16 for O and 12 for C.

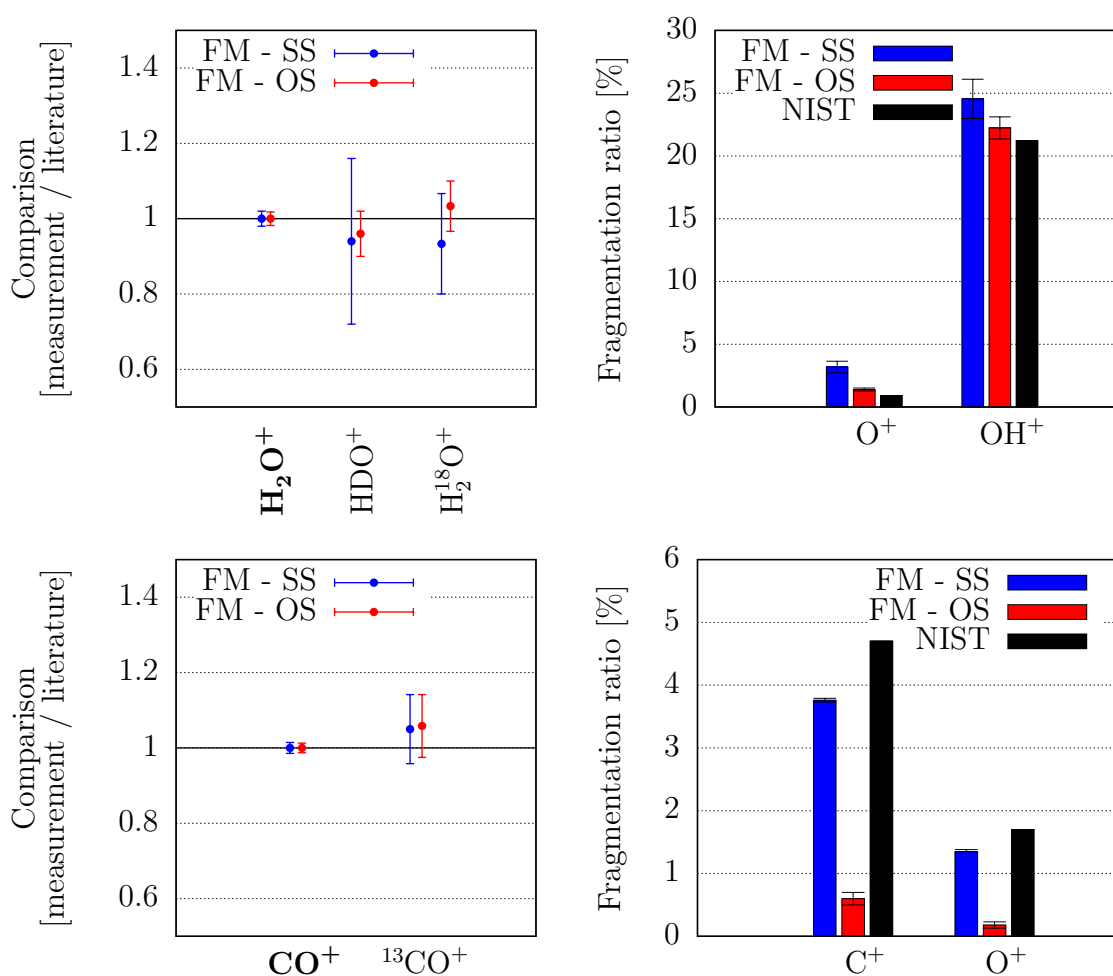


Figure 4.12: Isotopologic and fragmentation ratios for H₂O and CO. On the left side, the points correspond to the isotopologic ratios measured with RTOF divided by the ones from literature (NIST). On the right side, fragmentation ratios are given relative to H₂O⁺ for H₂O, and CO⁺ for CO. When not specified, C = ¹²C and O = ¹⁶O.

CO_2 has been indirectly identified from the observation of CO_2^+ in the optical spectrum of Comet C/1947 S1 (Bester) (Swings and Page, 1950) and in the UV spectrum of Comet C/1975 V1 (West) (Feldman and Brune, 1976).

The remote observation of carbon dioxide undergo the same limitations as H_2O because of the strong absorption from terrestrial CO_2 .

CO_2 is one of the three gases contained in the RTOF GCU and will therefore be used to compare the behaviors of the FS and the FM.

Regarding the calibration measurements (figure 4.13), the high contrast between the very low abundance of the doubly charged ions (CO_2^{++}) on one hand, and the very high abundance of O^+ and C^+ on the other hand, confirm once more the differences in sensitivity between RTOF and the NIST quadrupole.

Nevertheless, the non-linear sensitivity of the quadrupole cannot be invoked for the overabundance of CO^+ compared to literature: at mass 28, the sensitivity of a quadrupole is already “high” and no overabundance of CO would be expected.

A contamination by CO or N_2 is improbable given that CO was measured *after* CO_2 and that N_2 would be revealed by the presence of N^+ around mass 14, which is not the case. The only explanation to date is that RTOF in the $D = -1'800$ V configuration has a high transmission for CO^+ , O^+ , and C^+ , and a very low one for the doubly charged ions. This discussion will be followed up with the next measurements.

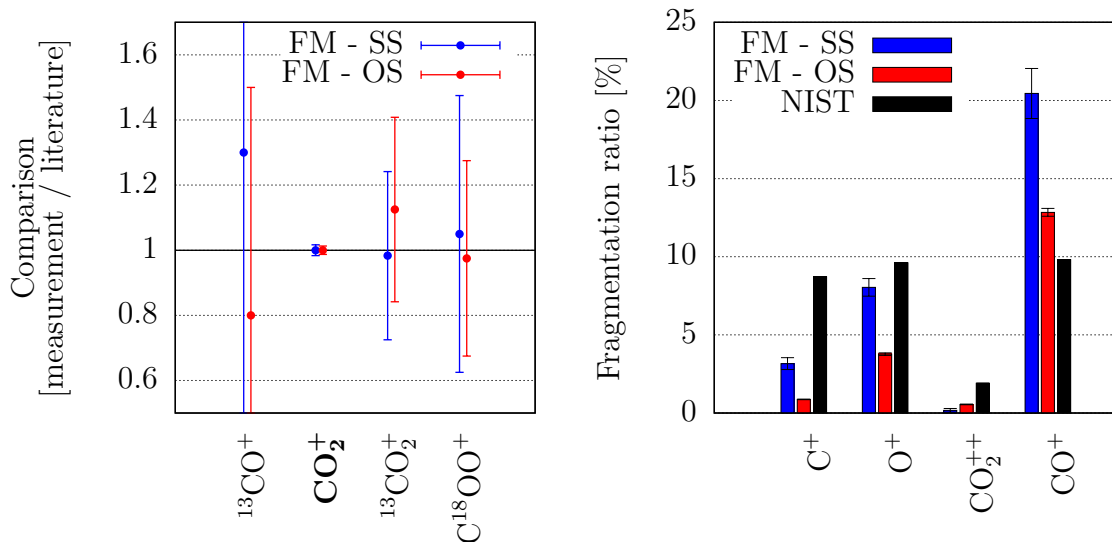


Figure 4.13: Isotopologic and fragmentation ratios for CO_2 . On the left side, the points correspond to the isotopologic ratios measured with RTOF divided by the ones from literature (NIST). On the right side, fragmentation ratios are given relative to CO_2^+ . When not specified, $\text{C} = ^{12}\text{C}$ and $\text{O} = ^{16}\text{O}$.

4.5.4 C-H-bearing compounds

C-H-bearing molecules such as alkanes, alkenes, and polycyclic aromatic hydrocarbons (PAH), are regularly seen in comets, especially CH_4 , C_2H_2 , and C_2H_6 (Mumma et al., 2003): the latter molecules have been detected spectroscopically in comet Hyakutake (Mumma et al., 1996) and in many comets since (Bockelée-Morvan et al., 2004), as well as *in situ* with the *Giotto* NMS measurements of 1P/Halley (Eberhardt, 1999). Alkanes, alkenes and PAH up to C_9H_{12} have also been detected by ROSINA in the gas cloud surrounding the *Rosetta* spacecraft (Schläppi et al., 2010).

Alkanes

Alkanes are saturated hydrocarbons consisting of carbon and hydrogen atoms, bound together with single bonds. In addition to comets, they can be found in the atmospheres of the giant planets of our Solar System and on Saturn's moon Titan (Owen, 2005), and have also been detected in carbonaceous chondrites (Sephton, 2002). They are typical products from living organisms.

Independently of the instrument, the fragmentation of alkanes is much more important for the heavy chains than for the light ones, to such an extent that the parent fragments for ethane, propane, and n-butane are less abundant than some of their fragments. A fraction of the propane molecules, losing a methyl substituent, fragments itself into C_2H_5^+ , which becomes the most abundant species seen. Likewise, C_3H_7^+ and C_2H_4^+ are the most abundant fragments of n-butane, created when n-butane loses one or two methyls respectively.

Another effect, particularly visible in the propane data, is the SS – OS inversion: for low masses, the SS produces globally more fragments than the OS, but for high masses this effect is inverted. As many fragments are created, one could think that this is due to the fact that in the 10 kHz mode, not more than 31 ions can be detected per extraction, leading to an underestimation of the heavy masses. However, the results obtained with the 5 kHz modes are identical, although 64 ions can be measured in this configuration. A possibility for this inversion could be lying in the way the ions are stored in the storage source: if the storage of the heavy ions is less efficient than the one of the light ions, such a difference between the OS and the SS would arise, as the OS do not benefit of any storage. A full characterization of the storage would be needed to confirm or reject this hypothesis.

A more general result regarding the OS, also valid for the other calibrated species, concerns the systematically high abundance at mass 28, i.e. for C_2H_4 . As for the high abundance of CO in the previous section regarding H_2O , CO and CO_2 , a contamination with N_2 or CO during the measurement has to be excluded: first, no suspicious peak is visible in the spectra at mass 14, which would reveal the presence of N_2 in the sample; second, the abundances of C^+ and O^+ are not high enough to explain an overabundance of CO. This effect has to be considered as specific of RTOF.

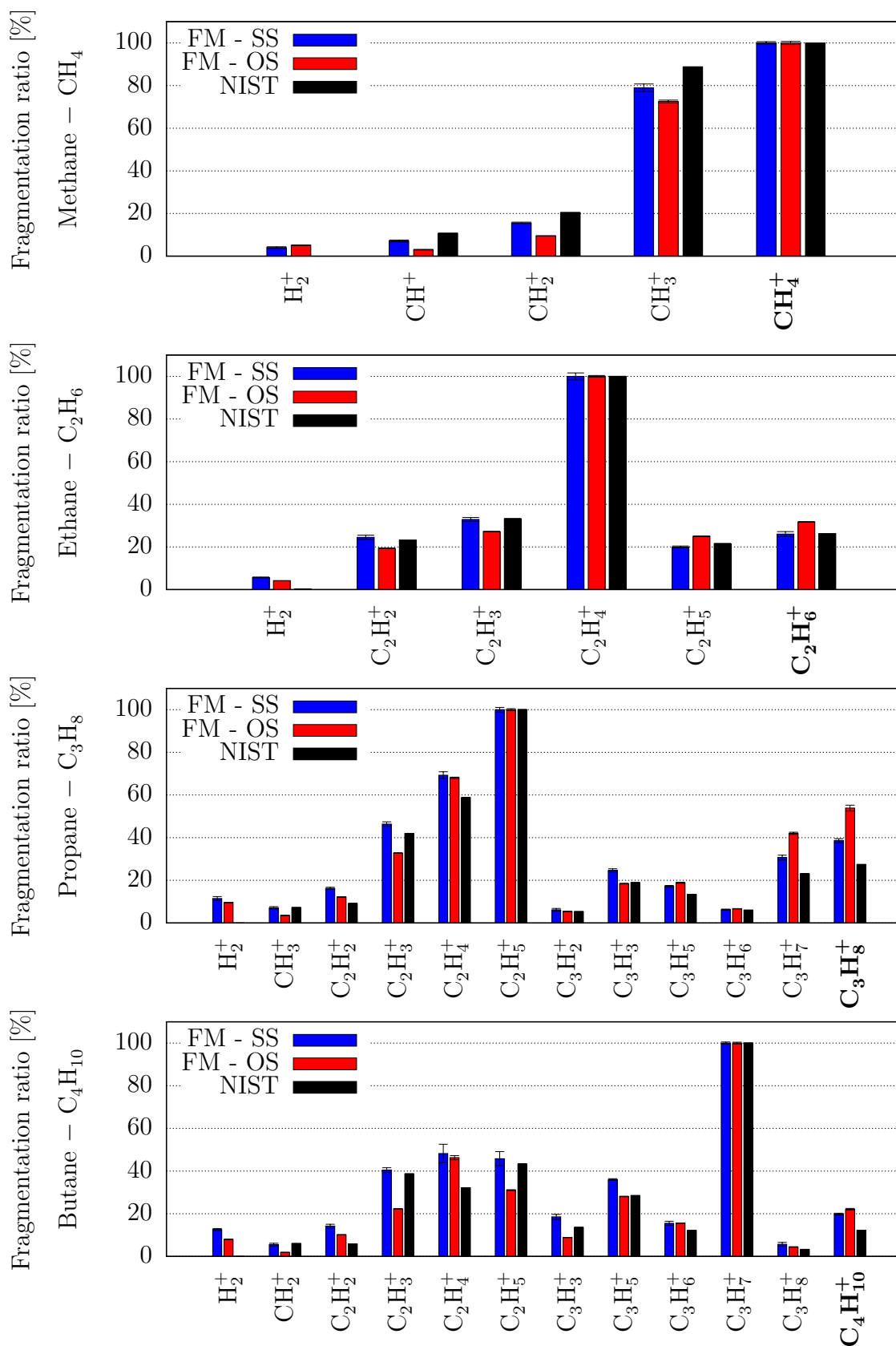


Figure 4.14: Fragmentation ratios – alkanes. Ratios below 5% are not shown, and the labels on the x-axis represent the molecule contributing the most at a given mass.

Alkenes

Alkenes are unsaturated hydrocarbons containing at least one C–C double bond, and participate in many chemical reactions.

Acetylene has few fragments and the relatively low abundance of the daughters reflects the difficulty to break the double bond between the two carbons.

The large error bars on the benzene ratios is to be attributed to the time when the measurement was performed: C_6H_6 was measured last, after all the alcohols, acids and PAH detailed in the next sections. The main contribution for the error comes from the remaining phenanthrene, being very abundant during the days following its calibration, and having a lot of fragments in common with benzene.

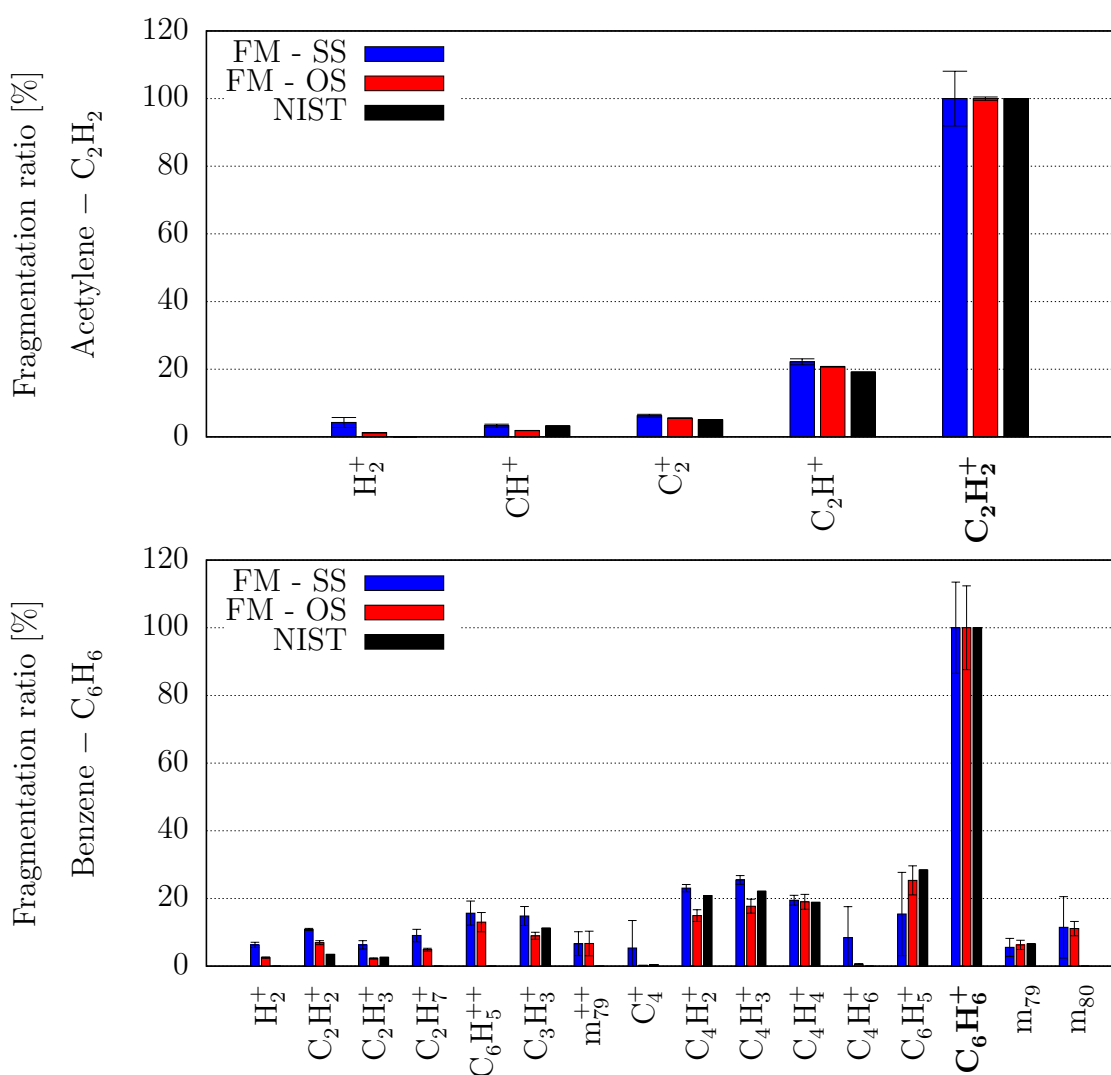


Figure 4.15: Fragmentation ratios – acetylene, benzene. Ratios below 5% are not shown, and the labels on the x-axis represent the molecule contributing the most at a given mass.

Polycyclic aromatic hydrocarbons

The calibration of naphthalene, phenanthrene and pyrene was initially planned for the characterization of the PAH, but despite a heating reaching 195 °C, no signal was visible for phenanthrene and pyrene, or at least not immediately: the presence of residual phenanthrene was observed only in the calibration of species done after the day phenanthrene was unsuccessfully measured, which indicate that phenanthrene probably re-condensed itself in the tubes leading to the vacuum chamber.

Nevertheless, naphthalene was clearly observable in the spectra (see figure 4.16), but only with the SS: due to the difficulty of preparing the sample and getting a high and stable temperature, the measurements for the SS and the OS were performed within two consecutive days. On the second day when the OS was used, no more signal at mass 128 was visible, but a new main peak was visible at mass 86, with other peaks at lower masses corresponding roughly to the fragmentation of hexane (based on NIST data), which was not measured during any calibration campaign. The process of heating, cooling down, and heating again most probably destroyed the molecule, and broke the two rings into several smaller alkanes.

The SS creates more fragments than the literature, which is consistent with the results of the other hydrocarbons.

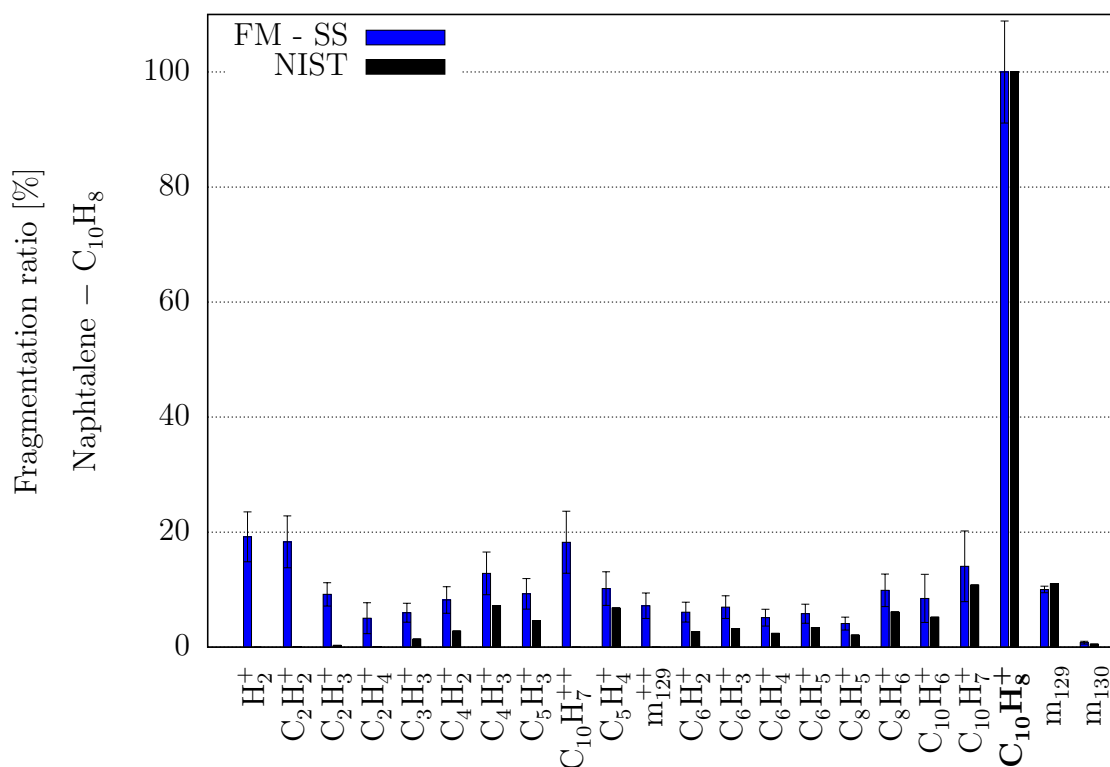


Figure 4.16: Fragmentation ratios – naphthalene. Ratios below 5% are not shown, and the labels on the x-axis represent the molecule contributing the most at a given mass.

4.5.5 C-H-O-bearing compounds

C-H-O-bearing molecules includes alcohols (R-OH), acids (R-COOH), and aldehydes. Ethyl alcohol (or ethanol, C_2H_5OH) has recently been identified in comet C/2014 Q2 (Lovejoy) (Biver et al., 2015).

Alcohols

The two most simple alcohols have been calibrated in this work, i.e. methanol (CH_3OH) and ethanol trans (C_2H_5OH). Both present the same effects as with the hydrocarbons from the previous section:

- more important fragmentation in this work than for NIST,
- SS – OS inversion for the highest masses,
- high intensities for compounds at mass 28 for the OS.

In figure 4.17, the names on the x-axis have been purposely written in their shortest form, to include all possible isomers: for instance, $C_2OH_5^+$ is actually a mixture of $C_2H_5O^+$ and $C_2H_4OH^+$.

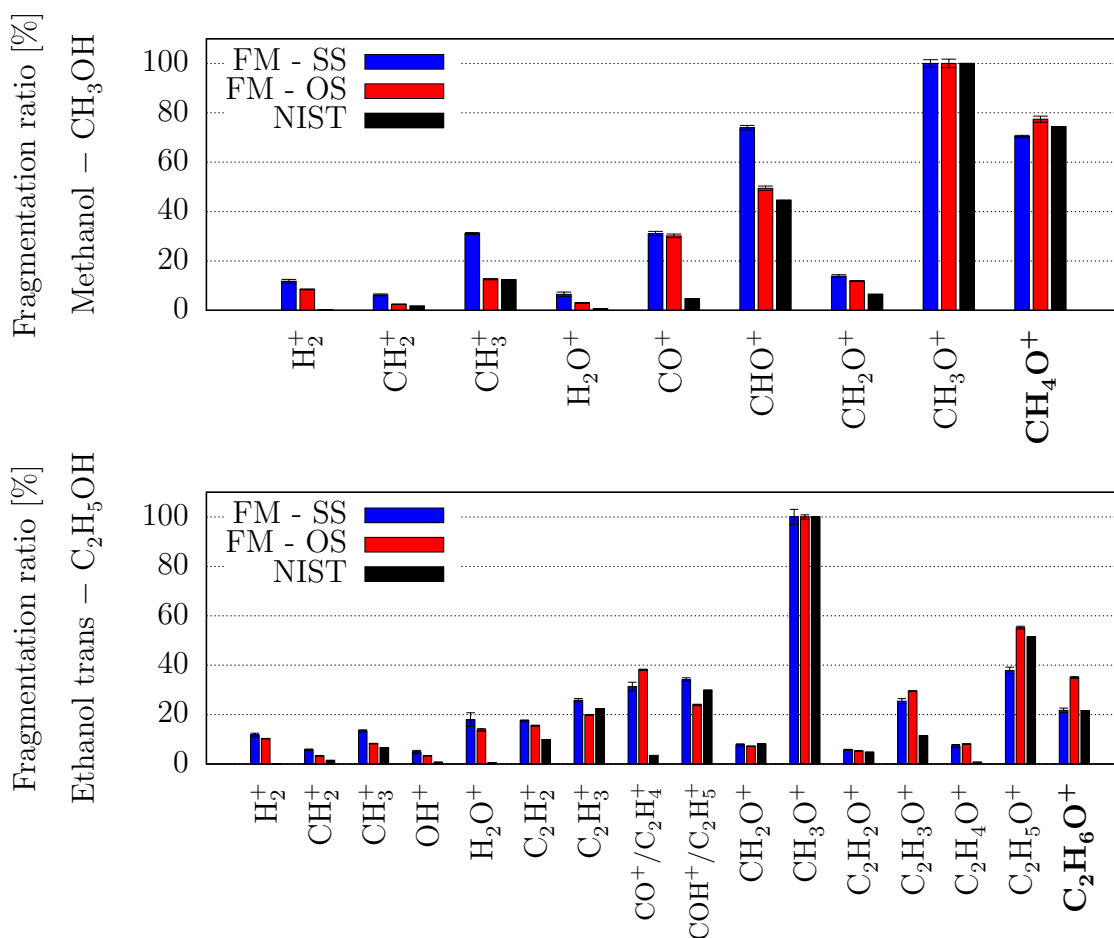


Figure 4.17: Fragmentation ratios – alcohols. Ratios below 5% are not shown, and the labels on the x-axis represent the molecule contributing the most at a given mass.

Acids

The behavior of the OS with formic acid is very interesting and may look like the measurement was corrupted by some contamination (see figure 4.18), but it is consistent with previous observations. CO is still high for the OS and the preference of the OS for the high masses translates into HCOOH being the most abundant fragment, but HCO^+ is still used as reference to be consistent with NIST and the SS.

To a lesser extent, the fragmentation of the acetic acid is similar to the one of the formic acid, with very high ratios for CO^+ and the heaviest masses, propelling the carboxyl group COOH^+ into being the most abundant fragment. Once again, contamination with CO_2 is out of the picture, as it could not explain such a high signal for CO^+ ; and a contamination with N_2 would explain the high signal at mass 28 but would lead to a high signal at mass 14 (N^+ and/or N_2^{++}), which would be seen in an over-abundance of CH_2^+ .

An attempt was made to calibrate glycolic acid (HOCH_2COOH) but once more, this solid compound was not detectable by RTOF in CASYMIR even after heating.

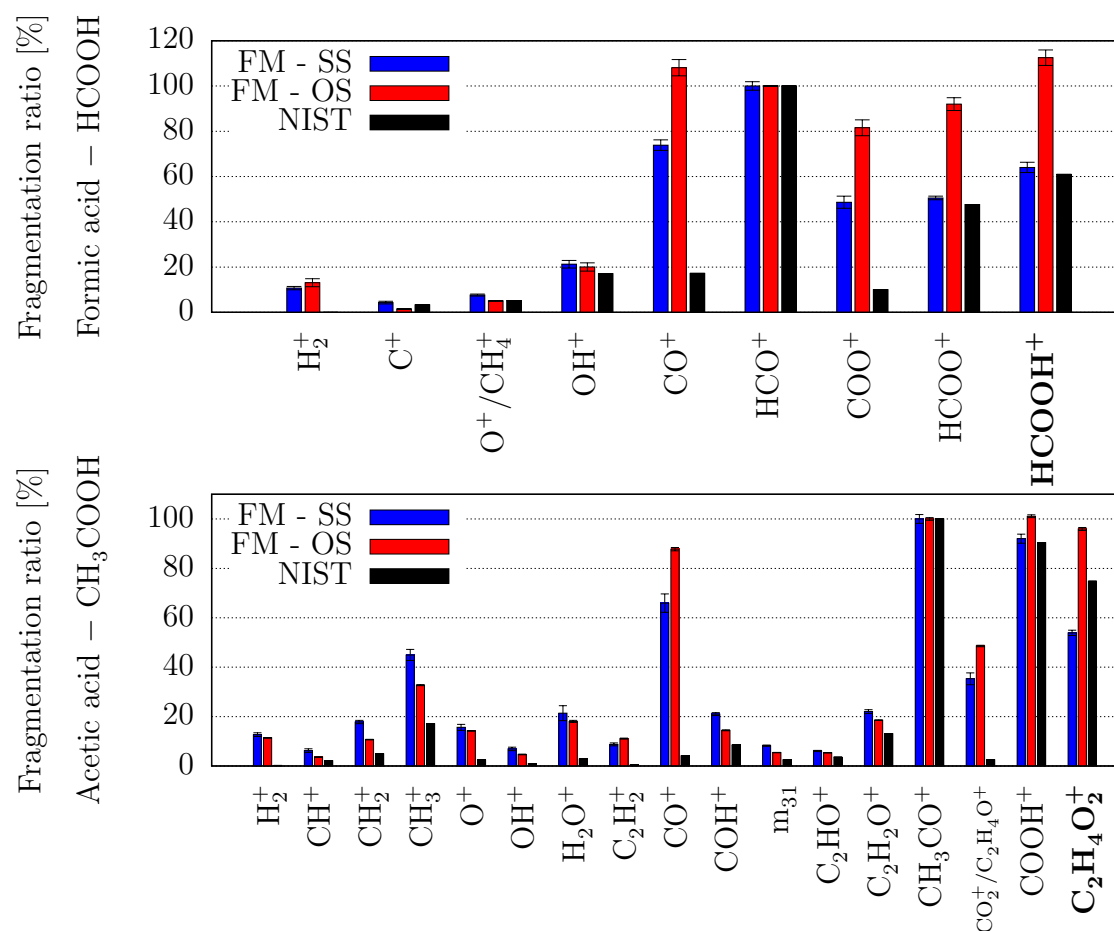


Figure 4.18: Fragmentation ratios – acids . Ratios below 5% are not shown, and the labels on the x-axis represent the molecule contributing the most at a given mass.

Aldehydes

The analysis of the formaldehyde and acetaldehyde results in the same conclusions as previously. The ratios are plotted in figure 4.19.

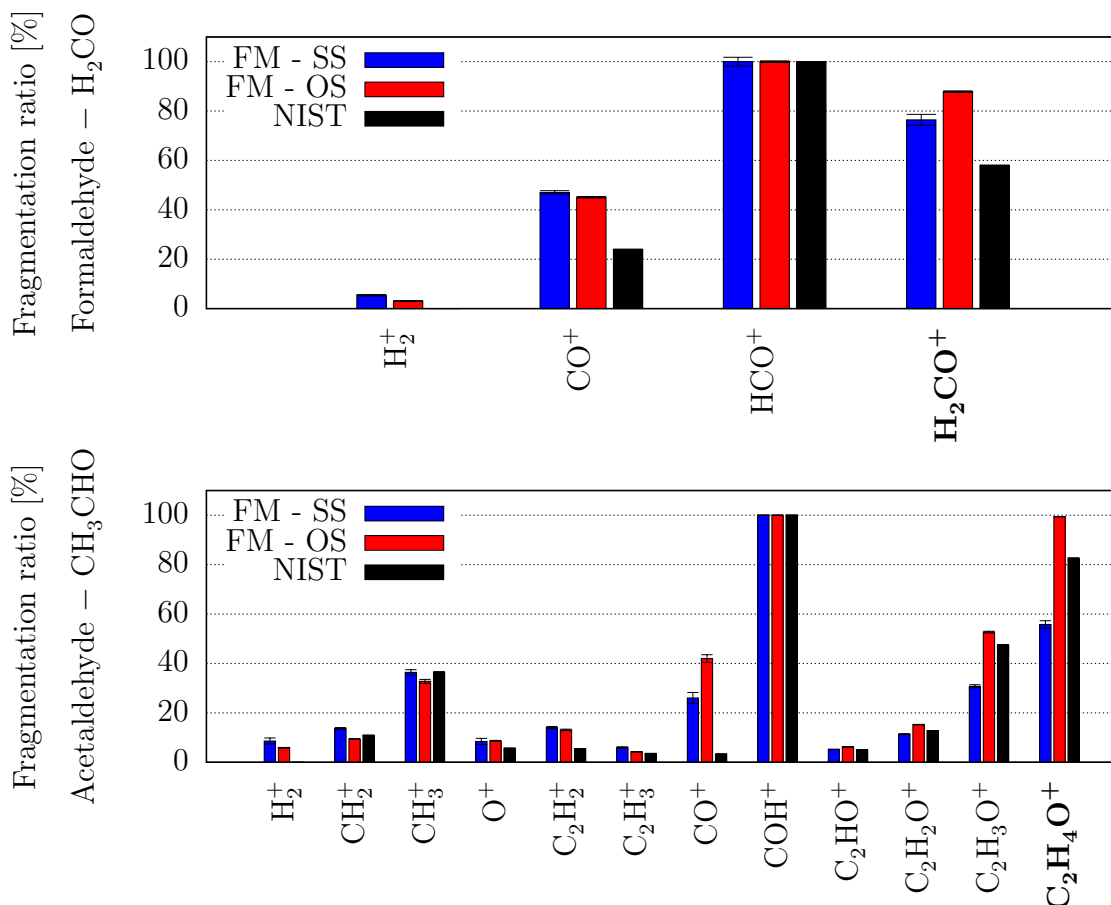


Figure 4.19: Fragmentation ratios – aldehydes. Ratios below 5% are not shown, and the labels on the x-axis represent the molecule contributing the most at a given mass.

4.5.6 C-H-N-bearing compounds

Hexamethylenetetramine (HMT) and triazine were planned to be calibrated, but only triazine was successfully measured, and with the SS only, for the same reasons as for the heavy PAH and the glycolic acid, also in a solid state: no trace of HMT could be observed in the spectra, and triazine was observable with the SS only.

The results for triazine (figure 4.20) are consistent with the previous observations.

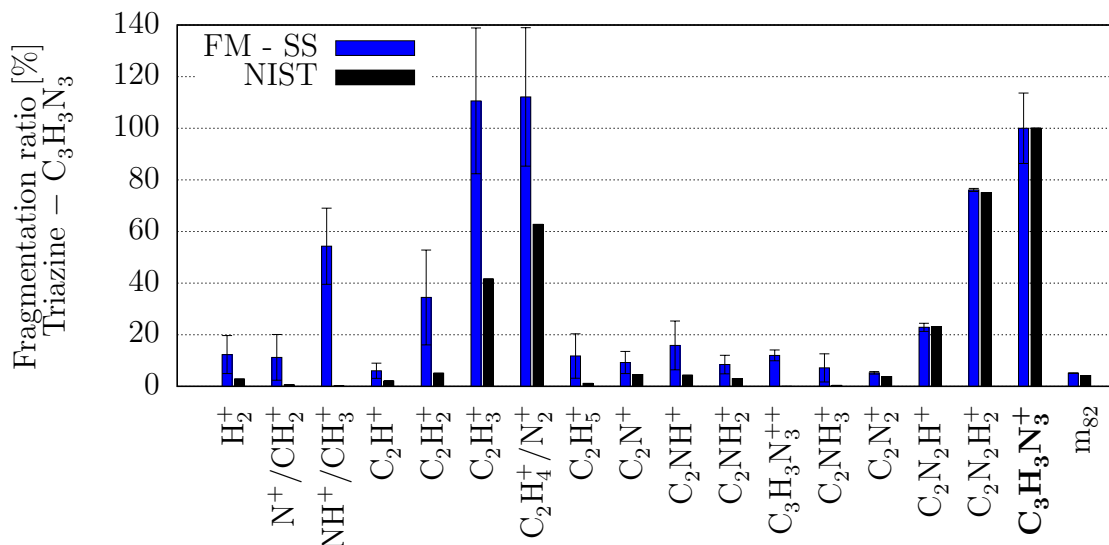


Figure 4.20: Fragmentation ratios – triazine. Ratios below 5% are not shown, and the labels on the x-axis represent the molecule contributing the most at a given mass.

4.5.7 Other compounds

A few other compounds were initially planned, particularly C-H-O-N-bearing molecules such as urea (NH_2CONH_2), formamide (NH_2CHO), and glycine ($\text{NH}_2\text{CH}_2\text{COOH}$), unfortunately none of these solid compounds were successfully vaporized, and the calibration of these species could not be performed.

4.5.8 Sensitivities

Sensitivities are summarized in appendix C and are plotted versus the ionization cross section in figure 4.21. Cross sections for the noble gases are from Szymtkowski et al. (1996), other cross sections are from Kim et al. (2005) and Vinodkumar et al. (2006). The factors for the correction of the N_2 calibrated Granville-Phillips ion gauge are listed in table C.1. The sensitivity for triazine ($\text{C}_3\text{H}_3\text{N}_3$) is not corrected for the pressure readings from the Granville-Phillips and is therefore not included in the plot.

The values presented are the ones from the event data: histogram data have exactly the same behavior, as the sensitivities for events and histogram differ by a factor of 28.0 ± 2.2 . Furthermore, the relation between each mode is reproducible and summarized in table 4.4.

Table 4.4: Sensitivity scale factors for the SS and the OS modes, for the event data. Sensitivities for the histogram data are 28.0 ± 2.2 times higher. Modes 511 for the SS and 513 for the OS have been chosen as references, as they both have the highest sensitivities.

Mode	Scale factor
M501	0.165 ± 0.047
M511	1.000
M521	0.216 ± 0.063
M506	0.092 ± 0.025
M516	0.111 ± 0.029
M526	0.033 ± 0.009
M513	1.000
M543	0.420 ± 0.034

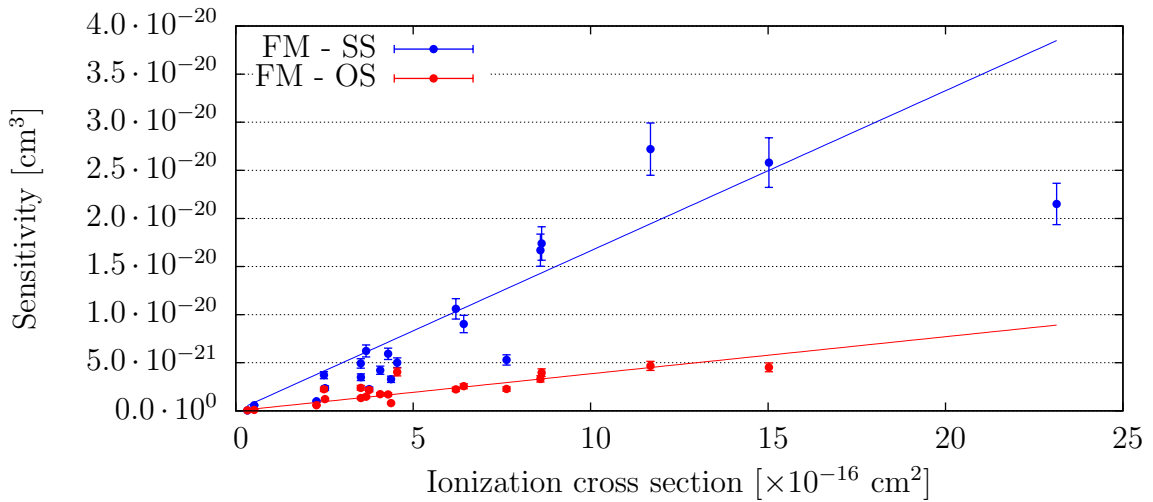


Figure 4.21: Correlation between ionization cross section and sensitivity, for the RTOF FM SS (M511 / events) and the RTOF FM OS (M513 / events). From left (small cross section) to right (higher cross section): He, Ne, H₂O, CO, Ar, CO₂, Kr, Xe, CH₄, C₂H₆, C₃H₈, and C₆H₆.

Although not perfect, the expected correlation between sensitivity and ionization cross section is clear. This means that total ionization cross sections can be used for first order spectral deconvolution when laboratory data for that particular gas species and instrument are not available.

4.6 Results – $D = -1'000$ V

After the change of configuration carried out mid-2014, and the optimization which followed (see chapter 3), some settings with $D = -1'000$ V were set in space for the RTOF FS SS and the RTOF FS OS and did not change between the 03/10/2014 and the 05/06/2015. It is these settings, similar for the FS and for the FM, which have been used for the latest calibration of H_2O , CO , CO_2 , and Kr. Water, carbon monoxide and carbon dioxide have been measured to establish a link between the three states associated to the drift values of $-3'000$ V, $-1'800$ V, and $-1'000$ V, and krypton was measured to verify the capability of RTOF to measure isotopic ratios. These measurements were made with reduced voltages and therefore reduced performance.

The fragmentation and the sensitivity of RTOF to these species is discussed hereafter, and the results will be then extrapolated to estimate some values for the analysis of space data.

4.6.1 H_2O , CO , CO_2 and krypton

Fragmentation

The fragmentation ratios for the four studied compounds are presented in figure 4.22, the numerical values are listed in appendix B.

An additional ratio is available for water: H^+ / H_2O^+ . With the “new” settings, the energies are lower, the ions are slower, and the time of flight of the ions is longer; with an unchanged extraction delay, mass 1 is therefore visible in the spectra and can be quantified here. The fragmentation ratios are otherwise very similar to NIST and to the previous settings, for the SS as well as for the OS. The presence of H_2^+ was not expected due to the lack of recombination at such low pressures and for such a short time – between their creation and the time they hit the MCP, the ions survive for $500 \mu s$ in the best case – but a peak at mass 2 is clearly visible for the SS and presents a nice correlation with the abundance of water. H_2^+ is most probably formed during the ionization process, when the two newly fragmented H atoms are still close enough to form H_2^+ .

The OS ratio $^{13}CO_2^+ / CO_2^+$ is off by 12.5 %, which is reminiscent of the similar high ratio for $D = -3'000$ V, to a lesser extent. In this case though, because of the small deviation compared with the literature, a bias induced by formamide contamination remains possible.

Another observation worthy of note is the intensity of CO^+ , fragment of CO_2 : systematically higher for the OS than the SS or than NIST in all the calibration measurements done with $D = -1'800$ V, this fragment has now equivalent abundances for the SS than for NIST, and a lower one for the OS.

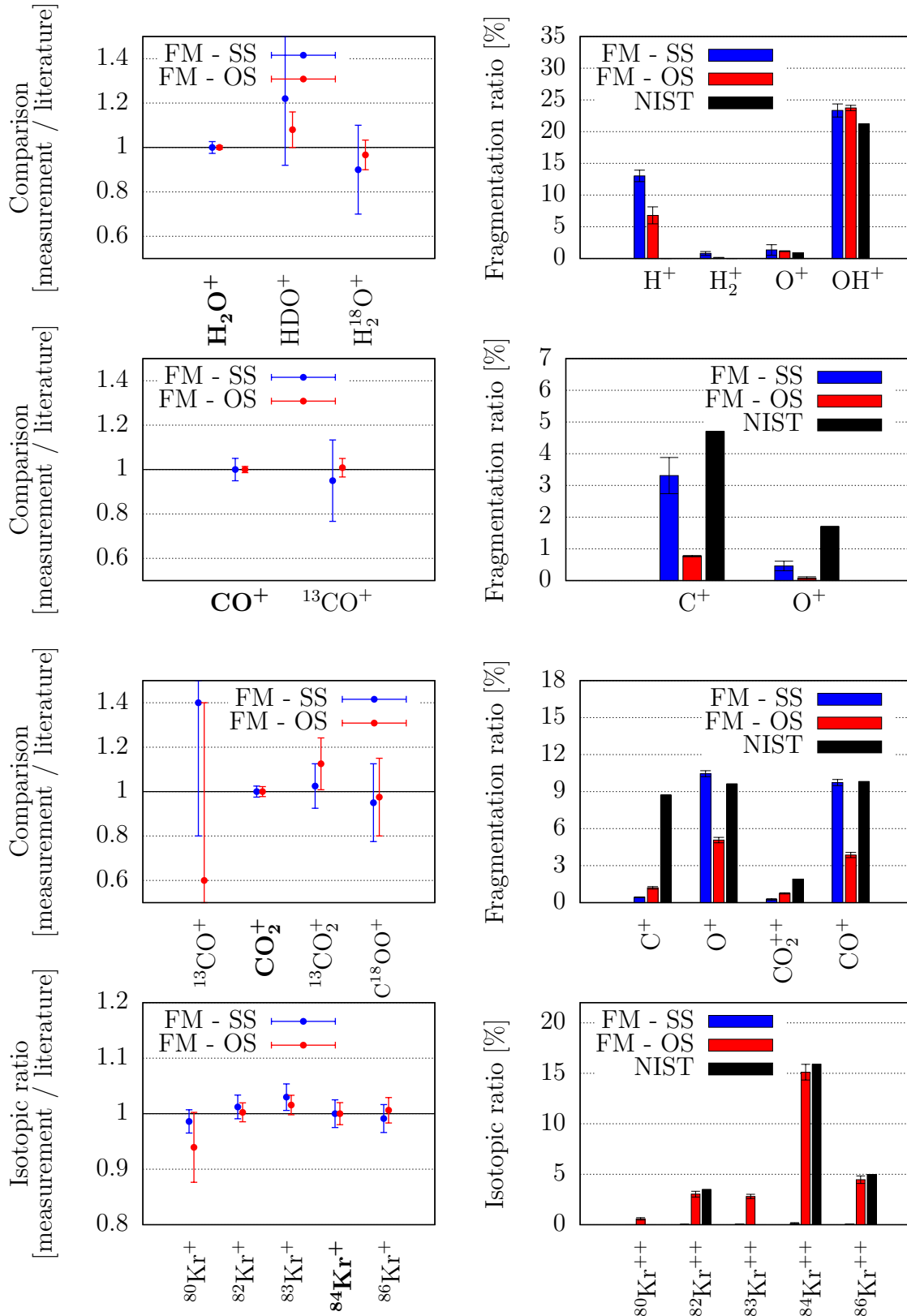


Figure 4.22: H₂O, CO, CO₂, and Kr ratios. For H₂O, CO, and CO₂, on the left side, the points correspond to the isotopolog ratios measured with RTOF divided by the ones from literature (NIST); on the right side, fragmentation ratios are given relative to the parent. For Kr, singly charged isotopes are shown on the left panel and are relative to the literature (NIST), doubly charged ions are shown on the right panel and are relative to the main isotope (⁸⁴Kr⁺). When not specified, C = ¹²C and O = ¹⁶O.

Sensitivity

Sensitivities are given in appendix C. Unlike in section 4.5.8 where the scale factors were given relative to mode 511 and 513, the factors are given here relative to modes 521 for the SS and to mode 523 for the OS. First of all because the high emission modes 521 and 523 are more frequently used in space than any other mode, and second because the sensitivities for these two modes are the highest with the optimized settings found with $D = -1'000$ V.

The ratio histogram / event data for the SS is here a bit different than for $D = -1'000$ V, and is equal to 20.5 ± 1.5 (was 28.0 ± 2.2 with $-1'800$ V).

Table 4.5: Sensitivity scale factors for the SS and the OS modes, for the event data. Sensitivities for the histogram data are 20.5 ± 1.5 times higher. Modes 521 for the SS and 523 for the OS have been chosen as references, as they both have the highest sensitivities.

Mode	Scale factor
M501	0.118 ± 0.032
M511	0.229 ± 0.062
M521	1.000
M506	0.068 ± 0.012
M516	0.499 ± 0.135
M526	0.112 ± 0.030
M513	0.116 ± 0.001
M523	1.000
M543	0.059 ± 0.001
M553	0.517 ± 0.009

4.6.2 Extrapolations

In order to extrapolate the results from $D = -1'800$ V to $D = -1'000$ V, and thus being able to use the values from the section 4.5 for the analysis of flight data, we first need to study the species common to these two configurations: H_2O , CO , CO_2 , and Kr. The values will then be applied on a GCU spectrum acquired in flight with the RTOF FS.

$D = -1'800$ V \rightarrow $D = -1'000$ V

The main differences between $D = -1'800$ V and $D = -1'000$ V are listed below. The isotopologues will not be mentioned here, as the literature values lie within the error bars of the measured values (except $^{13}\text{CO}_2^+$, already discussed previously).

- One of the clear trends concerns the doubly charged ions: for the OS, the amount of doubly charged ions is 1.53 ± 0.05 times smaller with $D = -1'000$ V than with $D = -1'800$ V; for the SS it's even clearer, as almost no doubly charged ions are visible with $D = -1'000$ V, neither for Kr nor for CO_2 .

- H₂O: proportions are the same for the SS and the OS, within a few percent.
- CO: proportions are the same for the OS, but for the SS the C⁺ and O⁺ fragments are less abundant for D = -1'000 V, by a factor of 3 for C⁺ and 15 % for O⁺.
- CO₂: compared to the results of D = -1'800 V, CO⁺ fragment is less abundant for both the OS (× 3.3) and the SS (× 2.0); O⁺ fragment is more abundant for both the OS and the SS (× 1.4 both); C⁺ fragment is equivalent for the OS and lower for the SS (× 5.9).

In summary, there does not seem to exist clear rules to extrapolate the fragmentation ratios from one set of settings to another one, except concerning the doubly charged ions. The fragmentation appears to be not only instrument dependent, but species dependent as well, at least regarding H₂O, CO, and CO₂. But as these molecules all contain C and O, and as we've seen already the particular behavior of the compounds of masses 12 and 19 in the optimization chapter, there would still be a possibility to find a correlation for molecules including other fragments than C⁺, O⁺, and CO⁺. In any case, a new ground calibration with specifically chosen species would be needed to confirm the analysis of the space data, or if the settings are changed again.

Regarding the sensitivity, based on the data available for the RTOF FM and for H₂O, CO, CO₂, and Kr, an estimation can be given for the correction factors to be applied between D = -1'800 V and D = -1'000 V. This factor is 3.54 ± 0.20 for the OS, and $(2.63 \pm 0.55) \cdot 10^{-2}$ for the SS. The detailed procedure to apply these factors is described hereafter for the extrapolation of the sensitivity for helium.

D = -1'000 V → Flight data

As for the spectrum analysed in 4.4.4, a model has been applied to a GCU spectrum acquired with the OS on 7th January 2015, at 26 km from 67P/Churyumov-Gerasimenko's surface, with an emission current of 200 μA and an extraction frequency of 10 kHz (mode 183). Figure 4.23 shows parts of the GCU spectrum, fitted using only the intensities of the parent molecules and a global mass-dependant FWHM as fitting parameters; the intensities of the fragments are given by the fragmentation pattern and isotopic ratios presented in appendix B.

The model fits the data well, with typical fit errors for the intensities of the order of 1 %. A significant difference is found only for CO₂: the fragmentation of CO₂ into CO₂⁺⁺ and CO⁺ is 10 % lower than predicted by the calibration values.

The area of the peaks integrated as defined in section 2.2.1 are summarized in table 4.6. The densities n_i have then been calculated with the sensitivities S_j from the RTOF FS tables with D = -1'000 V according to equation 4.4:

$$n_i = \frac{I_i}{S_j \frac{Q_{ij}}{\sum Q_{ij}} I_{em}} \quad (4.4)$$

i designates the parent fragment, j a daughter. I_i is the current generated by the ions of the parent molecule (i.e. the number of counts in the integrated peak times q the elementary charge), I_{em} is the emission current, here 200 μA, and the ratio

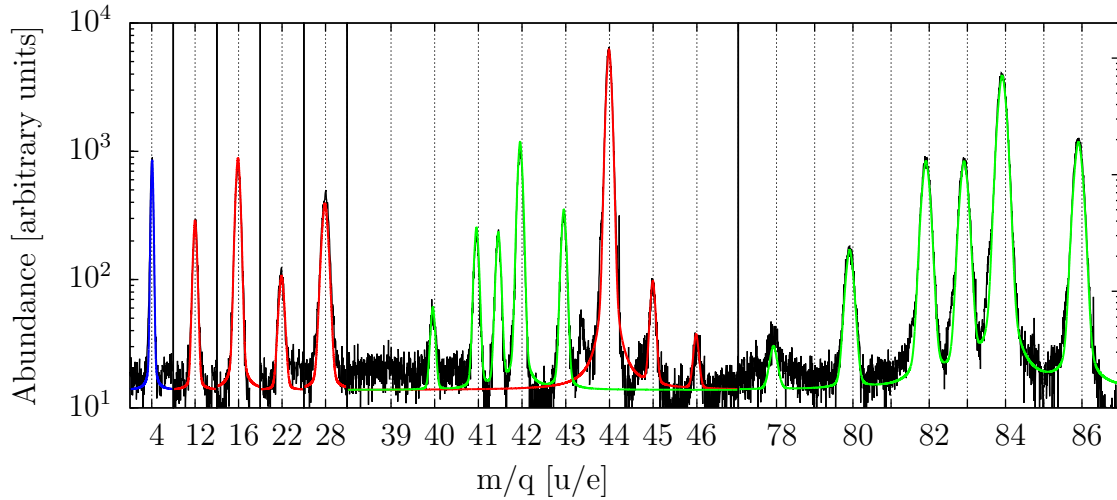


Figure 4.23: RTOF FS OS GCU spectrum with its model generated with the calibrated fragmentation patterns of 4 compounds: He, H₂O (not shown here), CO₂, and Kr.

$Q_{ij} / \sum Q_{ij}$ corresponds to the fragmentation ratio of the parent divided by the sum of the fragmentation ratios of all the fragments.

As no sensitivity value is available for helium with the FS and $D = -1'000$ V, we here apply the correction factor for the OS found in the previous paragraph (3.54 ± 0.20): $S_{\text{He}_{1000}} = (2.42 \pm 0.15) \cdot 10^{-22} \text{ cm}^3$.

Compound	$S_i [\text{cm}^3]$	A_i	Q_{ij}	$n_i [\text{cm}^{-3}]$	Ratio [%]
He	$2.42 \cdot 10^{-22}$	8'708	1.00	$(2.88 \pm 0.23) \cdot 10^{10}$	34.4 ± 2.8
H ₂ O	$5.73 \cdot 10^{-21}$	425	0.75	$(7.87 \pm 0.63) \cdot 10^7$	0.09 ± 0.01
CO ₂	$6.84 \cdot 10^{-21}$	207'344	0.89	$(2.73 \pm 0.22) \cdot 10^{10}$	32.7 ± 2.7
⁸⁴ Kr	$1.05 \cdot 10^{-20}$	178'281	0.49	$(2.75 \pm 0.22) \cdot 10^{10}$	32.9 ± 2.7

Table 4.6: Example of density calculations using the calibration values presented in this work. H₂O has a cometary origin and is not part of the GCU gases. A is the area under the peak, not yet multiplied by q .

These results demonstrate that the calibrated sensitivities are applicable to the RTOF FS, giving relative abundances very close to the ones expected for the GCU gases. For the determination of absolute density though, some non-negligible differences have to be expected, due to the different MCP voltages and the different threshold levels between the FM and the FS. For flight data, we need as a first step to apply the sensitivities given in this work on the RTOF data, and then use the absolute density provided by COPS to compute absolute densities from RTOF.

5. RTOF results from flight

This chapter is dedicated to the analysis of space data acquired with the optimized settings shown in chapter 3 and the application of the sensitivities calibrated in chapter 4.

In this chapter, only the main compounds seen by the RTOF FS in flight will be discussed, as an example to demonstrate the capabilities of RTOF. The data will be analyzed within a time range from August 2014, when *Rosetta* arrived within 100 km from the nucleus, to May 2015, at equinox. After this time period, the filament failure for the SS required the start of a new optimization which is still ongoing at the time of writing. In addition, the distance to the comet was too large to get significant results with RTOF.

The first section will point out one of the main difficulties faced during the data reduction, defined here as *baseline variations*. The next sections will focus on the coma heterogeneity and the seasonal and diurnal variations. In the following, the spacecraft attitude – altitude, longitude, latitude, solar array angle – are from Scholten et al. (2015).

5.1 Baseline variations

Since the exit of hibernation and more particularly since August 2014 and the arrival of *Rosetta* in the vicinity of 67P/C-G, very large variations of the baseline between the peaks are observable in the RTOF spectra. The noise added to the spectra even exceeds the intensity of the most abundant species such as H₂O and CO₂ in some cases.

A correlation is observed with the +Y Solar Array orientation Angle (SAA): this value is a good indicator of the angle between the Sun and the instrument platform. Figure 5.1 shows the evolution of the baseline level for the SS between August and November 2014: whereas the water signal is typically a few thousands of counts, the baseline level can reach several tens of thousands of counts. An equivalent plot for the OS is given in figure 5.2.

The baseline varies to such an extent that its intensity has been represented in a log scale for the SS in figure 5.1; a smoothing was done (blue curve) to ease the visualization of the correlation with the SAA, but raw data were kept in the plot (gray curve) to give an idea of the amount of spectra where the intensity of the baseline goes above 10³.

The variations have a much smaller amplitude for the OS and are therefore represented with a linear scale. With the OS, the biggest variations are visible for short but intense SAA changes, occurring during a slew for instance. Even so, the baseline level does not reach a few hundred of counts.

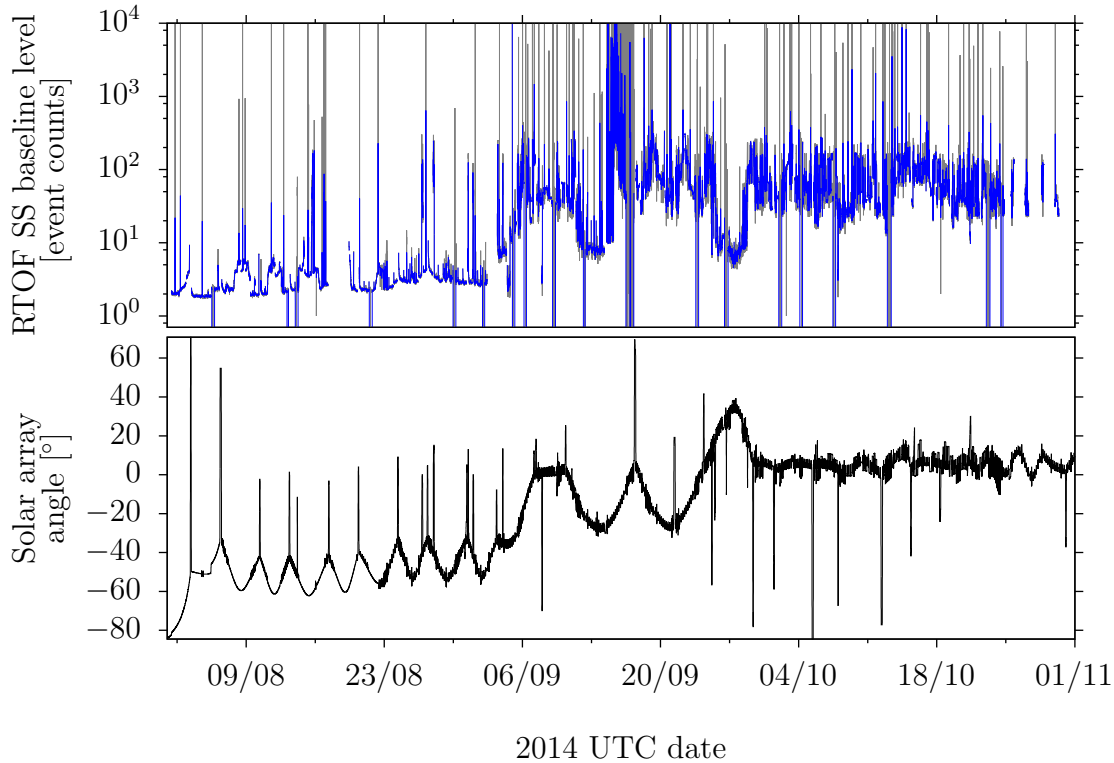


Figure 5.1: Top: intensity of the baseline level for the SS (gray: raw data; blue: smoothed data). Bottom: solar array angle. This level has been calculated using the mean value of all the points between mass 8 and mass 10, as no compound is expected in this region of the spectrum. It has nevertheless been verified that no peak was visible within this mass range for all the spectra analyzed. The intensity of the baseline level is of the same magnitude within a spectrum.

Variations are too fast to be attributable to a change in temperature:

- the electronic boards, located a few tens of centimeters inside the *Rosetta* spacecraft, are thermally more stable than the sensor head (where the ion sources are located),
- the monitoring of the ion source backplane temperature do not show any significant correlation with the baseline level.

The most probable origin for these variations is to be found in the solar radiation (UV), reflected in the instrument for particular attitudes of the spacecraft.

In an attempt to reduce the effect of the solar radiation, the cover was moved to position 14, leaving the sensor head opened with an angle of approximately 42° . This solution has not shown a consistent difference compared with a fully opened cover; the cover was set back to position 1 on 10/04/2015.

Due to its considerable impact, this effect needs to be accounted for in the data analysis, particularly for the SS.

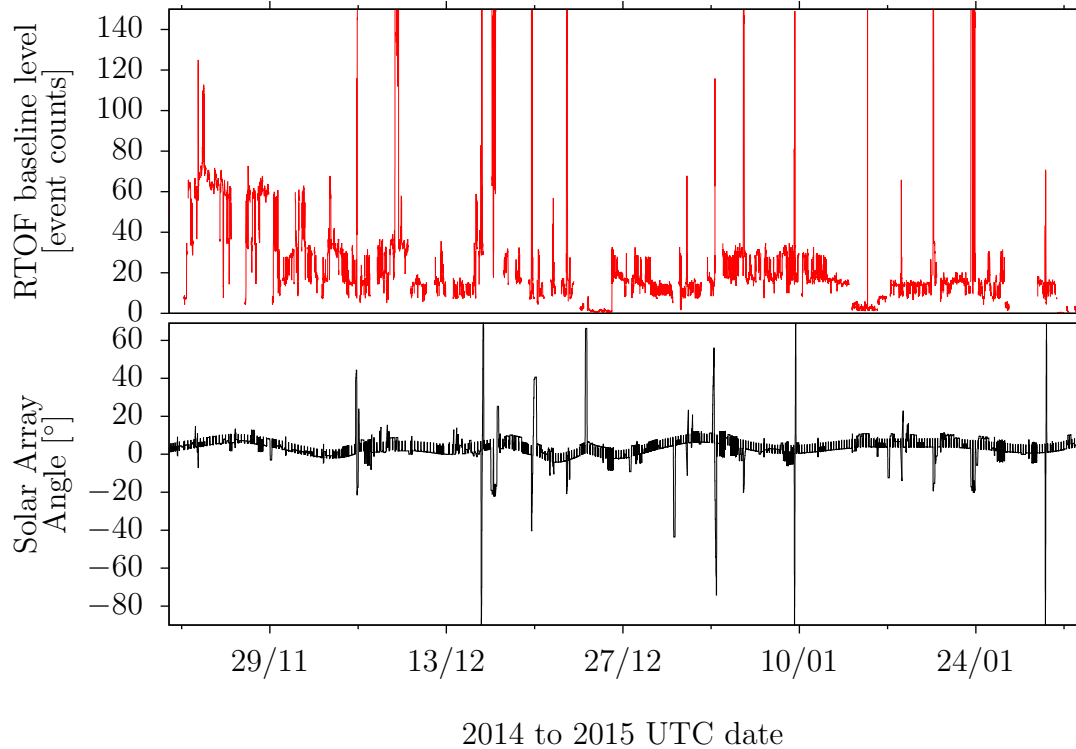


Figure 5.2: Top: intensity of the baseline level for the OS. Bottom: solar array angle. The calculation process is the same as in figure 5.1.

5.2 Seasonal variations

As most other bodies in the Solar System, 67P/C-G spins, with a period of 12.4 h. The spin axis is not normal to the orbital plane (Mottola et al., 2014), meaning that 67P/C-G has seasons. Seasonal variation is seen in the different abundances of the measured species, depending on the location of *Rosetta* in the coma.

To properly calculate densities out of RTOF raw data, two steps are necessary and detailed below: the correction of COPS raw density, and the scaling of RTOF data to COPS corrected density.

First: COPS was calibrated using N_2 and therefore needs to be corrected according to the abundances of the main species seen by RTOF. The COPS nude gauge is a Bayard-Alpert gauge, and its sensitivity to species other than N_2 is comparable to the one of a Granville-Phillips ion gauge. The scale factors from table C.1 can therefore be used for the correction of the density given by COPS, provided that a ratio of the most abundant species can be given by RTOF or DFMS.

Second: as we have seen in the chapter 4, RTOF sensitivity values are available for H_2O and CO_2 for the FM, and can be applied to the FS provided that a scaling with COPS is performed. For the chosen time period, the scale factor needed to get coherent values between COPS and RTOF was approximately 0.13, meaning that one has to multiply the RTOF FM sensitivities by this number to get RTOF FS densities in accordance

with COPS. This factor depends on the settings of the instrument, and particularly on the MCP voltage and the threshold level. These parameters did not change in December 2014, nor in January 2015.

Figure 5.3 shows the evolution of the H_2O and CO_2 densities measured by the RTOF FS OS over two months, along with the species-corrected COPS nude gauge density, the latitude of the comet above which *Rosetta* flew, and the distance of the spacecraft from the nucleus. COPS density is corrected according to the relative abundances given by RTOF; RTOF densities are sensitivity corrected and scaled to COPS.

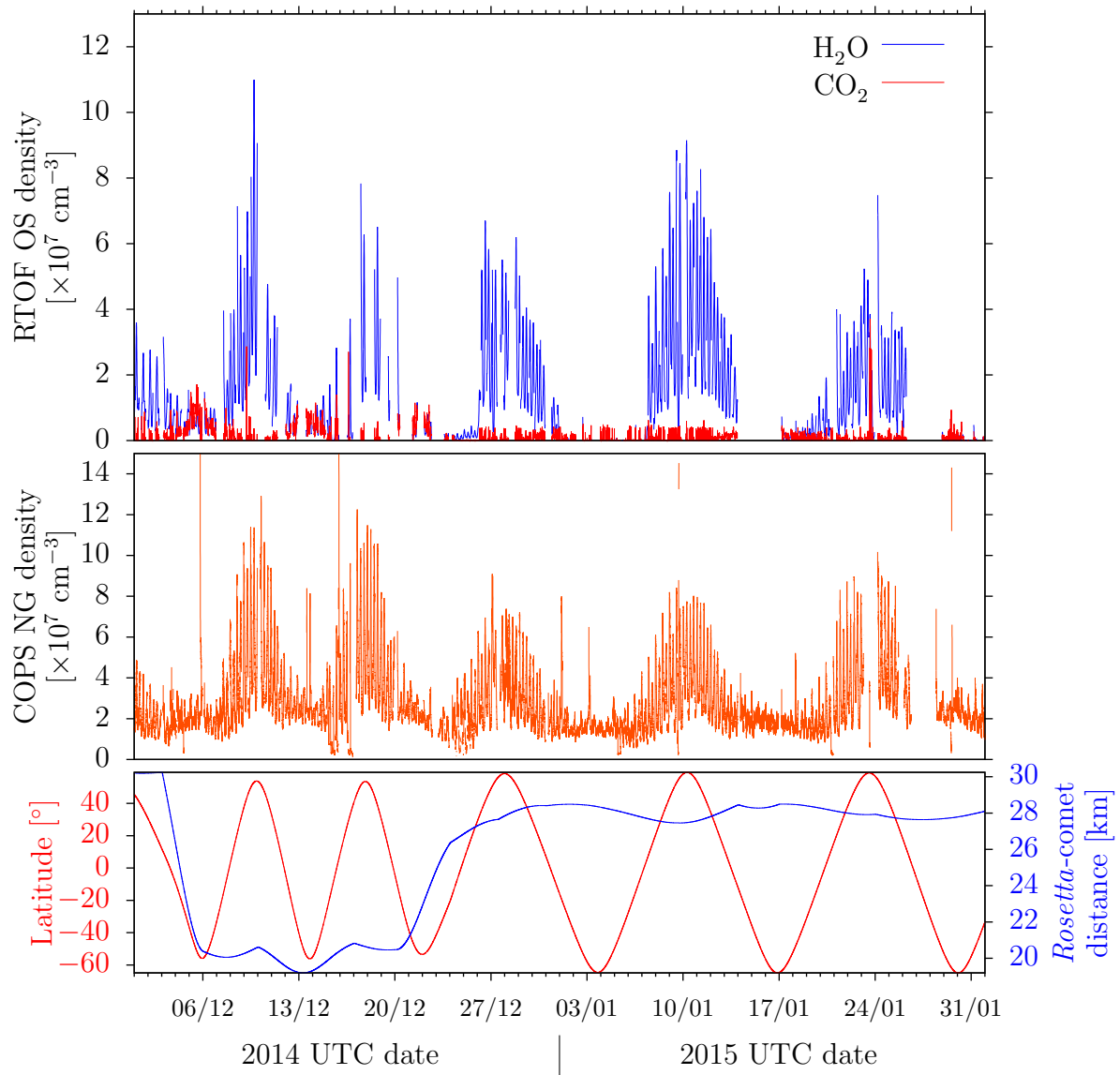


Figure 5.3: Seasonal variations measured by RTOF and COPS in December 2014 and January 2015. Top: RTOF FS densities acquired with the OS for H_2O (blue) and CO_2 (red). Middle: COPS nude gauge density. Bottom: latitude of the nadir view of the spacecraft (red) and distance from the nucleus (blue).

A clear correlation between the water density and the latitude is visible, indicating an over-abundance of H_2O in the northern hemisphere compared to the southern hemisphere. In December 2014 and January 2015, the cometary summer was in the northern hemisphere; equinox for 67P/C-G was on 13/05/2015.

Another interesting point is the behavior of CO_2 , showing an anti-correlation with H_2O : the CO_2 abundance reaches its maximum for the most negative latitudes – this is particularly visible in figure 5.3, on 06/12/2014 and on 13/12/2014. For certain time periods, the abundance of CO_2 is even higher than that of H_2O . This illustrates the strong heterogeneity of the coma of 67P/C-G mentioned by Hässig et al. (2015).

5.3 Diurnal variations

A zoom in on the second week of January 2015 is shown in figure 5.4 and highlights diurnal variations, with a periodicity of 12.4 h corresponding to one comet rotation.

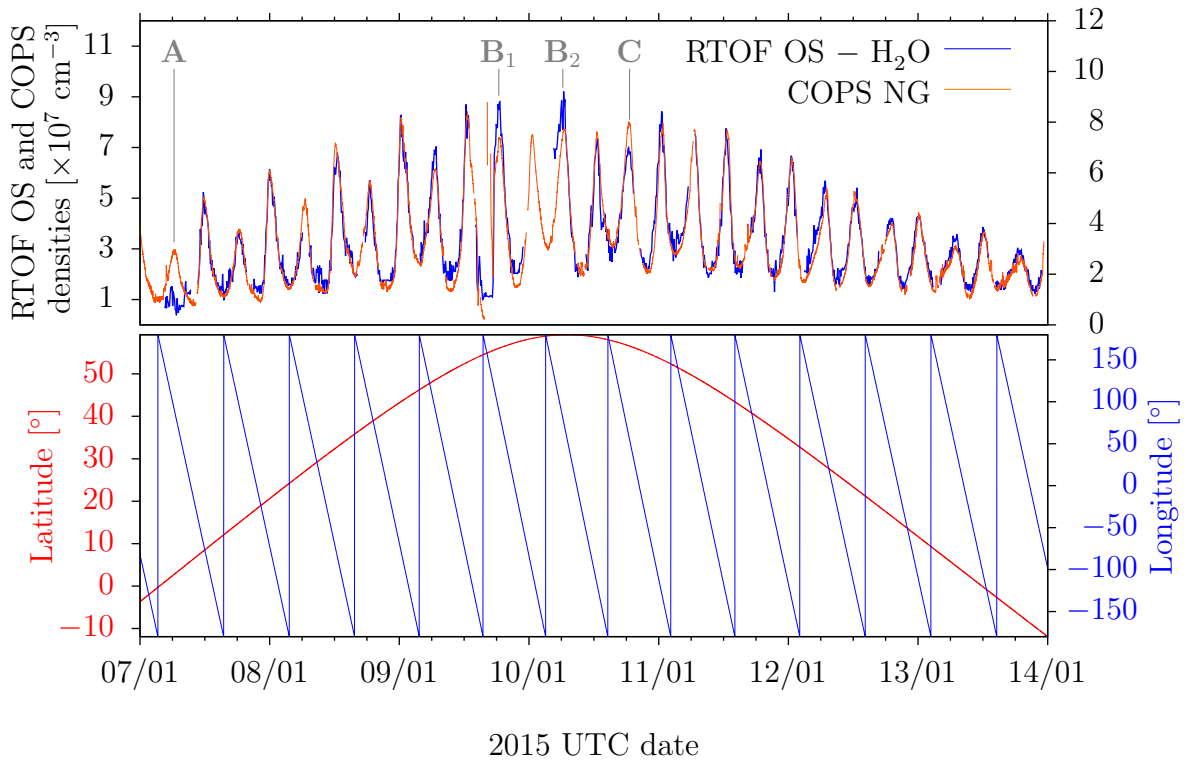


Figure 5.4: Diurnal variations measured by RTOF and COPS in the second week of 2015. Top: RTOF FS densities acquired with the OS for H_2O (blue) and COPS nude gauge density (orange). Bottom: latitude and longitude of the nadir view of the spacecraft.

The agreement with COPS is good except for three representative cases discussed below and labeled in figure 5.4 as A, B (1 & 2), and C.

A The small amount of water measured by RTOF compared to the COPS density can be explained by the fact that for low densities, i.e. for low peaks, the variation of the baseline level has a stronger effect. Hidden by the noise level, the small peaks are not visible below a given density.

B After a maneuver, or more generally when an ion source remains cold for few hours or more, an outgassing effect is visible after the switch ON. When OFF, RTOF cools down and becomes a trap for the cometary dust particles and the propellant droplets, which sublime as RTOF is warmed up during the switch ON. This effect occurs as well when only one source is used: the other one becomes cooler. In any case, this phenomenon leads to an overestimation of all the RTOF densities.

C In this case, the reason why COPS and RTOF differ for this particular maximum remains unknown. An underestimation of the RTOF signal due to a high baseline level is not expected for such a relatively high density; furthermore, COPS and RTOF were both in a thermally stable state; finally, no other species seem to be contributing to the total density measured by COPS. A more detailed analysis with higher statistics would be required to provide an explanation for this difference.

5.4 Summary

Putting everything together, one can map the densities of water and carbon dioxide on a sphere with a 10 km radius around the mass center of 67P/C-G, to characterize the coma of the comet. This way, no assumption is done regarding the origin of the gas: a simple projection on the surface would not be representative of the complexity of the surface, nor would it be representative of the changing field of view of the instrument.

The intensities of the peaks were scaled following a $1/r^2$ law, and the angular resolution has been chosen equal to 12° for both the latitude and the longitude, i.e. a mean value was calculated using the points located in a $12^\circ \times 12^\circ$ area. No data points are available above a latitude of 60° or below -60° . Results are shown in figures 5.5 and 5.6 for the OS and the SS respectively.

The measurements provided by the OS are clear and confirm a heterogeneous distribution of water and of carbon dioxide in the coma of 67P/C-G, with a higher abundance of H_2O at positive latitudes than at negative latitudes, and the opposite for CO_2 .

Knowing this, a similar trend may be guessed for the distribution of H_2O and CO_2 seen by the SS, but definitely not as clear as with the OS. An explanation is given by the statistics: due to the variation of the baseline level discussed in section 5.1, many points had to be filtered to obtain the map for the SS.

With both sources, the asymmetry in the abundance of the major volatiles is clear.

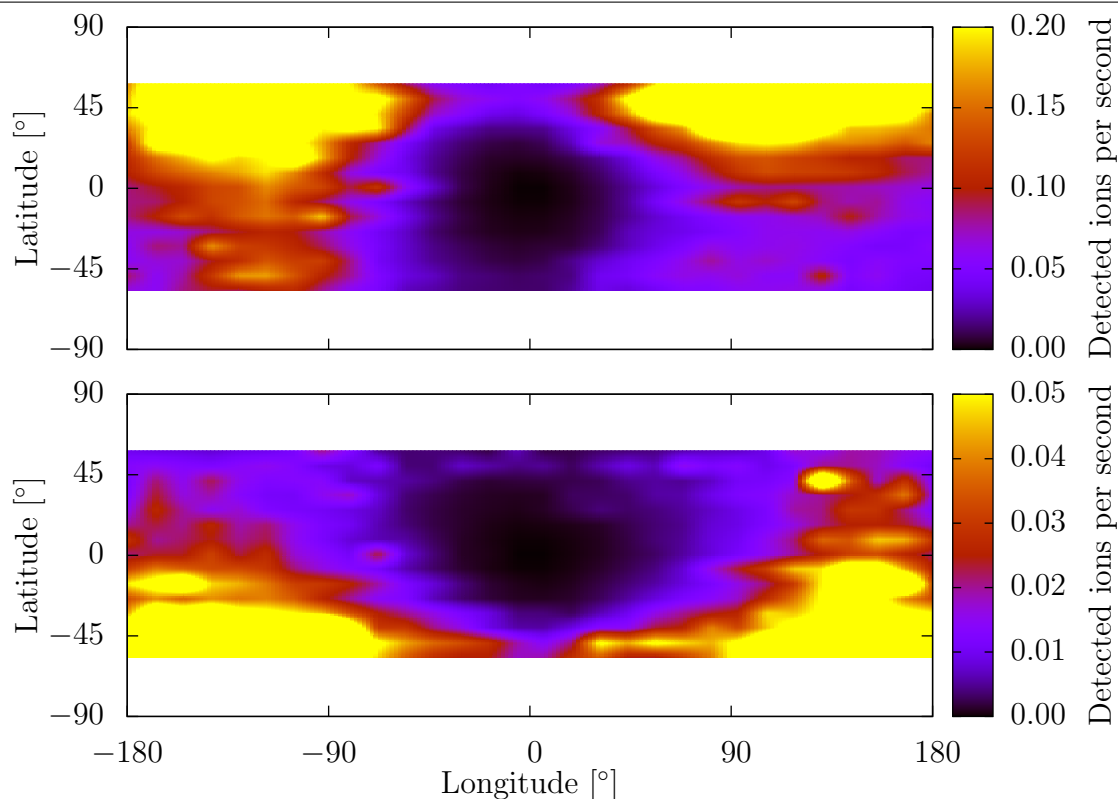


Figure 5.5: RTOF OS H_2O (upper panel) and CO_2 (lower panel) maps of 67P/Churyumov-Gerasimenko's coma, integrated over the period 01/10/2014 – 01/05/2015. Intensities have been scaled to a distance from the nucleus of 10 km.

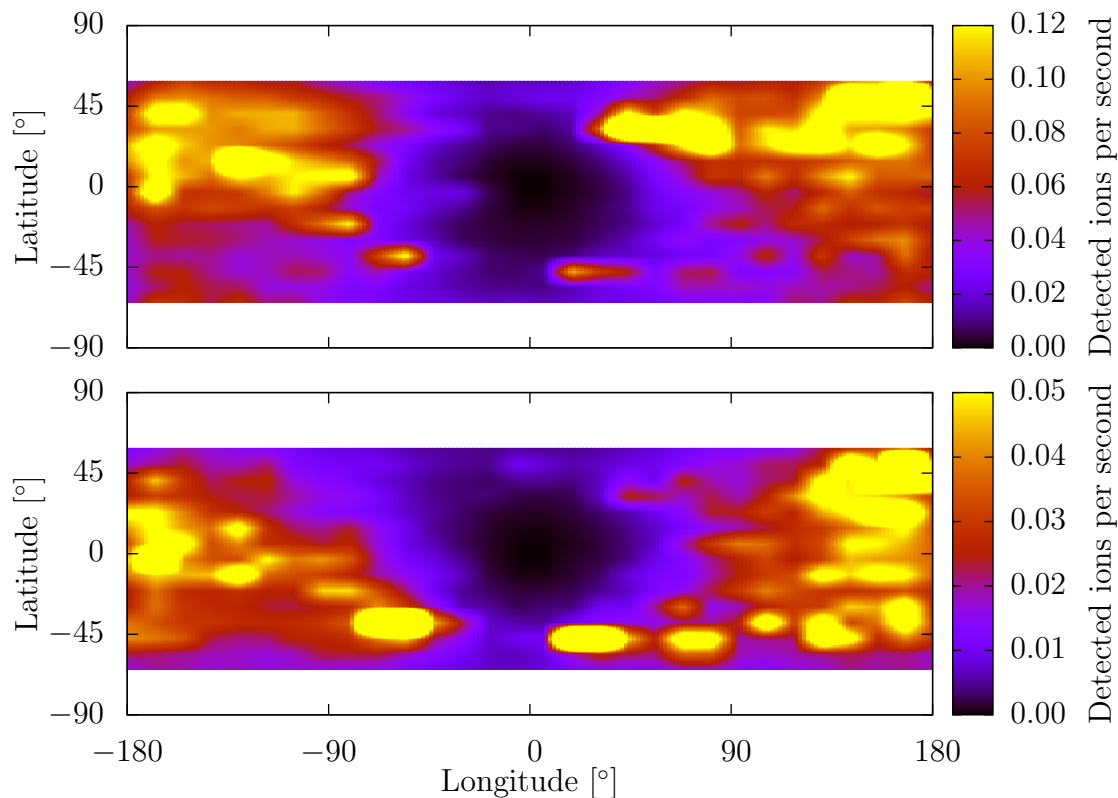


Figure 5.6: RTOF SS H_2O (upper panel) and CO_2 (lower panel) maps of 67P/Churyumov-Gerasimenko's coma, integrated over the period 01/10/2014 – 01/05/2015. Intensities have been scaled to a distance from the nucleus of 10 km.

6. Conclusions and perspectives

The Reflectron-type Time-Of-Flight mass spectrometer is a powerful instrument designed to achieve high performance: developed with the most recent techniques in mass spectrometry, RTOF also meets the constraining requirements inherent to the space industry.

Despite a dramatic technical failure and an initial drop of performance, RTOF slowly recovered over the years and achieved higher and higher performance, using different automatic optimizations on the ground as well as manual optimizations in flight. Although optimizing an instrument is a never-ending process, especially when the operational settings are far from the ones initially conceived, a procedure has been established to shorten the optimization time. This procedure consists in running an APSA optimization on the ground, and to upload and test the optimized parameters on the model in flight, followed by a manual fine tuning in flight. Being able to run some optimizations in the lab is undoubtedly a tremendous advantage.

As a result, and compared to the settings applied during the Lutetia flyby, the mass resolution for the SS and the OS in neutral mode was multiplied by a factor of 2, and higher peak intensities were obtained. Regarding the optimization of the SS with the filament #2, the fine tuning of the RTOF FS with the optimized settings from the lab remains to be done and will be performed in the next months. Since the performances degrade with time, a new optimization of the OS may also be considered for the next weeks.

The results from the calibration measurements and the differences observed with other references confirmed the necessity of creating a database specific to each instrument for as many species as possible.

Using the knowledge acquired during the optimization and calibration campaigns, the two major cometary volatiles (H_2O and CO_2) have been studied, revealing diurnal and seasonal variations of the coma, and a clear asymmetry in the abundance of the major volatiles between the two cometary hemispheres.

In spite of a major failure of the high voltage converter and a failure of one of the SS filaments, and thanks to the long-term involvement of many people, RTOF is still operational and keeps sending data from 67P/Churyumov-Gerasimenko. With increasing performance and a distance from the nucleus decreasing until the end of the mission, RTOF may detect more and more minor volatiles, and may have its moment of glory with the detection of very heavy molecules. If such an event occurs, a calibration of the supposed molecules with the lab model will probably be necessary to confirm their identities.

A. RTOF voltage tables

Table A.1: RTOF FS settings – OS (neutrals). All voltages are given in V.

Date	2003	29/03/2014	20/04/2014	17/10/2014
SW version	6.7 FS	8.3 FS	8.5 FS	8.8 FS
D	-3'000.0	-1'800.0	-1'000.0	-1'000.0
BP_OS	-12.5	-5.2	-18.5	-5.1
A1_OS	-760.0	-370.7	-318.0	-220.6
A2_OS	-2'400.0	-1'021.5	-918.7	-537.9
SL_OS	-4'310.0	-792.1	-1'671.2	-1'820.0
MCP_OS	2'700.0	2'700.0	2'700.0	2'700.0
Gr_OS	8.0	-4.9	-0.3	-4.3
P_OS	-262.0	-211.2	-90.6	-69.9
R1	-88.0	-52.2	-28.6	-15.6
R2	-1'123.0	-556.8	-382.1	-413.9
RL	-6'165.0	-878.5	-1'693.7	-1'633.2
E2	-8.7	-14.69	-14.69	-10.5
ELA	-6.0	-11.87	-11.87	-12.7
ELB	-5.3	-10.88	-10.88	-12.3
RepA_OS	-200.0	-200.0	-200.0	-200.0
RepB_OS	-200.0	-200.0	-200.0	-200.0
E1	0.0	0.0	0.0	0.0

Table A.2: RTOF FS settings – OS (ions). All voltages are given in V.

Date	20/04/2014	10/12/2014	11/05/2015
SW version	8.5 FS	8.8 FS	8.A FS
D	-1'000.0	-1'000.0	-1'000.0
BP_OS	-18.5	-5.1	2.5 / -4.4 / -6.9
A1_OS	-318.0	-220.6	-318.0
A2_OS	-918.7	-537.9	-918.7
SL_OS	-1'671.2	-1'820.0	-1'671.2
MCP_OS	2'700.0	2'700.0	'2750.0
Gr_OS	-0.3	-4.3	1.1 / -3.4 / -4.3
P_OS	-90.6	-69.8	-125.7 / -133.6 / -137.2
R1	-28.6	-15.6	-28.6
R2	-382.1	-413.9	-382.1
RL	-1'693.7	-1'633.2	-1747.4
E2	-49.5	-47.8	-49.0 / -48.5 / -37.9
ELA	-16.6	-12.2	-11.9 / -14.9 / -14.4
ELB	-16.2	-10.8	-13.6 / -13.6 / -13.5
RepA_OS	-200.0	-1.0	-1.0
RepB_OS	-200.0	-1.0	-1.0
E1	0.0	-13.3	0.0 / -7.7 / -5.0

Table A.3: RTOF FS settings – SS. All voltages are given in V.

Date	2003	29/03/2014	20/04/2014	02/09/2014	03/10/2014	08/04/2015	11/05/2015	05/06/2015
SW version	6.7 FS	8.3 FS	8.5 FS	8.8 FS	8.8 FS	8.9 FS	8.A FS	8.A FS
D	-3'000.0	-1'800.0	-1'000.0	-1'000.0	-1'000.0	-1'000.0	-1'000.0	-1'000.0
BP_SS	-13.5	-21.6	-24.0	-37.5	-33.4	14.3	-33.4	-40.0
A1_SS	-750.0	-331.2	-210.0	-210.0	-210.0	-210.0	-210.0	-210.0
A2_SS	-1'550.0	-995.1	-430.0	-700.0	-700.0	-700.0	-700.0	-700.0
SL_SS	-4'945.0	-798.0	-1'665.0	-1'715.0	-1'715.0	-1'715.0	-1'715.0	-1'715.0
MCP_SS	2'700.0	2'700.0	2'700.0	2'700.0	2'700.0	2'750.0	2'750.0	2'750.0
Gr_SS	18.0	-8.2	-8.0	-4.2	-0.15	48.0	-0.15	0.0
P_SS	-275.0	-246.1	-107.0	-87.7	-99.1	-127.1	-99.1	-90.0
R1	-93.0	-63.3	-54.8	-47.0	-53.7	-53.7	-53.7	-53.7
R2	-972.0	-555.7	-342.0	-376.5	-376.5	-376.5	-376.5	-376.5
RL	-5'335.0	-912.9	-1'710.0	-1'845.0	-1'825.0	-1'825.0	-1'825.0	-1'825.0
RepA_SS	-180.0	-180.0	-180.0	-180.0	-120.0	-120.0	-120.0	-120.0
RepB_SS	-180.0	-180.0	-180.0	-180.0	-120.0	-120.0	-120.0	-120.0

B. Tables of fragmentation and isotopic ratios

The ratios presented hereafter are given relative to the most abundant fragment; the most abundant isotope and the parent fragments are written in red. For each fragment, the chemical formula is a suggestion for the most abundant molecule to be found at the corresponding mass, but is in the facts a combination of many molecules, including isotopologues and doubly charged ions.

When not specified, C = ^{12}C , N = ^{14}N , and O = ^{16}O .

B.1 D = -3'000 V

Table B.1: Fragmentation ratios for CO_2 measured with the RTOF-OS in M513 with the FM and FS models.

Parent / Daughters	Mass	Fragmentation ratio (%)		
		FM-OS	FS-OS	NIST
C^+	11.9995	1.046 ± 0.007	0.884 ± 0.018	8.71
O^+	15.9944	3.961 ± 0.024	2.917 ± 0.051	9.61
CO_2^{++}	21.9944	0.884 ± 0.008	0.299 ± 0.006	1.90
CO^+	27.9944	3.744 ± 0.031	3.590 ± 0.070	9.81
$^{13}\text{CO}^+$	28.9977	0.085 ± 0.018	0.090 ± 0.014	0.10
$^{13}\text{CO}_2^+$	44.9926	1.233 ± 0.050	1.600 ± 0.051	1.20
CO_2^+	43.9893	100.00 ± 0.15	100.00 ± 0.15	100.00
C^{18}OO^+	46.0049	0.411 ± 0.021	0.389 ± 0.024	0.40

Table B.2: Isotopic ratios for krypton measured with the RTOF-OS in M513 with the FM and FS models.

Isotopes	Mass	Isotopic ratio (%)		
		FM-OS	FS-OS	NIST
$^{78}\text{Kr}^{++}$	38.9597	0.074 ± 0.001	0.047 ± 0.004	\emptyset
$^{80}\text{Kr}^{++}$	39.9576	0.497 ± 0.002	0.299 ± 0.002	\emptyset
$^{82}\text{Kr}^{++}$	40.9562	2.458 ± 0.006	1.534 ± 0.006	3.47
$^{83}\text{Kr}^{++}$	41.4565	2.440 ± 0.009	1.572 ± 0.012	\emptyset
$^{84}\text{Kr}^{++}$	41.9552	11.853 ± 0.019	7.486 ± 0.050	15.90
$^{86}\text{Kr}^{++}$	42.9548	3.758 ± 0.014	2.428 ± 0.017	4.98
$^{78}\text{Kr}^+$	77.9198	0.679 ± 0.003	0.687 ± 0.003	\emptyset
$^{80}\text{Kr}^+$	79.9158	4.245 ± 0.082	4.306 ± 0.021	4.29
$^{82}\text{Kr}^+$	81.9129	20.648 ± 0.289	20.559 ± 0.005	20.60
$^{83}\text{Kr}^+$	82.9136	20.532 ± 0.235	20.515 ± 0.001	20.50
$^{84}\text{Kr}^+$	83.9109	100.00 ± 1.02	100.00 ± 1.10	100.00
$^{86}\text{Kr}^+$	85.9101	30.694 ± 0.117	30.750 ± 0.000	30.60

B.2 $D = -1'800 \text{ V}$

 Table B.3: Isotopic ratios for the noble gases He, Ne, Ar, Kr, and Xe for FM with $D = -1'800 \text{ V}$.

Isotopes	Mass	Isotopic ratio (%)		
		FM-SS	FM-OS	NIST
$^4\text{He}^+$	4.0021	100.0	100.0	100.0
$^{20}\text{Ne}^+$	19.9919	100.0 ± 1.7	100.0 ± 1.3	100.00
$^{21}\text{Ne}^+$	20.9933	0.34 ± 0.08	0.27 ± 0.06	0.30
$^{22}\text{Ne}^+$	21.9908	10.94 ± 0.88	10.72 ± 1.02	10.22
$^{40}\text{Ar}^{++}$	19.9806	1.13 ± 0.02	6.58 ± 0.08	14.62
$^{36}\text{Ar}^+$	35.9670	0.26 ± 0.06	0.31 ± 0.03	0.30
$^{38}\text{Ar}^+$	37.9622	0.05 ± 0.02	0.05 ± 0.01	0.05
$^{40}\text{Ar}^+$	39.9618	100.0 ± 2.5	100.0 ± 1.6	100.00
$^{78}\text{Kr}^{++}$	38.9596	< 0.03	< 0.07	\emptyset
$^{80}\text{Kr}^{++}$	39.9576	0.20 ± 0.17	0.45 ± 0.03	\emptyset
$^{82}\text{Kr}^{++}$	40.9562	0.89 ± 0.10	1.89 ± 0.05	3.47
$^{83}\text{Kr}^{++}$	41.4565	1.01 ± 0.42	1.76 ± 0.12	\emptyset
$^{84}\text{Kr}^{++}$	41.9552	4.12 ± 0.19	9.28 ± 0.55	15.90
$^{86}\text{Kr}^{++}$	42.9548	1.39 ± 0.12	2.99 ± 0.12	4.98
$^{78}\text{Kr}^+$	77.9198	0.61 ± 0.11	0.77 ± 0.12	\emptyset
$^{80}\text{Kr}^+$	79.9158	4.20 ± 0.20	4.10 ± 0.20	4.29
$^{82}\text{Kr}^+$	81.9129	20.70 ± 0.47	20.62 ± 0.61	20.60
$^{83}\text{Kr}^+$	82.9136	20.77 ± 0.57	20.50 ± 0.60	20.50
$^{84}\text{Kr}^+$	83.9109	100.0 ± 2.1	100.0 ± 2.0	100.00
$^{86}\text{Kr}^+$	85.9100	30.64 ± 0.86	30.57 ± 0.52	30.60
$^{128}\text{Xe}^{++}$	63.9512	0.69 ± 0.29	0.87 ± 0.21	\emptyset
$^{129}\text{Xe}^{++}$	64.4518	8.63 ± 1.38	12.77 ± 0.50	\emptyset
$^{130}\text{Xe}^{++}$	64.9512	1.37 ± 0.24	1.82 ± 0.06	2.93
$^{131}\text{Xe}^{++}$	65.4520	6.90 ± 0.99	10.23 ± 0.15	\emptyset
$^{132}\text{Xe}^{++}$	65.9515	8.79 ± 0.71	12.98 ± 1.17	17.76
$^{134}\text{Xe}^{++}$	66.9521	3.35 ± 0.49	5.05 ± 0.11	6.90
$^{136}\text{Xe}^{++}$	67.9531	2.75 ± 0.48	4.19 ± 0.15	6.05
$^{124}\text{Xe}^+$	123.9053	0.40 ± 0.09	0.31 ± 0.12	0.35
$^{126}\text{Xe}^+$	125.9037	0.36 ± 0.06	0.26 ± 0.11	0.34
$^{128}\text{Xe}^+$	127.9030	7.44 ± 0.61	7.28 ± 0.40	7.05
$^{129}\text{Xe}^+$	128.9042	95.78 ± 3.81	99.17 ± 2.49	98.41
$^{130}\text{Xe}^+$	129.9030	16.21 ± 1.12	15.49 ± 0.46	15.20
$^{131}\text{Xe}^+$	130.9045	78.70 ± 2.60	77.15 ± 2.44	79.40
$^{132}\text{Xe}^+$	131.9036	100.0 ± 2.2	100.0 ± 2.4	100.00
$^{134}\text{Xe}^+$	133.9048	38.64 ± 1.79	38.62 ± 1.04	37.83
$^{136}\text{Xe}^+$	135.9067	32.86 ± 2.03	32.09 ± 1.28	31.97

Table B.4: Fragmentation and isotopologic ratios for H₂O, CO, and CO₂, for FM with D = -1'800 V.

Parent / Daughters	Mass	Fragmentation ratio (%)		NIST
		FM-SS	FM-OS	
O ⁺	15.9944	3.18 ± 0.46	1.39 ± 0.12	0.90
OH ⁺	17.0022	24.55 ± 1.56	22.23 ± 0.88	21.22
H₂O⁺	18.0100	100.0 ± 2.0	100.0 ± 1.8	100.00
HDO	19.0163	0.47 ± 0.11	0.48 ± 0.03	0.50
H ₂ ¹⁸ O ⁺	20.0143	0.28 ± 0.04	0.31 ± 0.02	0.30
C ⁺	11.9995	3.76 ± 0.03	0.60 ± 0.10	4.70
O ⁺	15.9944	1.35 ± 0.03	0.18 ± 0.05	1.70
CO⁺	27.9944	100.0 ± 1.5	100.0 ± 1.3	100.00
¹³ CO ⁺	28.9977	1.26 ± 0.11	1.27 ± 0.10	1.20
C ⁺	11.9995	3.16 ± 0.38	0.87 ± 0.02	8.71
O ⁺	15.9944	8.04 ± 0.56	3.77 ± 0.08	9.61
CO ₂ ⁺⁺	21.9944	0.17 ± 0.12	0.55 ± 0.02	1.90
CO ⁺	27.9944	20.45 ± 1.60	12.84 ± 0.25	9.81
¹³ CO ⁺	28.9977	0.13 ± 0.11	0.07 ± 0.10	0.10
CO₂⁺	43.9893	100.0 ± 1.7	100.0 ± 1.3	100.00
¹³ CO ₂ ⁺	44.9926	1.18 ± 0.31	0.34 ± 1.20	1.20
C ¹⁸ OO ⁺	46.0049	0.42 ± 0.17	0.12 ± 0.40	0.40

 Table B.5: Fragmentation and isotopologic ratios for CH₄, for FM with D = -1'800 V.

Parent / Daughters	Mass	Fragmentation ratio (%)		NIST
		FM-SS	FM-OS	
H ₂ ⁺	2.0151	4.05 ± 0.38	5.08 ± 0.09	∅
C ⁺	11.9995	1.83 ± 0.16	0.73 ± 0.02	3.80
CH ⁺	13.0073	7.12 ± 0.46	3.04 ± 0.13	10.69
CH ₂ ⁺	14.0151	15.62 ± 0.34	9.49 ± 0.09	20.42
CH ₃ ⁺	15.0229	78.97 ± 1.78	72.56 ± 0.61	88.80
CH₄⁺	16.0308	100.0 ± 0.6	100.0 ± 0.7	100.00
¹³ CH ₄ ⁺ / CH ₃ D ⁺	17.0370	1.61 ± 0.13	1.43 ± 0.03	1.64

Table B.6: Fragmentation and isotopologic ratios for C_2H_6 , for FM with $D = -1'800$ V.

Parent / Daughters	Mass	Fragmentation ratio (%)		
		FM-SS	FM-OS	NIST
H_2^+	2.0151	5.69 ± 0.17	4.15 ± 0.03	0.20
C^+	11.9995	0.38 ± 0.07	0.11 ± 0.01	0.40
$CH^+/C_2H_2^{++}$	13.0073	0.68 ± 0.03	0.25 ± 0.01	1.00
$CH_2^+/C_2H_4^{++}$	14.0151	2.01 ± 0.16	1.05 ± 0.03	3.00
$CH_3^+/C_2H_6^{++}$	15.0229	4.00 ± 0.13	2.24 ± 0.02	4.40
CH_4^+	16.0308	1.10 ± 0.09	0.80 ± 0.03	0.10
C_2^+	23.9995	0.49 ± 0.04	0.50 ± 0.03	0.50
C_2H^+	25.0073	3.51 ± 0.37	3.08 ± 0.04	3.50
$C_2H_2^+$	26.0151	24.51 ± 1.00	19.35 ± 0.14	23.22
$C_2H_3^+$	27.0229	32.88 ± 0.93	27.18 ± 0.11	33.23
$C_2H_4^+$	28.0308	100.0 ± 1.63	100.0 ± 0.40	99.99
$C_2H_5^+$	29.0386	19.96 ± 0.43	24.97 ± 0.16	21.52
$C_2H_6^+$	30.0464	26.04 ± 1.14	31.72 ± 0.14	26.22
$^{13}CH_6^+ / CH_5D^+$	31.0542	0.66 ± 0.02	0.74 ± 0.02	0.50

 Table B.7: Fragmentation and isotopologic ratios for C_3H_8 , for FM with $D = -1'800$ V.

Parent / Daughters	Mass	Fragmentation ratio (%)		
		FM-SS	FM-OS	NIST
H_2^+	2.0151	11.50 ± 0.90	9.57 ± 0.13	\emptyset
C^+	11.9995	0.23 ± 0.15	0.08 ± 0.02	0.30
CH^+	13.0073	0.59 ± 0.11	0.30 ± 0.01	0.60
CH_2^+	14.0151	1.78 ± 0.17	0.78 ± 0.03	2.20
CH_3^+	15.0229	7.12 ± 0.57	3.52 ± 0.03	7.21
CH_4^+	16.0308	2.70 ± 0.29	2.69 ± 0.12	0.40
C_2^+	23.9995	0.23 ± 0.16	0.30 ± 0.02	0.10
C_2H^+	25.0073	1.74 ± 0.16	1.67 ± 0.05	0.50
$C_2H_2^+$	26.0151	16.24 ± 0.53	12.19 ± 0.11	9.11
$C_2H_3^+$	27.0229	46.39 ± 1.03	32.79 ± 0.13	41.94
$C_2H_4^+$	28.0308	69.31 ± 1.59	68.12 ± 0.29	58.76
$C_2H_5^+$	29.0386	100.0 ± 1.1	100.0 ± 0.5	100.00
$C_2H_6^+$	30.0464	2.20 ± 0.40	2.44 ± 0.02	2.20
C_3H^+	37.0073	3.06 ± 0.45	3.20 ± 0.03	3.00
$C_3H_2^+$	38.0151	6.19 ± 0.62	5.45 ± 0.08	5.30
$C_3H_3^+$	39.0229	24.68 ± 0.74	18.45 ± 0.17	18.92
$C_3H_4^+$	40.0308	3.87 ± 0.14	3.49 ± 0.14	2.80
$C_3H_5^+$	41.0386	17.16 ± 0.42	18.83 ± 0.25	13.41
$C_3H_6^+$	42.0464	6.27 ± 0.27	6.68 ± 0.11	6.01
$C_3H_7^+$	43.0542	30.68 ± 1.10	42.07 ± 0.50	23.12
$C_3H_8^+$	44.0621	38.59 ± 0.94	53.88 ± 1.37	27.42
$^{13}CC_2H_8^+ / C_3H_7D^+$	45.0654	1.18 ± 0.35	1.71 ± 0.06	0.90

Table B.8: Fragmentation and isotopologic ratios for C_4H_{10} , for FM with $D = -1'800$ V.

Parent / Daughters	Mass	Fragmentation ratio (%)		
		FM-SS	FM-OS	NIST
H_2^+	2.0151	12.59 ± 0.48	7.96 ± 0.12	\emptyset
C^+	11.9995	0.43 ± 0.11	0.06 ± 0.01	0.10
CH^+	13.0073	0.43 ± 0.21	0.20 ± 0.02	0.20
CH_2^+	14.0151	1.48 ± 0.15	0.62 ± 0.01	0.80
CH_3^+	15.0229	5.55 ± 0.64	1.88 ± 0.03	6.01
CH_4^+	16.0308	0.13 ± 0.04	0.16 ± 0.01	0.10
C_2^+	23.9995	0.39 ± 0.16	0.32 ± 0.02	0.10
C_2H^+	25.0073	1.87 ± 0.28	1.56 ± 0.02	0.20
$C_2H_2^+$	26.0151	14.23 ± 0.87	10.15 ± 0.07	5.81
$C_2H_3^+$	27.0229	40.51 ± 1.04	22.32 ± 0.11	38.73
$C_2H_4^+$	28.0308	48.25 ± 4.35	46.32 ± 0.98	32.13
$C_2H_5^+$	29.0386	45.81 ± 3.31	31.09 ± 0.19	43.34
$C_2H_6^+$	30.0464	2.42 ± 0.66	1.17 ± 0.01	1.00
C_3H^+	37.0073	0.83 ± 0.28	0.68 ± 0.01	0.70
$C_3H_2^+$	38.0151	2.33 ± 0.29	1.36 ± 0.01	1.90
$C_3H_3^+$	39.0229	18.53 ± 1.17	8.86 ± 0.08	13.61
$C_3H_4^+$	40.0308	2.81 ± 0.25	1.91 ± 0.15	1.90
$C_3H_5^+$	41.0386	36.03 ± 0.44	28.11 ± 0.12	28.53
$C_3H_6^+$	42.0464	15.53 ± 0.98	15.59 ± 0.09	12.11
$C_3H_7^+$	43.0542	100.0 ± 0.5	100.0 ± 0.4	100.00
$C_3H_8^+$	44.0621	5.68 ± 0.87	4.43 ± 0.13	3.30
$^{13}CC_2H_8^+/C_3H_7D^+$	45.0654	1.63 ± 0.91	0.14 ± 0.01	0.10
C_4H^+	49.0073	0.59 ± 0.57	0.47 ± 0.02	0.20
$C_4H_2^+$	50.0151	1.69 ± 0.30	1.65 ± 0.03	1.10
$C_4H_3^+$	51.0229	1.42 ± 0.14	1.16 ± 0.01	1.00
$C_4H_4^+$	52.0308	0.41 ± 0.19	0.32 ± 0.01	0.30
$C_4H_5^+$	53.0386	1.13 ± 0.13	0.87 ± 0.01	0.90
$C_4H_6^+$	54.0464	0.34 ± 0.03	0.21 ± 0.02	0.20
$C_4H_7^+$	55.0542	1.23 ± 0.24	1.17 ± 0.01	1.00
$C_4H_8^+$	56.0621	1.02 ± 0.27	0.89 ± 0.03	0.80
$C_4H_9^+$	57.0699	2.98 ± 0.15	3.07 ± 0.06	2.50
$C_4H_{10}^+$	58.0777	19.79 ± 0.46	22.12 ± 0.37	12.21
$^{13}CC_3H_{10}^+/C_4H_9D^+$	59.0811	0.88 ± 0.24	1.09 ± 0.02	0.50

 Table B.9: Fragmentation and isotopologic ratios for C_2H_2 , for FM with $D = -1'800$ V.

Parent / Daughters	Mass	Fragmentation ratio (%)		
		FM-SS	FM-OS	NIST
H_2^+	2.0151	4.24 ± 1.46	1.22 ± 0.01	\emptyset
C^+	11.9995	1.62 ± 0.15	0.55 ± 0.01	0.70
CH^+	13.0073	3.31 ± 0.44	1.87 ± 0.02	3.20
CH_2^+	14.0151	0.54 ± 0.19	0.26 ± 0.01	0.10
C_2^+	23.9995	6.25 ± 0.40	5.53 ± 0.03	5.00
C_2H^+	25.0073	22.18 ± 0.89	20.74 ± 0.08	19.12
$C_2H_2^+$	26.0151	100.0 ± 8.1	100.0 ± 0.5	100.00
m_{27}	≈ 27	2.56 ± 0.30	2.41 ± 0.01	\emptyset
m_{28}	≈ 28	3.86 ± 2.81	2.50 ± 0.04	2.20

Table B.10: Fragmentation and isotopologic ratios for C_6H_6 , for FM with $D = -1'800$ V.

Parent / Daughters	Mass	Fragmentation ratio (%)		
		FM-SS	FM-OS	NIST
H_2^+	2.0151	6.28 ± 0.77	2.52 ± 0.21	\emptyset
C^+	11.9995	0.26 ± 0.10	0.06 ± 0.01	\emptyset
CH^+	13.0073	0.44 ± 0.14	0.15 ± 0.02	\emptyset
CH_2^+	14.0151	0.53 ± 0.07	0.18 ± 0.02	\emptyset
CH_3^+	15.0229	1.72 ± 0.49	0.45 ± 0.04	1.22
CH_4^+	16.0308	1.67 ± 0.36	0.47 ± 0.07	\emptyset
$^{13}CH_4^+/CH_3^+D$	17.0341	2.20 ± 0.38	0.53 ± 0.10	\emptyset
C_2^+	23.9995	0.40 ± 0.14	0.29 ± 0.03	\emptyset
C_2H^+	25.0073	2.04 ± 0.21	1.19 ± 0.10	0.70
$C_2H_2^+$	26.0151	10.85 ± 0.32	6.94 ± 0.60	3.45
$C_2H_3^+$	27.0229	6.28 ± 1.24	2.26 ± 0.19	2.62
$C_2H_4^+$	28.0308	4.19 ± 0.90	2.14 ± 0.18	2.10
$C_2H_5^+$	29.0386	2.56 ± 0.51	0.97 ± 0.08	\emptyset
$C_2H_6^+$	30.0464	0.68 ± 0.24	0.40 ± 0.04	\emptyset
$C_2H_7^+$	31.0542	9.05 ± 1.84	4.87 ± 0.43	\emptyset
C_3^+	35.9995	1.02 ± 1.58	0.21 ± 0.02	0.66
C_3H^+	37.0073	2.12 ± 0.43	1.77 ± 0.15	4.29
$C_6H_3^{++}$	37.5112	4.51 ± 4.53	0.47 ± 0.06	\emptyset
$C_6H_5^{++}$	38.5190	15.67 ± 3.58	13.01 ± 2.82	\emptyset
$C_3H_3^+$	39.0229	14.83 ± 2.81	8.96 ± 1.05	11.19
$^{13}CC_5H_6^+/C_6H_5D^{++}$	39.5246	6.63 ± 3.53	6.70 ± 3.62	\emptyset
$C_3H_4^+$	40.0308	0.42 ± 0.21	0.40 ± 0.05	0.70
$C_3H_5^+$	41.0386	0.35 ± 0.36	0.15 ± 0.04	\emptyset
$C_3H_6^+$	42.0464	0.37 ± 0.15	0.32 ± 0.08	\emptyset
$C_3H_7^+$	43.0542	0.90 ± 0.14	0.76 ± 0.10	\emptyset
$C_3H_8^+$	44.0621	0.57 ± 0.25	1.48 ± 0.55	\emptyset
C_4^+	47.9995	5.37 ± 8.10	0.22 ± 0.03	0.47
C_4H^+	49.0073	2.98 ± 0.41	2.06 ± 0.25	3.92
$C_4H_2^+$	50.0151	23.05 ± 1.07	14.94 ± 1.74	20.82
$C_4H_3^+$	51.0229	25.48 ± 1.29	17.72 ± 2.06	22.11
$C_4H_4^+$	52.0308	19.48 ± 1.47	19.00 ± 2.19	18.84
$C_4H_5^+$	53.0386	0.79 ± 0.18	0.91 ± 0.10	0.77
$C_4H_6^+$	54.0464	8.43 ± 9.16	0.60 ± 0.13	\emptyset
$C_4H_7^+$	55.0542	0.54 ± 0.47	0.07 ± 0.02	\emptyset
$C_4H_8^+$	56.0621	0.47 ± 0.41	0.06 ± 0.02	\emptyset
C_5^+	59.9995	0.31 ± 0.33	0.20 ± 0.03	\emptyset
C_5H^+	61.0073	0.39 ± 0.20	0.39 ± 0.05	1.02
$C_5H_2^+$	62.0151	0.87 ± 0.27	0.60 ± 0.07	1.10
$C_5H_3^+$	63.0229	4.43 ± 0.68	2.17 ± 0.27	4.97
$C_5H_4^+$	64.0308	0.68 ± 0.76	0.18 ± 0.02	\emptyset
C_6^+	71.9995	1.29 ± 1.48	0.11 ± 0.02	\emptyset
C_6H^+	73.0073	1.02 ± 0.53	1.00 ± 0.09	2.46
$C_6H_2^+$	74.0151	4.02 ± 2.51	2.84 ± 0.28	6.22
$C_6H_3^+$	75.0229	1.75 ± 0.45	2.51 ± 0.59	2.25
$C_6H_4^+$	76.0308	3.60 ± 1.14	5.17 ± 1.34	5.89
$C_6H_5^+$	77.0386	15.41 ± 12.3	25.36 ± 4.30	28.37
$C_6H_6^+$	78.0464	100.0 ± 13.5	100.0 ± 12.4	100.00
$^{13}CC_5H_6^+/C_6H_5D^+$	79.0498	5.54 ± 2.65	6.27 ± 1.36	6.53

Table B.11: Fragmentation and isotopologic ratios for $C_{10}H_8$, for FM with $D = -1'800$ V.

Parent / Daughters	Mass	Fragmentation ratio (%)		
		FM-SS	FM-OS	NIST
H_2^+	2.0151	19.18 ± 4.34	\emptyset	\emptyset
C^+	11.9995	4.06 ± 0.83	\emptyset	\emptyset
CH^+	13.0073	4.80 ± 0.99	\emptyset	\emptyset
C_2^+	23.9995	1.09 ± 0.27	\emptyset	\emptyset
C_2H^+	25.0073	3.96 ± 0.98	\emptyset	\emptyset
$C_2H_2^+$	26.0151	18.31 ± 4.52	\emptyset	0.10
$C_2H_3^+$	27.0229	9.18 ± 2.03	\emptyset	0.30
$C_2H_4^+$	28.0308	5.04 ± 2.69	\emptyset	0.10
C_3^+	35.9995	0.23 ± 0.06	\emptyset	\emptyset
C_3H^+	37.0073	0.59 ± 0.16	\emptyset	0.30
$C_3H_2^+$	38.0151	1.29 ± 0.32	\emptyset	0.50
$C_3H_3^+$	39.0229	5.99 ± 1.65	\emptyset	1.39
C_4H^+	49.0073	1.07 ± 0.33	\emptyset	0.20
$C_4H_2^+$	50.0151	8.20 ± 2.31	\emptyset	2.79
$C_4H_3^+$	51.0229	12.82 ± 3.71	\emptyset	7.19
$C_4H_4^+$	52.0308	2.46 ± 0.69	\emptyset	0.80
$C_4H_5^+$	53.0386	0.76 ± 0.18	\emptyset	0.10
C_5H^+	61.0073	0.72 ± 0.22	\emptyset	0.70
$C_5H_2^+$	62.0151	2.74 ± 0.76	\emptyset	1.29
$C_5H_3^+/C_{10}H_6^{++}$	63.0229	9.27 ± 2.65	\emptyset	4.59
$C_{10}H_7^{++}$	63.5268	18.24 ± 5.39	\emptyset	\emptyset
$C_5H_4^+/C_{10}H_8^{++}$	64.0308	10.18 ± 2.92	\emptyset	6.79
$^{13}CC_9H_8^+/C_{10}H_7D^+$	64.5327	7.20 ± 2.21	\emptyset	\emptyset
$C_5H_5^+$	65.0386	1.34 ± 0.41	\emptyset	0.10
C_6H^+	73.0073	0.85 ± 0.26	\emptyset	0.20
$C_6H_2^+$	74.0151	6.08 ± 1.73	\emptyset	2.69
$C_6H_3^+$	75.0229	6.96 ± 1.98	\emptyset	3.19
$C_6H_4^+$	76.0308	5.13 ± 1.46	\emptyset	2.39
$C_6H_5^+$	77.0386	5.81 ± 1.65	\emptyset	3.39
$C_6H_6^+$	78.0464	3.74 ± 1.04	\emptyset	2.29
$C_6H_7^+$	79.0542	0.92 ± 0.28	\emptyset	0.10
C_7H^+	85.0073	0.77 ± 0.24	\emptyset	0.20
$C_7H_2^+$	86.0151	2.05 ± 0.56	\emptyset	0.50
$C_7H_3^+$	87.0229	2.04 ± 0.55	\emptyset	0.80
$C_7H_4^+$	88.0308	0.67 ± 0.20	\emptyset	0.10
$C_7H_5^+$	89.0386	1.49 ± 0.46	\emptyset	0.50
C_8H^+	97.0073	1.03 ± 0.32	\emptyset	0.10
$C_8H_2^+$	98.0151	1.81 ± 0.47	\emptyset	0.70
$C_8H_3^+$	99.0229	1.39 ± 0.43	\emptyset	0.40
$C_8H_4^+$	100.0308	1.80 ± 0.55	\emptyset	0.40
$C_8H_5^+$	101.0386	4.10 ± 1.12	\emptyset	2.09
$C_8H_6^+$	102.0464	9.88 ± 2.83	\emptyset	6.09
$C_8H_7^+$	103.0542	1.90 ± 0.58	\emptyset	0.60
$C_9H_5^+$	113.0386	0.50 ± 0.15	\emptyset	0.10
$C_{10}H_5^+$	125.0386	2.30 ± 0.71	\emptyset	0.30
$C_{10}H_6^+$	126.0464	8.47 ± 4.19	\emptyset	5.19
$C_{10}H_7^+$	127.0542	14.06 ± 6.15	\emptyset	10.79
$C_{10}H_8^+$	128.0621	100.0 ± 8.9	\emptyset	100.00
$^{13}CC_9H_8^+/C_{10}H_7D^+$	129.0654	10.03 ± 0.57	\emptyset	10.99

Table B.12: Fragmentation and isotopologic ratios for CH_3OH , for FM with $D = -1'800$ V.

Parent / Daughters	Mass	Fragmentation ratio (%)		
		FM-SS	FM-OS	NIST
H_2^+	2.0151	11.77 ± 0.74	8.49 ± 0.18	0.30
C^+	11.9995	1.87 ± 0.21	0.47 ± 0.01	0.20
CH^+	13.0073	2.46 ± 0.23	0.71 ± 0.01	0.60
CH_2^+	14.0151	6.28 ± 0.39	2.44 ± 0.03	1.69
CH_3^+	15.0229	31.10 ± 0.41	12.62 ± 0.23	12.39
O^+	15.9944	3.11 ± 0.16	2.03 ± 0.06	0.10
OH^+	17.0022	2.50 ± 0.13	0.80 ± 0.03	0.30
H_2O^+	18.0100	6.48 ± 0.92	2.97 ± 0.11	0.70
CO^+	27.9944	31.11 ± 0.87	30.16 ± 0.74	4.59
CHO^+	29.0022	73.94 ± 0.96	49.46 ± 0.87	44.59
CH_2O^+	30.0100	13.85 ± 0.57	11.82 ± 0.21	6.49
CH_3O^+	31.0178	100.0 ± 1.5	100.0 ± 1.7	100.00
CH_4O^+	32.0257	70.50 ± 0.41	77.44 ± 1.25	74.40
$^{13}\text{CH}_4\text{O}^+/\text{CH}_3\text{DO}^+$	33.0290	1.18 ± 0.04	1.24 ± 0.02	1.19
$\text{CH}_4^{18}\text{O}^+$	34.0305	0.18 ± 0.02	\emptyset	0.10

 Table B.13: Fragmentation and isotopologic ratios for $\text{C}_2\text{H}_5\text{OH}$, for FM with $D = -1'800$ V.

Parent / Daughters	Mass	Fragmentation ratio (%)		
		FM-SS	FM-OS	NIST
H_2^+	2.0151	11.71 ± 0.79	10.24 ± 0.11	\emptyset
C^+	11.9995	1.34 ± 0.16	0.46 ± 0.01	0.20
CH^+	13.0073	1.80 ± 0.10	1.02 ± 0.03	1.39
CH_2^+	14.0151	5.73 ± 0.34	3.28 ± 0.06	1.45
CH_3^+	15.0229	13.39 ± 0.41	8.28 ± 0.10	6.64
OH^+	17.0022	4.80 ± 0.70	3.33 ± 0.03	0.70
H_2O^+	18.0100	17.95 ± 2.79	13.77 ± 0.53	0.55
m_{19}	≈ 19	1.87 ± 0.79	3.46 ± 0.03	2.79
C_2^+	23.9995	0.72 ± 0.03	0.54 ± 0.04	0.61
C_2H^+	25.0073	3.16 ± 0.25	2.87 ± 0.05	2.46
C_2H_2^+	26.0151	17.48 ± 0.35	15.52 ± 0.19	9.85
C_2H_3^+	27.0229	25.80 ± 0.70	19.85 ± 0.17	22.41
$\text{CO}^+/\text{C}_2\text{H}_4^+$	28.0126	31.30 ± 1.78	38.10 ± 0.30	3.45
$\text{COH}^+/\text{C}_2\text{H}_5^+$	29.0203	34.15 ± 0.75	23.91 ± 0.29	29.85
CH_2O^+	30.0100	7.73 ± 0.41	7.19 ± 0.06	8.12
CH_3O^+	31.0178	100.0 ± 3.0	100.0 ± 0.9	100.00
CH_5O^+	33.0335	0.27 ± 0.02	\emptyset	0.31
C_2HO^+	41.0022	2.36 ± 0.20	1.95 ± 0.02	1.37
$\text{C}_2\text{H}_2\text{O}^+$	42.0100	5.69 ± 0.26	5.23 ± 0.09	4.74
$\text{C}_2\text{H}_3\text{O}^+$	43.0178	25.45 ± 0.99	29.49 ± 0.20	11.44
$\text{C}_2\text{H}_4\text{O}^+$	44.0257	7.21 ± 0.65	8.03 ± 0.15	0.71
$\text{C}_2\text{H}_5\text{O}^+$	45.0335	37.85 ± 1.34	55.19 ± 0.61	51.50
$\text{C}_2\text{H}_6\text{O}^+$	46.0413	21.73 ± 0.90	35.00 ± 0.38	21.63
$\text{C}_2\text{H}_7\text{O}^+$	47.0491	0.73 ± 0.01	0.97 ± 0.01	0.73

Table B.14: Fragmentation and isotopologic ratios for HCOOH, for FM with $D = -1'800$ V.

Parent / Daughters	Mass	Fragmentation ratio (%)		
		FM-SS	FM-OS	NIST
H_2^+	2.0151	10.72 ± 0.73	13.10 ± 1.76	\emptyset
C^+	11.9995	4.31 ± 0.60	1.45 ± 0.06	3.30
CH^+	13.0073	1.47 ± 0.17	0.57 ± 0.02	2.90
CH_2^+	14.0151	0.47 ± 0.21	0.72 ± 0.03	0.40
O^+/CH_4^+	16.0126	7.65 ± 0.44	5.04 ± 0.10	5.20
OH^+	17.0022	21.25 ± 1.67	20.04 ± 1.84	17.12
CO^+	27.9944	73.87 ± 2.34	108.1 ± 3.6	17.22
HCO^+	29.0022	100.0 ± 1.9	100.0 ± 1.4	100.00
$HCOH^+$	30.0100	3.48 ± 0.16	1.30 ± 0.04	1.70
$H^{13}COH^+/HCOOD^+$	31.0134	0.83 ± 0.13	4.12 ± 0.06	0.60
O_2^+	31.9893	1.90 ± 0.12	2.53 ± 0.03	0.20
COO^+	43.9893	48.65 ± 2.67	81.56 ± 3.51	10.01
$HCOO^+$	44.9971	50.54 ± 0.80	92.00 ± 2.82	47.64
HCOOH⁺	46.0049	64.02 ± 2.28	112.5 ± 3.4	60.96
$H^{13}COOH^+/HCOOD^+$	47.0083	1.24 ± 0.04	2.04 ± 0.06	1.00
$HC^{18}OOH^+$	48.0092	0.40 ± 0.01	0.68 ± 0.03	0.30

Table B.15: Fragmentation and isotopologic ratios for CH_3COOH , for FM with $D = -1'800 \text{ V}$.

Parent / Daughters	Mass	Fragmentation ratio (%)		
		FM-SS	FM-OS	NIST
H_2^+	2.0151	12.69 ± 0.74	11.39 ± 0.12	0.20
C^+	11.9995	4.78 ± 0.56	1.94 ± 0.04	0.60
CH^+	13.0073	6.22 ± 0.72	3.60 ± 0.09	2.09
CH_2^+	14.0151	17.80 ± 0.66	10.68 ± 0.11	4.89
CH_3^+	15.0229	44.94 ± 2.25	32.73 ± 0.20	17.09
O^+	15.9944	15.65 ± 1.22	14.25 ± 0.13	2.39
OH^+	17.0022	6.91 ± 0.68	4.66 ± 0.13	0.99
H_2O^+	18.0100	21.38 ± 3.03	18.05 ± 0.41	2.79
C_2^+	23.9995	0.71 ± 0.07	0.73 ± 0.03	0.20
C_2H^+	25.0073	2.67 ± 0.23	2.45 ± 0.01	0.40
C_2H_2^+	26.0151	8.74 ± 0.60	11.09 ± 0.18	0.50
C_2H_3^+	27.0229	1.70 ± 0.17	1.60 ± 0.04	0.10
CO^+	27.9944	65.94 ± 3.72	87.78 ± 0.67	4.09
CHO^+	29.0022	21.00 ± 0.61	14.44 ± 0.20	8.49
CH_2O^+	30.0100	2.80 ± 0.30	3.13 ± 0.05	0.40
CH_3O^+	31.0178	8.22 ± 0.24	5.43 ± 0.09	2.49
CH_4O^+	32.0257	2.53 ± 0.25	3.03 ± 0.02	0.10
C_2O^+	39.9944	1.92 ± 0.14	2.10 ± 0.06	0.80
C_2HO^+	41.0022	6.09 ± 0.25	5.36 ± 0.04	3.59
$\text{C}_2\text{H}_2\text{O}^+$	42.0100	22.01 ± 0.78	18.54 ± 0.14	13.09
$\text{C}_2\text{H}_3\text{O}^+$	43.0178	100.0 ± 1.8	100.0 ± 0.5	100.00
$\text{CO}_2^+/\text{C}_2\text{H}_4\text{O}^+$	44.0075	35.31 ± 2.40	48.58 ± 0.28	2.49
COOH^+	44.9971	92.03 ± 1.83	101.1 ± 0.6	90.40
$^{13}\text{COOH}^+/\text{COOD}^+$	46.0005	1.71 ± 0.13	1.70 ± 0.02	1.09
$\text{C}^{18}\text{OOH}^+$	47.0014	0.56 ± 0.03	0.64 ± 0.06	0.20
C_2OOH^+	56.9971	0.11 ± 0.01	0.16 ± 0.09	0.20
$\text{C}_2\text{H}_4\text{O}_2^+$	60.0206	53.90 ± 1.07	95.98 ± 0.59	74.80
$^{13}\text{CCH}_4\text{O}_2^+/\text{C}_2\text{H}_3\text{DO}_2^+$	61.0239	1.52 ± 0.10	2.45 ± 0.12	1.99
$\text{C}_2\text{H}_4^{18}\text{OO}^+$	62.0248	0.34 ± 0.01	0.48 ± 0.05	0.20

Table B.16: Fragmentation and isotopologic ratios for H_2CO , for FM with $D = -1'800$ V.

Parent / Daughters	Mass	Fragmentation ratio (%)		
		FM-SS	FM-OS	NIST
H_2^+	2.0151	5.39 ± 0.26	3.05 ± 0.06	\emptyset
C^+	11.9995	2.72 ± 0.42	0.80 ± 0.01	1.00
CH^+	13.0073	2.91 ± 0.23	0.70 ± 0.02	1.00
CH_2^+	14.0151	3.67 ± 0.33	0.89 ± 0.02	1.00
CH_3^+	15.0229	0.83 ± 0.05	0.47 ± 0.01	2.00
CO^+	27.9944	47.07 ± 0.68	45.08 ± 0.29	24.00
HCO^+	29.0022	100.0 ± 1.8	100.0 ± 0.3	100.00
H_2CO^+	30.0100	76.45 ± 2.21	87.87 ± 0.28	58.01
$\text{H}_2^{13}\text{CO}^+/\text{HDCO}^+$	31.0134	1.39 ± 0.14	1.51 ± 0.01	0.50

 Table B.17: Fragmentation and isotopologic ratios for CH_3CHO , for FM with $D = -1'800$ V.

Parent / Daughters	Mass	Fragmentation ratio (%)		
		FM-SS	FM-OS	NIST
H_2^+	2.0151	8.60 ± 1.21	5.85 ± 0.12	\emptyset
C^+	11.9995	2.31 ± 0.19	1.18 ± 0.10	0.90
CH^+	13.0073	4.53 ± 0.21	3.07 ± 0.05	2.99
CH_2^+	14.0151	13.62 ± 0.42	9.45 ± 0.07	10.89
CH_3^+	15.0229	36.39 ± 1.11	32.76 ± 0.79	36.49
O^+CH_4^+	15.9944	8.41 ± 1.23	8.64 ± 0.20	5.69
HO^+	17.0022	0.97 ± 0.36	0.31 ± 0.20	0.30
H_2O^+	18.0100	3.17 ± 1.76	0.75 ± 0.44	1.09
C_2^+	23.9995	0.89 ± 0.05	1.11 ± 0.10	0.70
C_2H^+	25.0073	4.30 ± 0.01	3.70 ± 0.36	2.39
C_2H_2^+	26.0151	14.02 ± 0.45	13.09 ± 0.28	5.49
C_2H_3^+	27.0229	5.91 ± 0.36	4.21 ± 0.03	3.59
CO^+	27.9944	26.05 ± 2.21	41.97 ± 1.57	3.29
CHO^+	29.0022	100.0 ± 2.4	100.0 ± 2.0	100.00
CH_2O^+	30.0100	1.80 ± 0.04	1.84 ± 0.17	1.19
CH_3O^+	31.0178	0.56 ± 0.2	0.96 ± 0.01	0.30
C_2O^+	39.9944	1.48 ± 0.03	1.80 ± 0.13	1.09
C_2HO^+	41.0022	5.21 ± 0.09	6.21 ± 0.12	5.09
$\text{C}_2\text{H}_2\text{O}^+$	42.0100	11.38 ± 0.18	15.23 ± 0.09	12.79
$\text{C}_2\text{H}_3\text{O}^+$	43.0178	30.73 ± 0.62	52.68 ± 0.37	47.49
$\text{C}_2\text{H}_4\text{O}^+$	44.0257	55.80 ± 1.52	99.43 ± 1.08	82.60
$^{13}\text{CCH}_4\text{O}^+/\text{C}_2\text{H}_3\text{DO}^+$	45.0290	1.72 ± 0.05	3.25 ± 0.06	2.79

Table B.18: Fragmentation and isotopologic ratios for $C_3H_3N_3$, for FM with $D = -1'800$ V.

Parent / Daughters	Mass	Fragmentation ratio (%)		
		FM-SS	FM-OS	NIST
H_2^+	2.0151	12.32 ± 7.38	\emptyset	2.77
C^+	11.9995	3.64 ± 1.45	\emptyset	1.77
CH^+	13.0073	4.76 ± 1.89	\emptyset	2.17
N^+/CH_2^+	14.0088	11.24 ± 8.84	\emptyset	0.58
NH^+/CH_3^+	15.0166	54.30 ± 14.75	\emptyset	0.17
NH_2^+/CH_4^+	16.0245	3.00 ± 2.42	\emptyset	0.15
C_2^+	23.9995	2.14 ± 0.62	\emptyset	1.42
C_2H^+	25.0073	6.05 ± 2.95	\emptyset	2.06
$C_2H_2^+$	26.0151	34.46 ± 18.38	\emptyset	5.06
$C_2H_3^+$	27.0229	110.6 ± 28.25	\emptyset	41.55
$C_2H_4^+/N_2^+$	28.0181	112.2 ± 26.83	\emptyset	62.75
$C_2H_5^+$	29.0386	11.76 ± 8.60	\emptyset	1.15
m_{31}	≈ 31	1.26 ± 0.93	\emptyset	0.17
C_2N^+	38.0025	9.26 ± 4.29	\emptyset	4.61
C_2NH^+	39.0104	15.86 ± 9.46	\emptyset	4.28
$C_2NH_2^+$	40.0182	8.46 ± 3.59	\emptyset	2.99
$C_3H_3N_3^{++}$	40.5158	12.01 ± 2.08	\emptyset	\emptyset
$C_2NH_3^+$	41.0260	7.16 ± 5.46	\emptyset	0.35
m_{45}	≈ 45	2.00 ± 1.24	\emptyset	0.11
$C_2N_2^+$	52.0056	5.25 ± 0.47	\emptyset	3.79
$C_2N_2H^+$	53.0134	22.88 ± 1.59	\emptyset	23.16
$C_2N_2H_2^+$	54.0212	76.11 ± 0.59	\emptyset	75.05
m_{55}	≈ 55	3.26 ± 0.49	\emptyset	2.04
m_{59}	≈ 59	3.55 ± 1.89	\emptyset	0.14
$C_3N_2^+$	64.0056	0.11 ± 0.03	\emptyset	0.12
$C_3N_3^+$	78.0087	0.34 ± 0.12	\emptyset	0.13
$C_3H_3N_3^+$	81.0321	100.0 ± 13.6	\emptyset	100.00
$^{13}CC_2H_3N_3^+/C_3H_2DN_3^+$	82.0355	5.12 ± 0.10	\emptyset	4.17

B.3 $D = -1'000 \text{ V}$

 Table B.19: Fragmentation and isotopologic ratios for H_2O , CO , CO_2 , and Kr , for FM with $D = -1'000 \text{ V}$.

Parent / Daughters	Mass	Fragmentation ratio (%)		NIST
		FM-SS	FM-OS	
H^+	1.0073	13.02 ± 0.91	6.80 ± 1.34	\emptyset
H_2^+	2.0151	0.80 ± 0.30	0.09 ± 0.08	\emptyset
O^+	15.9944	1.34 ± 0.82	1.15 ± 0.06	0.90
OH^+	17.0022	23.34 ± 1.03	23.73 ± 0.42	21.22
H_2O^+	18.0100	100.0 ± 2.7	100.0 ± 0.8	100.0
HDO	19.0163	0.61 ± 0.15	0.54 ± 0.04	0.50
$\text{H}_2^{18}\text{O}^+$	20.0143	0.27 ± 0.06	0.29 ± 0.02	0.30
C^+	11.9995	3.31 ± 0.57	0.77 ± 0.02	4.70
O^+	15.9944	0.46 ± 0.15	0.08 ± 0.04	1.70
CO^+	27.9944	100.0 ± 5.1	100.0 ± 1.4	100.0
$^{13}\text{CO}^+$	28.9977	1.14 ± 0.22	1.21 ± 0.05	1.20
C^+	11.9995	0.44 ± 0.02	1.20 ± 0.10	8.71
O^+	15.9944	10.45 ± 0.24	5.07 ± 0.22	9.61
CO_2^{++}	21.9944	0.25 ± 0.07	0.75 ± 0.05	1.90
CO^+	27.9944	9.73 ± 0.25	3.86 ± 0.21	9.81
$^{13}\text{CO}^+$	28.9977	0.19 ± 0.03	0.06 ± 0.08	0.10
CO_2^+	43.9893	100.0 ± 2.5	100.0 ± 2.2	100.0
$^{13}\text{CO}_2^+$	44.9926	1.23 ± 0.12	1.35 ± 0.14	1.20
C^{18}OO^+	46.0049	0.38 ± 0.07	0.39 ± 0.07	0.40
$^{80}\text{Kr}^{++}$	39.9576	\emptyset	0.58 ± 0.12	\emptyset
$^{82}\text{Kr}^{++}$	40.9562	0.03 ± 0.02	3.03 ± 0.28	3.47
$^{83}\text{Kr}^{++}$	41.4565	0.04 ± 0.02	2.80 ± 0.21	\emptyset
$^{84}\text{Kr}^{++}$	41.9552	0.14 ± 0.06	15.11 ± 0.78	15.90
$^{86}\text{Kr}^{++}$	42.9548	0.05 ± 0.02	4.46 ± 0.37	4.98
$^{80}\text{Kr}^+$	79.9158	4.23 ± 0.09	4.03 ± 0.27	4.29
$^{82}\text{Kr}^+$	81.9129	20.85 ± 0.44	20.65 ± 0.35	20.60
$^{83}\text{Kr}^+$	82.9136	21.11 ± 0.49	20.82 ± 0.36	20.50
$^{84}\text{Kr}^+$	83.9109	100.0 ± 2.5	100.00 ± 2.0	100.0
$^{86}\text{Kr}^+$	85.9101	30.33 ± 0.77	30.79 ± 0.70	30.60

C. Tables of sensitivities

C.1 Granville-Phillips correction factors

Table C.1: Correction factors for the pressure measurements of the Granville-Phillips stabil ion gauge, computed from Granville-Phillips (2007) and Varian Vacuum Technologies (2001).

Species		Scale factor
Helium	He	5.556
Neon	Ne	3.333
Argon	Ar	0.775
Krypton	Kr	0.515
Xenon	Xe	0.348
Water	H ₂ O	0.893
Carbon monoxide	CO	0.952
Carbon dioxide	CO ₂	0.704
Methane	CH ₄	0.714
Ethane	C ₂ H ₆	0.385
Propane	C ₃ H ₈	0.238
n-Butane	C ₄ H ₁₀	0.204
Acetylene	C ₂ H ₂	0.526
Benzene	C ₆ H ₆	0.169
Naphthalene	C ₁₀ H ₈	0.103
Methanol	CH ₃ OH	0.556
Ethanol trans	C ₂ H ₅ OH	0.278
Formic acid	HCOOH	0.313
Acetic acid	CH ₃ COOH	0.649
Formaldehyde	H ₂ CO	0.586
Acetaldehyde	CH ₃ CHO	0.385
Triazine	C ₃ H ₃ N ₃	∅

C.2 D = -3'000 V

Table C.2: CO₂ and krypton sensitivities for D = -3'000 V, with RTOF OS.

Modes	Sensitivity [cm ³]		
	He (estimated)	CO ₂	Kr
FM – M503	1.19 · 10 ⁻²³	(4.84 ± 0.02) · 10 ⁻²²	(7.04 ± 0.08) · 10 ⁻²²
FM – M513	4.64 · 10 ⁻²³	(1.89 ± 0.01) · 10 ⁻²¹	(3.34 ± 0.01) · 10 ⁻²¹
FM – M523	6.98 · 10 ⁻²³	(2.84 ± 0.05) · 10 ⁻²¹	(5.40 ± 0.04) · 10 ⁻²¹
FS – M513	∅	(7.06 ± 0.01) · 10 ⁻²³	(2.73 ± 0.01) · 10 ⁻²²

C.3 $D = -1'800 \text{ V}$

Table C.3: Sensitivity conversion factors for SS and OS modes, for the event data, with $D = -1'800 \text{ V}$. Sensitivities for the histogram data are (28.0 ± 2.2) times higher. Modes 511 for SS and 513 for OS have been chosen as references, as they both have the highest sensitivities.

Mode	Conversion factor
M501	0.165 ± 0.047
M511	1.000
M521	0.216 ± 0.063
M506	0.092 ± 0.025
M516	0.111 ± 0.029
M526	0.033 ± 0.009
M513	1.000
M543	0.420 ± 0.034

Table C.4: Sensitivities for modes 511 (events) and 513 (events), with $D = -1'000 \text{ V}$. Value for triazine (*) is relative to N_2 (i.e. not corrected for the pressure readings from the Granville-Phillips). Only the statistical error on the fit is given here, an estimated error of 10 % has to be added due to the uncertainty on the pressure readings.

Species		Sensitivity [cm^3]	
		SS	OS
Helium	He	$(4.76 \pm 0.18) \cdot 10^{-23}$	$(5.65 \pm 0.19) \cdot 10^{-23}$
Neon	Ne	$(5.86 \pm 0.19) \cdot 10^{-22}$	$(1.02 \pm 0.08) \cdot 10^{-22}$
Argon	Ar	$(3.71 \pm 0.02) \cdot 10^{-21}$	$(2.24 \pm 0.02) \cdot 10^{-21}$
Krypton	Kr	$(2.26 \pm 0.08) \cdot 10^{-21}$	$(2.18 \pm 0.03) \cdot 10^{-21}$
Xenon	Xe	$(5.00 \pm 0.23) \cdot 10^{-21}$	$(4.04 \pm 0.08) \cdot 10^{-21}$
Water	H_2O	$(1.00 \pm 0.20) \cdot 10^{-21}$	$(5.81 \pm 0.09) \cdot 10^{-22}$
Carbon monoxide	CO	$(2.36 \pm 0.08) \cdot 10^{-21}$	$(1.22 \pm 0.02) \cdot 10^{-21}$
Carbon dioxide	CO_2	$(4.93 \pm 0.11) \cdot 10^{-21}$	$(2.39 \pm 0.04) \cdot 10^{-21}$
Methane	CH_4	$(3.49 \pm 0.04) \cdot 10^{-21}$	$(1.33 \pm 0.01) \cdot 10^{-21}$
Ethane	C_2H_6	$(9.03 \pm 0.72) \cdot 10^{-21}$	$(2.56 \pm 0.01) \cdot 10^{-21}$
Propane	C_3H_8	$(1.74 \pm 0.01) \cdot 10^{-20}$	$(3.97 \pm 0.05) \cdot 10^{-21}$
n-Butane	C_4H_{10}	$(2.72 \pm 0.03) \cdot 10^{-20}$	$(4.67 \pm 0.03) \cdot 10^{-21}$
Acetylene	C_2H_2	$(3.28 \pm 0.33) \cdot 10^{-21}$	$(8.00 \pm 0.01) \cdot 10^{-22}$
Benzene	C_6H_6	$(2.58 \pm 0.02) \cdot 10^{-20}$	$(4.52 \pm 0.13) \cdot 10^{-21}$
Naphthalene	C_{10}H_8	$(2.15 \pm 0.35) \cdot 10^{-20}$	\emptyset
Methanol	CH_3OH	$(5.93 \pm 0.24) \cdot 10^{-21}$	$(1.71 \pm 0.04) \cdot 10^{-21}$
Ethanol trans	$\text{C}_2\text{H}_5\text{OH}$	$(1.67 \pm 0.05) \cdot 10^{-20}$	$(3.32 \pm 0.01) \cdot 10^{-21}$
Formic acid	HCOOH	$(5.29 \pm 0.25) \cdot 10^{-21}$	$(2.27 \pm 0.02) \cdot 10^{-21}$
Acetic acid	CH_3COOH	$(6.23 \pm 0.35) \cdot 10^{-21}$	$(1.47 \pm 0.01) \cdot 10^{-21}$
Formaldehyde	H_2CO	$(4.22 \pm 0.24) \cdot 10^{-21}$	$(1.73 \pm 0.01) \cdot 10^{-21}$
Acetaldehyde	CH_3CHO	$(7.91 \pm 0.03) \cdot 10^{-21}$	$(1.67 \pm 0.02) \cdot 10^{-21}$
Triazine	$\text{C}_3\text{H}_3\text{N}_3$	* $(4.01 \pm 0.23) \cdot 10^{-21}$	\emptyset

C.4 $D = -1'000$ V

Table C.5: Sensitivity conversion factors for SS and OS modes, for the event data, with $D = -1'000$ V. Sensitivities for the histogram data are (20.5 ± 1.5) times higher. Modes 521 for SS and 523 for OS have been chosen as references, as they both have the highest sensitivities.

Mode	Conversion factor
M501	0.118 ± 0.032
M511	0.229 ± 0.062
M521	1.000
M506	0.068 ± 0.012
M516	0.499 ± 0.135
M526	0.112 ± 0.030
M513	0.116 ± 0.001
M523	1.000
M543	0.059 ± 0.001
M553	0.517 ± 0.009

Table C.6: Scale factors for the extrapolation of the sensitivities from $D = -1'800$ V (mode 511) to $D = -1'000$ V (mode 521).

	Scale factor
SS	$(2.95 \pm 0.82) \cdot 10^{-2}$
OS	3.54 ± 0.20

Table C.7: Sensitivities for modes 521 (events) and 523 (events), with $D = -1'000$ V.

Species	Sensitivity [cm^3]	
	SS	OS
H ₂ O	$(5.88 \pm 0.90) \cdot 10^{-23}$	$(5.73 \pm 0.09) \cdot 10^{-21}$
CO	$(9.12 \pm 0.89) \cdot 10^{-23}$	$(5.03 \pm 0.08) \cdot 10^{-21}$
CO ₂	$(1.40 \pm 0.02) \cdot 10^{-23}$	$(6.84 \pm 0.01) \cdot 10^{-21}$
Kr	$(6.67 \pm 0.03) \cdot 10^{-23}$	$(1.05 \pm 0.02) \cdot 10^{-20}$

Bibliography

- ESA website. http://www.esa.int/spaceinimages/Images/2015/01/Comet_vital_statistics. Retrieved October 26, 2015.
- K. Altwegg. ROSINA RTOF activities, report for the period 16. Feb.-4. March 2010. Technical Report RO-ROS-TR-1130, March 2010.
- K. Altwegg, H. Balsiger, A. Bar-Nun, J. J. Berthelier, A. Bieler, P. Bochslers, C. Briois, U. Calmonte, M. Combi, J. De Keyser, P. Eberhardt, B. Fiethe, S. Fuselier, S. Gasc, T. I. Gombosi, K. C. Hansen, M. Hässig, A. Jäckel, E. Kopp, A. Korth, L. Le Roy, U. Mall, B. Marty, O. Mousis, E. Neefs, T. Owen, H. Rème, M. Rubin, T. Sémon, C.-Y. Tzou, H. Waite, and P. Wurz. 67P/Churyumov-Gerasimenko, a Jupiter family comet with a high D/H ratio. *Science*, 347(27):1261952, January 2015. doi: 10.1126/science.1261952.
- H. Balsiger, K. Altwegg, P. Bochslers, P. Eberhardt, J. Fischer, S. Graf, A. Jäckel, E. Kopp, U. Langer, M. Mildner, J. Müller, T. Riesen, M. Rubin, S. Scherer, P. Wurz, S. Wüthrich, E. Arijs, S. Delanoye, J. de Keyser, E. Neefs, D. Nevejans, H. Rème, C. Aoustin, C. Mazelle, J.-L. Médale, J. A. Sauvaud, J.-J. Berthelier, J.-L. Bertaux, L. Duvet, J.-M. Illiano, S. A. Fuselier, A. G. Ghielmetti, T. Magoncelli, E. G. Shelley, A. Korth, K. Heerlein, H. Lauche, S. Livi, A. Loose, U. Mall, B. Wilken, F. Gliem, B. Fiethe, T. I. Gombosi, B. Block, G. R. Carignan, L. A. Fisk, J. H. Waite, D. T. Young, and H. Wollnik. Rosina Rosetta Orbiter Spectrometer for Ion and Neutral Analysis. *Space Science Reviews*, 128:745–801, February 2007. doi: 10.1007/s11214-006-8335-3.
- H. Balsiger, K. Altwegg, A. Bar-Nun, J.-J. Berthelier, A. Bieler, P. Bochslers, C. Briois, U. Calmonte, M. Combi, J. De Keyser, P. Eberhardt, B. Fiethe, S. A. Fuselier, S. Gasc, T. I. Gombosi, K. C. Hansen, M. Hässig, A. Jäckel, E. Kopp, A. Korth, L. Le Roy, U. Mall, B. Marty, O. Mousis, T. Owen, H. Rème, M. Rubin, T. Sémon, C.-Y. Tzou, J. H. Waite, and P. Wurz. Detection of argon in the coma of comet 67P/Churyumov-Gerasimenko. *Science Advances*, 1(8), 2015. doi: 10.1126/sciadv.1500377.
- A. Bieler, K. Altwegg, L. Hofer, A. Jäckel, A. Riedo, T. Sémon, P. Wahlström, and P. Wurz. Optimization of mass spectrometers using the adaptive particle swarm algorithm. *Journal of Mass Spectrometry*, 46(11):1143–1151, 2011.
- A. Bieler, K. Altwegg, H. Balsiger, A. Bar-Nun, J.-J. Berthelier, P. Bochslers, C. Briois, U. Calmonte, M. Combi, J. De Keyser, E. F. van Dishoeck, B. Fiethe, S. A. A. Fuselier, S. Gasc, T. Gombosi, K. C. Hansen, M. Hässig, A. Jäckel, E. Kopp, A. Korth, L. Le Roy, U. Mall, R. Maggiolo, B. Marty, O. Mousis, T. Owen, H. Rème, M. Rubin, T. Sémon, C.-Y. Tzou, J. H. Waite, C. Walsh, and P. Wurz. Abundant molecular oxygen in the coma of comet 67P/Churyumov-Gerasimenko. *Nature*, 526:678–681, October 2015a. doi: 10.1038/nature15707.
- A. Bieler, K. Altwegg, H. Balsiger, J.-J. Berthelier, U. Calmonte, M. Combi, J. De Keyser, B. Fiethe, N. Fougere, S. Fuselier, S. Gasc, T. Gombosi, K. Hansen,

- M. Hässig, Z. Huang, A. Jäckel, X. Jia, L. Le Roy, U. A. Mall, H. Rème, M. Rubin, V. Tennishev, G. Tóth, C.-Y. Tzou, and P. Wurz. Comparison of 3D kinetic and hydrodynamic models to ROSINA-COPS measurements of the neutral coma of 67P/Churyumov-Gerasimenko. *Astronomy and Astrophysics*, 583:A7, 2015b. doi: 10.1051/0004-6361/201526178. URL <http://dx.doi.org/10.1051/0004-6361/201526178>.
- N. Biver, D. Bockelée-Morvan, R. Moreno, J. Crovisier, P. Colom, D. C. Lis, A. Sandqvist, J. Boissier, D. Despois, and S. N. Milam. Ethyl alcohol and sugar in comet C/2014 Q2 (Lovejoy). *Science Advances*, 1(9), 2015. doi: 10.1126/sciadv.1500863.
- D. Bockelée-Morvan, J. Crovisier, M. J. Mumma, and H. A. Weaver. *The composition of cometary volatiles*, pages 391–423. 2004.
- W. A. de Heer and P. Milani. Large ion volume time-of-flight mass spectrometer with position- and velocity-sensitive detection capabilities for cluster beams. *Review of Scientific Instruments*, 62:670–677, March 1991. doi: 10.1063/1.1142066.
- B. Donn and D. Hughes. A fractal model of a cometary nucleus formed by random accretion. In B. Battrick, E. J. Rolfe, and R. Reinhard, editors, *ESLAB Symposium on the Exploration of Halley’s Comet*, volume 250 of *ESA Special Publication*, pages 523–524, December 1986.
- P. Eberhardt. Comet Halley’s Gas Composition and Extended Sources: Results from the Neutral Mass Spectrometer on Giotto. *Space Science Reviews*, 90:45–52, October 1999. doi: 10.1023/A:1005221309219.
- P. Eberhardt, D. Krankowsky, W. Schulte, U. Dolder, P. Lammerzähl, J. J. Berthelier, J. Woweries, U. Stubbemann, R. R. Hodges, J. H. Hoffman, and J. M. Illiano. The CO and N₂ Abundance in Comet P/Halley. *Astronomy and Astrophysics*, 187:481, November 1987.
- P. D. Feldman and W. H. Brune. Carbon production in comet West 1975n. *Astrophysical Journal, Letters*, 209:L45–L48, October 1976. doi: 10.1086/182263.
- I. Ferrín, J. Zuluaga, and P. Cuartas. The location of Asteroidal Belt Comets (ABCs), in a comet’s evolutionary diagram: The Lazarus Comets. *Monthly Notices of the RAS*, 434:1821–1837, September 2013. doi: 10.1093/mnras/stt839.
- M. C. Festou, H. Rickman, and R. M. West. Comets. I - Concepts and observations. *Astronomy and Astrophysics Reviews*, 4:363–447, April 1993. doi: 10.1007/BF00872944.
- S. A. Fuselier, K. Altwegg, H. Balsiger, J. J. Berthelier, A. Bieler, C. Briois, T. W. Broiles, J. L. Burch, U. Calmonte, G. Cessateur, M. Combi, J. De Keyser, B. Fiethe, M. Galand, S. Gasc, T. I. Gombosi, H. Gunell, K. C. Hansen, M. Hässig, A. Jäckel, A. Korth, L. Le Roy, U. Mall, K. E. Mandt, S. M. Petriner, S. Raghuram, H. Rème, M. Rinaldi, M. Rubin, T. Sémon, K. J. Trattner, C.-Y. Tzou, E. Vigren, J. H. Waite, and P. Wurz. ROSINA/DFMS and IES observations of 67P: Ion-neutral chemistry in the coma of a weakly outgassing comet. *Astronomy and Astrophysics*, 583:A2, 2015. doi: 10.1051/0004-6361/201526210. URL <http://dx.doi.org/10.1051/0004-6361/201526210>.

- S. Graf, K. Altwegg, H. Balsiger, A. Jäckel, E. Kopp, U. Langer, W. Luithardt, C. Westermann, and P. Wurz. A cometary neutral gas simulator for gas dynamic sensor and mass spectrometer calibration. *Journal of Geophysical Research (Planets)*, 109: E07S08, May 2004. doi: 10.1029/2003JE002188.
- Granville-Phillips. *Granville-Phillips Series 370 Stabil-Ion[®] Vacuum Measurement Controller Instruction Manual*, 2007.
- M. Hässig. *Sensitivity and fragmentation calibration of the ROSINA Double Focusing Mass Spectrometer*. PhD thesis, University of Bern, 2013.
- M. Hässig, K. Altwegg, H. Balsiger, A. Bar-Nun, J. J. Berthelier, A. Bieler, P. Bochslers, C. Briois, U. Calmonte, M. Combi, J. De Keyser, P. Eberhardt, B. Fiethe, S. A. Fuselier, M. Galand, S. Gasc, T. I. Gombosi, K. C. Hansen, A. Jäckel, H. U. Keller, E. Kopp, A. Korth, E. Kührt, L. Le Roy, U. Mall, B. Marty, O. Mousis, E. Neefs, T. Owen, H. Rème, M. Rubin, T. Sémon, C. Tornow, C.-Y. Tzou, J. H. Waite, and P. Wurz. Time variability and heterogeneity in the coma of 67P/Churyumov-Gerasimenko. *Science*, 347(1):aaa0276, January 2015. doi: 10.1126/science.aaa0276.
- W. M. Haynes. “Atomic Masses and Abundances” in *CRC Handbook of Chemistry and Physics, 96th Edition (Internet Version 2016)*.
- M. Hohl, P. Wurz, S. Scherer, K. Altwegg, and H. Balsiger. Mass selective blanking in a compact multiple reflection time-of-flight mass spectrometer. *International journal of mass spectrometry*, 188(3):189–197, 1999.
- H. H. Hsieh and D. Jewitt. A Population of Comets in the Main Asteroid Belt. *Science*, 312:561–563, April 2006. doi: 10.1126/science.1125150.
- D. C. Jewitt. *From cradle to grave: the rise and demise of the comets*, pages 659–676. 2004.
- E. Johnson and A. Nier. Angular aberrations in sector shaped electromagnetic lenses for focusing beams of charged particles. *Physical Review*, 91(1):10, 1953.
- J. Kennedy and R. C. Eberhart. Particle swarm optimization. In *Proc. IEEE Int. Conf. Neural Netw.*, volume 2, pages 1942–1948. 1995.
- Y.-K. Kim, K.K. Irikura, M.E. Rudd, M.A. Ali, P.M. Stone, J. Chang, J.S. Coursey, R.A. Dragoset, A.R. Kishore, K.J. Olsen, A.M. Sansonetti, G.G. Wiersma, D.S. Zucker, and Zucker M.A. Electron-impact cross section database. *NIST Standard Reference Database 107*, 2005.
- L. Le Roy, K. Altwegg, H. Balsiger, J.-J. Berthelier, A. Bieler, C. Briois, U. Calmonte, M. R. Combi, J. De Keyser, F. Dhooghe, B. Fiethe, S. A. Fuselier, S. Gasc, T. I. Gombosi, M. Hässig, A. Jäckel, M. Rubin, and C.-Y. Tzou. Inventory of the volatiles on comet 67P/Churyumov-Gerasimenko from Rosetta/ROSINA. *Astronomy and Astrophysics*, 583:A1, 2015. doi: 10.1051/0004-6361/201526450. URL <http://dx.doi.org/10.1051/0004-6361/201526450>.
- A. Luspay-Kuti, M. Hässig, S. A. Fuselier, K. E. Mandt, K. Altwegg, H. Balsiger, S. Gasc, A. Jäckel, L. Le Roy, M. Rubin, C.-Y. Tzou, P. Wurz, O. Mousis, F. Dhooghe, J. J. Berthelier, B. Fiethe, T. I. Gombosi, and U. Mall. Composition-dependent outgassing of comet 67P/Churyumov-Gerasimenko from

- ROSINA/DFMS. *Astronomy and Astrophysics*, 583:A4, 2015. doi: 10.1051/0004-6361/201526205. URL <http://dx.doi.org/10.1051/0004-6361/201526205>.
- B.A. Mamyrin, V.I. Karataev, D.V. Shmikk, and V.A. Zagulin. The mass-reflectron, a new non-magnetic time-of-flight mass spectrometer with high resolution. *Zh. Eksp. Teor. Fiz.*, 64:82–89, 1973.
- TD Mark. Fundamental aspects of electron impact ionization. *International Journal of Mass Spectrometry and Ion Physics*, 45:125–145, 1982.
- A. Morbidelli. *Comets and Their Reservoirs: Current Dynamics and Primordial Evolution*, pages 79–164. 2008.
- S. Mottola, Lowry, S., Snodgrass, C., Lamy, P. L., Toth, I., Rožek, A., Sierks, H., A'Hearn, M. F., Angrilli, F., Barbieri, C., Barucci, M. A., Bertaux, J.-L., Cremonese, G., Da Deppo, V., Davidsson, B., De Cecco, M., Debei, S., Fornasier, S., Fulle, M., Groussin, O., Gutiérrez, P., Hviid, S. F., Ip, W., Jorda, L., Keller, H. U., Knollenberg, J., Koschny, D., Kramm, R., Kührt, E., Küppers, M., Lara, L., Lazzarin, M., Lopez Moreno, J. J., Marzari, F., Michalik, H., Naletto, G., Rickman, H., Rodrigo, R., Sabau, L., Thomas, N., Wenzel, K.-P., Agarwal, J., Bertini, I., Ferri, F., Güttler, C., Magrin, S., Oklay, N., Tubiana, C., and Vincent, J.-B. The rotation state of 67P/Churyumov-Gerasimenko from approach observations with the OSIRIS cameras on Rosetta. *Astronomy and Astrophysics*, 569:L2, 2014. doi: 10.1051/0004-6361/201424590. URL <http://dx.doi.org/10.1051/0004-6361/201424590>.
- M. J. Mumma and S. B. Charnley. The Chemical Composition of Comets—Emerging Taxonomies and Natal Heritage. *Annual Review of Astron and Astrophys*, 49:471–524, September 2011. doi: 10.1146/annurev-astro-081309-130811.
- M. J. Mumma, M. A. Disanti, N. dello Russo, M. Fomenkova, K. Magee-Sauer, C. D. Kaminski, and D. X. Xie. Detection of Abundant Ethane and Methane, Along with Carbon Monoxide and Water, in Comet C/1996 B2 Hyakutake: Evidence for Interstellar Origin. *Science*, 272:1310–1314, May 1996. doi: 10.1126/science.272.5266.1310.
- M. J. Mumma, M. A. DiSanti, N. Dello Russo, K. Magee-Sauer, E. Gibb, and R. Novak. Remote infrared observations of parent volatiles in comets: A window on the early solar system. *Advances in Space Research*, 31:2563–2575, June 2003. doi: 10.1016/S0273-1177(03)00578-7.
- J. H. Oort. The structure of the cloud of comets surrounding the Solar System and a hypothesis concerning its origin. *Bulletin Astronomical Institute of the Netherlands*, 11:91–110, January 1950.
- J. Oró. Comets and the Formation of Biochemical Compounds on the Primitive Earth. *Nature*, 190:389–390, April 1961. doi: 10.1038/190389a0.
- T. Owen. Planetary science: Huygens rediscovers Titan. *Nature*, 438:756–757, December 2005. doi: 10.1038/438756a.
- T. Owen and A. Bar-Nun. Comets, Impacts, and Atmospheres. *Icarus*, 116:215–226, 1995. doi: 10.1006/icar.1995.1122.
- M. Rubin, K. Altwegg, H. Balsiger, A. Bar-Nun, J.-J. Berthelier, A. Bieler, P. Bochsler,

- C. Briois, U. Calmonte, M. Combi, J. De Keyser, F. Dhooghe, P. Eberhardt, B. Fiethe, S. A. Fuselier, S. Gasc, T. I. Gombosi, K. C. Hansen, M. Hässig, A. Jäckel, E. Kopp, A. Korth, L. Le Roy, U. Mall, B. Marty, O. Mousis, T. Owen, H. Rème, T. Sémon, C.-Y. Tzou, J. H. Waite, and P. Wurz. Molecular nitrogen in comet 67P/Churyumov-Gerasimenko indicates a low formation temperature. *Science*, 348: 232–235, April 2015. doi: 10.1126/science.aaa6100.
- S. Scherer, K. Altwegg, H. Balsiger, J. Fischer, A. Jäckel, A. Korth, M. Mildner, D. Piazza, H. Rème, and P. Wurz. A novel principle for an ion mirror design in time-of-flight mass spectrometry. *International Journal of Mass Spectrometry*, 251(1):73–81, 2006.
- B. Schläppi, K. Altwegg, H. Balsiger, M. Hässig, A. Jäckel, P. Wurz, B. Fiethe, M. Rubin, S. A. Fuselier, J. J. Berthelier, J. de Keyser, H. Rème, and U. Mall. Influence of spacecraft outgassing on the exploration of tenuous atmospheres with in situ mass spectrometry. *Journal of Geophysical Research (Space Physics)*, 115:A12313, December 2010. doi: 10.1029/2010JA015734.
- F. Scholten, F. Preusker, L. Jorda, and S. Hviid. Reference Frames and Mapping Schemes of Comet 67P/C-G, RO-C-MULTI-5-67P-SHAPE-V1.0:CHEOPS_REF_FRAME_V1. *NASA Planetary Data System and ESA Planetary Science Archive*, 2015.
- R. Schulz, C. Alexander, H. Boehnhardt, and K.-H. Glaßmeier. *ESA’s Mission to the Origin of the Solar System*. Springer-Verlag New York, 1 edition, 2009. ISBN 978-0-387-77517-3.
- G. Schwehm and R. Schulz. Rosetta Goes to Comet Wirtanen. *Space Science Reviews*, 90:313–319, October 1999. doi: 10.1023/A:1005231006010.
- M. A. Sephton. Organic compounds in carbonaceous meteorites. *Natural product reports*, 19(3):292–311, 2002.
- B. Sinzig. Charakterisierung des Flugzeitmassenspektrometers ROSINA RTOF. Master’s thesis, Universität Bern, 2003.
- S.E. Stein. *NIST Mass Spec Data Center, “Mass Spectra” in NIST Chemistry WebBook, NIST Standard Reference Database Number 69*.
- S. A. Stern. The evolution of comets in the Oort cloud and Kuiper belt. *Nature*, 424: 639–642, August 2003.
- P. Swings and T. Page. The Spectrum of Comet Bester (1947k). *Astrophysical Journal*, 111:530, May 1950. doi: 10.1086/145295.
- C. Szmytkowski, K. Maciag, and G. Karwasz. Absolute electron-scattering total cross section measurements for noble gas atoms and diatomic molecules. *Physica Scripta*, 54:271–280, 1996.
- Varian Vacuum Technologies. *Multi-Gauge Controller Part No. L8350301 Instruction Manual*, February 2001.
- M. Vinodkumar, K. N. Joshipura, C. Limbachiya, and N. Mason. Theoretical calculations of the total and ionization cross sections for electron impact on some sim-

- ple biomolecules. *Phys. Rev. A*, 74:022721, Aug 2006. doi: 10.1103/PhysRevA.74.022721. URL <http://link.aps.org/doi/10.1103/PhysRevA.74.022721>.
- P. R. Weissman. Are cometary nuclei primordial rubble piles? *Nature*, 320:242–244, March 1986. doi: 10.1038/320242a0.
- C. B. Westermann, W. Luithardt, E. Kopp, T. Koch, R. Liniger, H. Hofstetter, J. Fischer, K. Altwegg, and H. Balsiger. A high precision calibration system for the simulation of cometary gas environments. *Measurement Science and Technology*, 12:1594–1603, September 2001. doi: 10.1088/0957-0233/12/9/327.
- F. L. Whipple. A comet model. I. The acceleration of Comet Encke. *Astrophysical Journal*, 111:375–394, March 1950. doi: 10.1086/145272.
- P. Wurz, M. Rubin, K. Altwegg, H. Balsiger, J.-J. Berthelier, A. Bieler, U. Calmonte, J. De Keyser, B. Fiethe, S. A. Fuselier, A. Galli, S. Gasc, T. I. Gombosi, A. Jäckel, L. Le Roy, U. A. Mall, H. Rème, V. Tennishev, and C.-Y. Tzou. Solar wind sputtering of dust on the surface of 67P/Churyumov-Gerasimenko. *Astronomy and Astrophysics*, 583:A22, 2015. doi: 10.1051/0004-6361/201525980. URL <http://dx.doi.org/10.1051/0004-6361/201525980>.

Acknowledgments

My first thoughts go to Prof. Dr. Kathrin Altwegg for offering me this wonderful opportunity to participate in such a successful project. Her availability, determination, wisdom, and straightforwardness are an everyday inspiration. Special thanks also go to Prof. Dr. Stephen Fuselier for refereeing this work, and to Prof. Dr. Willy Benz for chairing the defense.

A few people taught me more in four years than during my entire studies: I would like to express my deepest gratitude to Dr. Annette Jäckel, for telling me everything there is to know about RTOF, teaching me how to impeccably write in a labbook, and reading very carefully through this document; to Adrian Etter, *the man who can fix everything*, for being himself; and to Prof. Dr. Peter Wurz for his many lectures and advices about mass spectrometry, diplomacy, and professional life.

To all the actual and former ROSINA group members not mentioned above, I want to express how grateful I am for sharing with me such a huge amount of knowledge in so many fields: Prof. Dr. Hans Balsiger, Dr. André Bieler, Dr. Myrtha Hässig, Dr. Lukas Hofer, Dr. Léna Le Roy, Dr. Timm Riesen, PD Martin Rubin, Dr. Bernard Schläppi, and Thierry Sémon. The long discussions with the RTOF Co-Is and associates were as well really helpful: many thanks to Dr. Urs Mall, Dr. Axel Korth, Prof. Dr. Henri Rème, Dr. Philippe Garnier, and Margaux Hoang. I want to dedicate very special thanks to the best office-mates ever: Dr. Ursina Calmonte and very-soon-Dr. Chia-Yu Tzou. I am impressed by your ability to withstand a colleague like myself for so long without becoming crazy.

Hereinafter, I want to deeply thank both Alain Mimouni and Werner Hirschi for helping me finding my way in the professional world as well as for their continuous help in my personnel life.

English is always a source of concern for non-native English speakers, especially the ones endowed with a brain filled to the brim with French exceptions; many thanks to Victoria Roloff and Peter Stephenson for making this thesis look a bit more American and a bit less French. And for not letting me forget my French, I warmly thank the *French speaking mafia*: Dr. Antoine Roth, Cléa Serpollier, Anthony Servonet, Dr. Thomas Smith, Amaury Thiabaud, and Zuriñe Yoldi. Dr. Julien Gouman deserves a special status in this team for his long friendship and his unconditional support.

On a more personal level, I would like to thank my parents, Annie and Dominique, my brothers, Guillaume and Grégoire, and Zoulikha and Rémi for always supporting my choices, and most importantly I want to thank my wife Amel for sharing her life with me, for offering me the most wonderful gift a man can dream of, and for bringing me love and support since more than 15 years; I would never have gotten as far if it hadn't been for you.

Erklärung

gemäss Art. 28 Abs. 2 RSL 05

Name/Vorname: Gasc Sébastien

Matrikelnummer: 11-132-552

Studiengang: Physik

Bachelor

Master

Dissertation

Titel der Arbeit: Sensitivity and Fragmentation Calibration of the ROSINA
Reflectron-type Time-Of-Flight Mass Spectrometer

LeiterIn der Arbeit: Prof. Dr. Kathrin Altwegg

Ich erkläre hiermit, dass ich diese Arbeit selbständig verfasst und keine anderen als die angegebenen Quellen benutzt habe. Alle Stellen, die wörtlich oder sinngemäss aus Quellen entnommen wurden, habe ich als solche gekennzeichnet. Mir ist bekannt, dass andernfalls der Senat gemäss Artikel 36 Absatz 1 Buchstabe r des Gesetzes vom 5. September 1996 über die Universität zum Entzug des auf Grund dieser Arbeit verliehenen Titels berechtigt ist. Ich gewähre hiermit Einsicht in diese Arbeit.

Bern, 18/12/2015

Ort/Datum

Unterschrift

Sébastien GASC

Boulevard de la Forêt 55

1009 Pully

SWITZERLAND

Phone: +41 78 936 68 78

E-Mail: sebastien.gasc@space.unibe.ch

French citizen, 30 years old, married, 1 child. Driver license.

Education

Since October 2011	PhD in Space Research and Planetary Sciences: «Sensitivity and fragmentation calibration of the ROSINA Reflectron-type Time-Of-Flight mass spectrometer» – Physics Institute of the University of Bern, Switzerland
2010 – 2011	2nd year of the Master Degree: «Astronomical and Space-based Systems Engineering», Observatoire de Paris, France
2008 – 2010	1st year of the Master Degree: «Astronomy, Astrophysics, and Space Engineering», Observatoire de Paris, and 1 st year of the Master «Physique Fondamentale et Sciences de l'Ingénieur», Paris 7 – Denis Diderot, France
2005 –2008	Bachelor's degree in Physics, Paris 7 – Denis Diderot, France
2003 – 2005	Premier Cycle d'Etudes Médicales 1 , Paris 5 – René Descartes, France
2003	High school degree , with honors

Research

2011	6-month internship – Sagem REOSC – implementation of an ion source used for Ion Assisted Deposition in a large evaporating unit
2010	6-month internship – Physics Institute of the University of Bern – mass spectrometry with an ECR (electron cyclotron resonance) ion source for the ROSETTA mission
2009	3-month internship – «Institut de Mécanique Céleste et de Calcul des Ephémérides», Observatoire de Paris – spectral analysis of near-earth asteroids for the MARCO POLO mission
2007	7-week internship – «AstroParticules et Cosmologie» laboratory, CNRS – laser stabilization for the LISA mission

Teaching Experience

Since October 2011	Practical work in Physics for 1 st year students in «Minor Physics and Pharmacy»
Since October 2011	Practical work in Physics for 2 nd year students in «Major Physics»

Conferences

- 2015** **European Geosciences Union General Assembly**
Poster: « Evolution of the coma composition at 67P/Churyumov-Gerasimenko as seen by ROSINA/Rosetta from November 2014 to April 2015 » – Vienna, Austria
- 2014** **Division of Planetary Sciences Meeting**
Oral: « Preliminary results seen with Rosetta/ROSINA: early cometary activity of 67P/Churyumov-Gerasimenko » – Tucson, AZ, USA
- 2014** **European Geosciences Union General Assembly**
Poster: « Sensitivity and fragmentation calibration of the time-of-flight mass spectrometer RTOF on board ESA's Rosetta mission » – Vienna, Austria

Miscellaneous

Thematic schools

- 2013** **CSH Summer School on cosmochemistry** – Schwägalp, Switzerland
- 2012** **Alpbach Summer School** – Exploration of the Giant Planets and their Systems – Alpbach, Austria

Public relations

- 2015** **TecDay @Madame-de-Staël, Geneva; @LDDR, Neuchâtel**
- 2014** **TecDay @Beaulieu, Lausanne**
- 2013** **TecDay @HoPro, Zürich; @Emilie-Gourd, Geneva; @Saint-Michel, Fribourg**
- Since 2012** **Nationaler Zukunftstag am Center for Space and Habitability**

Computer skills

Programming: C, python, fortran, IDL/GDL, gnuplot, unix, HTML
Simulating: MatLab, Mathematica

Languages

French, native language
English, full professional proficiency (ILR scale)
German, professional working proficiency (ILR scale)

Publications

2016 (in prep.)

Sensitivity and fragmentation calibration of the time-of-flight mass spectrometer RTOF on board ESA's Rosetta mission. S. Gasc, K. Altwegg, A. Jäckel, L. Le Roy, M. Rubin, P. Wurz, B. Fiethe, A. Korth, U. Mall, H. Rème.

2015

High time resolution in-situ investigation of major cometary volatiles around 67P/C-G at 3.1 - 2.3 AU measured with ROSINA-RTOF. U. Mall, K. Altwegg, H. Balsiger, A. Bar-Nun, J.-J. Berthelier, A. Bieler, P. Bochsler, C. Briois, U. Calmonte, M. R. Combi, B. Dabrowski, J. De Keyser, F. Dhooghe, B. Fiethe, S. A. Fuselier, A. Galli, P. Garnier, S. Gasc, T. I. Gombosi, K. C. Hansen, M. Hässig, M. Hoang, A. Jäckel, E. Kopp, A. Korth, L. Le Roy, B. Magee, B. Marty, O. Mousis, H. Rème, M. Rubin, T. Sémon, C.-Y. Tzou, J. H. Waite, P. Wurz. (submitted)

Comparison of 3D kinetic and hydrodynamic models to ROSINA-COPS measurements of the neutral coma of 67P/Churyumov-Gerasimenko. A. Bieler, K. Altwegg, H. Balsiger, J.-J. Berthelier, U. Calmonte, M. Combi, J. De Keyser, B. Fiethe, N. Fougere, S. Fuselier, S. Gasc, T. Gombosi, K. Hansen, M. Hässig, Z. Huang, A. Jäckel, X. Jia, L. Le Roy, U. A. Mall, H. Rème, M. Rubin, V. Tennishev, G. Tóth, C.-Y. Tzou, and P. Wurz. *Astronomy and Astrophysics*, 583:A7, 2015. doi: 10.1051/0004-6361/201526178.

ROSINA/DFMS and IES observations of 67P: Ion-neutral chemistry in the coma of a weakly outgassing comet. S. A. Fuselier, K. Altwegg, H. Balsiger, J. J. Berthelier, A. Bieler, C. Briois, T. W. Broiles, J. L. Burch, U. Calmonte, G. Cessateur, M. Combi, J. De Keyser, B. Fiethe, M. Galand, S. Gasc, T. I. Gombosi, H. Gunell, K. C. Hansen, M. Hässig, A. Jäckel, A. Korth, L. Le Roy, U. Mall, K. E. Mandt, S. M. Petrinec, S. Raghuram, H. Rème, M. Rinaldi, M. Rubin, T. Sémon, K. J. Trattner, C.-Y. Tzou, E. Vigren, J. H. Waite, and P. Wurz. *Astronomy and Astrophysics*, 583:A2, 2015. doi: 10.1051/0004-6361/201526210.

Inventory of the volatiles on comet 67P/Churyumov-Gerasimenko from Rosetta/ROSINA. L. Le Roy, K. Altwegg, H. Balsiger, J.-J. Berthelier, A. Bieler, C. Briois, U. Calmonte, M. R. Combi, J. De Keyser, F. Dhooghe, B. Fiethe, S. A. Fuselier, S. Gasc, T. I. Gombosi, M. Hässig, A. Jäckel, M. Rubin, and C.-Y. Tzou. *Astronomy and Astrophysics*, 583:A1, 2015. doi: 10.1051/0004-6361/201526450.

Composition-dependent outgassing of comet 67P/Churyumov-Gerasimenko from ROSINA/DFMS. A. Luspay-Kuti, M. Hässig, S. A. Fuselier, K. E. Mandt, K. Altwegg, H. Balsiger, S. Gasc, A. Jäckel, L. Le Roy, M. Rubin, C.-Y. Tzou, P. Wurz, O. Mousis, F. Dhooghe, J. J. Berthelier, B. Fiethe, T. I. Gombosi, and U. Mall. *Astronomy and Astrophysics*, 583:A4, 2015. doi: 10.1051/0004-6361/201526205.

Solar wind sputtering of dust on the surface of 67P/Churyumov-Gerasimenko. P. Wurz, M. Rubin, K. Altwegg, H. Balsiger, J.-J. Berthelier, A. Bieler, U. Calmonte, J. De Keyser, B. Fiethe, S. A. Fuselier, A. Galli, S. Gasc, T. I. Gombosi, A. Jäckel, L. Le Roy, U. A. Mall, H. Rème, V. Tennishev, and C.-Y. Tzou. *Astronomy and Astrophysics*, 583:A22, 2015. doi: 10.1051/0004-6361/201525980.

Abundant molecular oxygen in the coma of comet 67P/Churyumov-Gerasimenko. A. Bieler, K. Altwegg, H. Balsiger, A. Bar-Nun, J.-J. Berthelier, P. Bochsler, C. Briois, U. Calmonte, M. Combi, J. De Keyser, E. F. van Dishoeck, B. Fiethe, S. A. A. Fuselier, S. Gasc, T. Gombosi, K. C. Hansen, M. Hässig, A. Jäckel, E. Kopp, A. Korth, L. Le Roy, U. Mall, R. Maggiolo, B. Marty, O. Mousis, T. Owen, H. Rème, M. Rubin, T. Sémon, C.-Y. Tzou, J. H. Waite, C. Walsh, and P. Wurz. *Nature*, 526:678-681, October 2015. doi: 10.1038/nature15707.

Detection of argon in the coma of comet 67P/Churyumov-Gerasimenko. H. Balsiger, K. Altwegg, A. Bar-Nun, J.-J. Berthelier, A. Bieler, P. Bochslers, C. Briois, U. Calmonte, M. Combi, J. De Keyser, P. Eberhardt, B. Fiethe, S. A. Fuselier, **S. Gasc**, T. I. Gombosi, K. C. Hansen, M. Hässig, A. Jäckel, E. Kopp, A. Korth, L. Le Roy, U. Mall, B. Marty, O. Mousis, T. Owen, H. Rème, M. Rubin, T. Sémon, C.-Y. Tzou, J. H. Waite, and P. Wurz. *Science Advances*, 1(8), 2015. doi: 10.1126/sciadv.1500377.

Spatial distribution of low-energy plasma around comet 67P/CG from Rosetta measurements. N. J. T. Edberg, A. I. Eriksson, E. Odelstad, P. Henri, J.-P. Lebreton, **S. Gasc**, M. Rubin, M. André, R. Gill, E. P. G. Johansson, F. Johansson, E. Vigren, J. E. Wahlund, C. M. Carr, E. Cupido, K.-H. Glassmeier, R. Goldstein, C. Koenders, K. Mandt, Z. Nemeth, H. Nilsson, I. Richter, G. S. Wieser, K. Szego, and M. Volwerk. *Geophys. Res. Lett.*, 42, 4263–4269, 2015. doi: 10.1002/2015GL064233.

Molecular nitrogen in comet 67P/Churyumov-Gerasimenko indicates a low formation temperature. M. Rubin, K. Altwegg, H. Balsiger, A. Bar-Nun, J.-J. Berthelier, A. Bieler, P. Bochslers, C. Briois, U. Calmonte, M. Combi, J. De Keyser, F. Dhooghe, P. Eberhardt, B. Fiethe, S. A. Fuselier, **S. Gasc**, T. I. Gombosi, K. C. Hansen, M. Hässig, A. Jäckel, E. Kopp, A. Korth, L. Le Roy, U. Mall, B. Marty, O. Mousis, T. Owen, H. Rème, T. Sémon, C.-Y. Tzou, J. H. Waite, and P. Wurz. *Science*, 348: 232-235, April 2015. doi: 10.1126/science.aaa6100.

Time variability and heterogeneity in the coma of 67P/Churyumov-Gerasimenko. M. Hässig, K. Altwegg, H. Balsiger, A. Bar-Nun, J. J. Berthelier, A. Bieler, P. Bochslers, C. Briois, U. Calmonte, M. Combi, J. De Keyser, P. Eberhardt, B. Fiethe, S. A. Fuselier, M. Galand, **S. Gasc**, T. I. Gombosi, K. C. Hansen, A. Jäckel, H. U. Keller, E. Kopp, A. Korth, E. Kührt, L. Le Roy, U. Mall, B. Marty, O. Mousis, E. Neefs, T. Owen, H. Rème, M. Rubin, T. Sémon, C. Tornow, C.-Y. Tzou, J. H. Waite, and P. Wurz. *Science*, 347(1):aaa0276, January 2015. doi: 10.1126/science.aaa0276.

2014

67P/Churyumov-Gerasimenko, a Jupiter family comet with a high D/H ratio. K. Altwegg, H. Balsiger, A. Bar-Nun, J. J. Berthelier, A. Bieler, P. Bochslers, C. Briois, U. Calmonte, M. Combi, J. De Keyser, P. Eberhardt, B. Fiethe, S. Fuselier, **S. Gasc**, T. I. Gombosi, K. C. Hansen, M. Hässig, A. Jäckel, E. Kopp, A. Korth, L. Le Roy, U. Mall, B. Marty, O. Mousis, E. Neefs, T. Owen, H. Rème, M. Rubin, T. Sémon, C.-Y. Tzou, H. Waite, and P. Wurz. *Science*, 347(27):1261952, January 2015. doi: 10.1126/science.1261952.